

INFORMATION TO USERS

This manuscript has been reproduced from the microfilm master. UMI films the text directly from the original or copy submitted. Thus, some thesis and dissertation copies are in typewriter face, while others may be from any type of computer printer.

The quality of this reproduction is dependent upon the quality of the copy submitted. Broken or indistinct print, colored or poor quality illustrations and photographs, print bleedthrough, substandard margins, and improper alignment can adversely affect reproduction.

In the unlikely event that the author did not send UMI a complete manuscript and there are missing pages, these will be noted. Also, if unauthorized copyright material had to be removed, a note will indicate the deletion.

Oversize materials (e.g., maps, drawings, charts) are reproduced by sectioning the original, beginning at the upper left-hand corner and continuing from left to right in equal sections with small overlaps.

Photographs included in the original manuscript have been reproduced xerographically in this copy. Higher quality 6" x 9" black and white photographic prints are available for any photographs or illustrations appearing in this copy for an additional charge. Contact UMI directly to order.

ProQuest Information and Learning
300 North Zeeb Road, Ann Arbor, MI 48106-1346 USA
800-521-0600

UMI[®]

University of Alberta

**A Multi-Wavelength Study of an HII Region/Supernova
Remnant Pair in a Rich Galactic Environment**

by

Tyler J. Foster ©

A thesis submitted to the Faculty of Graduate Studies and Research in partial
fulfillment of the requirements for the degree of Master of Science

Department of Physics

Edmonton, Alberta

Fall 2000



National Library
of Canada

Acquisitions and
Bibliographic Services

395 Wellington Street
Ottawa ON K1A 0N4
Canada

Bibliothèque nationale
du Canada

Acquisitions et
services bibliographiques

395, rue Wellington
Ottawa ON K1A 0N4
Canada

Your file Votre référence

Our file Notre référence

The author has granted a non-exclusive licence allowing the National Library of Canada to reproduce, loan, distribute or sell copies of this thesis in microform, paper or electronic formats.

The author retains ownership of the copyright in this thesis. Neither the thesis nor substantial extracts from it may be printed or otherwise reproduced without the author's permission.

L'auteur a accordé une licence non exclusive permettant à la Bibliothèque nationale du Canada de reproduire, prêter, distribuer ou vendre des copies de cette thèse sous la forme de microfiche/film, de reproduction sur papier ou sur format électronique.

L'auteur conserve la propriété du droit d'auteur qui protège cette thèse. Ni la thèse ni des extraits substantiels de celle-ci ne doivent être imprimés ou autrement reproduits sans son autorisation.

0-612-59804-7

Canada

University of Alberta

Library Release Form

NAME OF AUTHOR: Tyler J. Foster


TITLE OF THESIS: A Multi-Wavelength Study of an HII
Region/Supernova Remnant Pair in
a Rich Galactic Environment

DEGREE: Master of Science

YEAR THIS DEGREE GRANTED: 2000

Permission is hereby granted to the University of Alberta Library to reproduce single copies of this thesis and to lend or sell such copies for private, scholarly or scientific research purposes only.

The author reserves all other publication and other rights in association with the copyright in the thesis and, except as hereinbefore provided, neither the thesis nor any substantial portion thereof may be printed or otherwise reproduced in any material form whatever without the author's prior written permission.



Tyler J. Foster
Apt. 4,
14224 McQueen Road
Edmonton Alberta T5N 3L7
CANADA

August 10, 2000

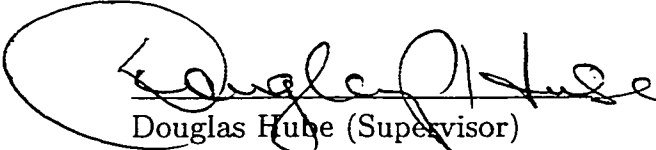
Abstract

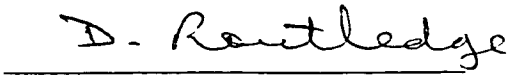
This work presents original results from an astrophysical study involving observations at many astronomical wavelengths. Presented first are hardware and software developed for a unique CCD camera system at the Devon Astronomical Observatory. Results from performance measurements are given, and proper observing and processing techniques for achieving high photometric precision are outlined with examples. A scientific grade software package (DevonCB) is developed for CCD data acquisition, calibration and photometric analysis at the DevonAO. New radio, optical, and infrared observations of Galactic objects NRAO 655 and 3C434.1, near $l = 94^\circ$, are presented. The first ever detections of these objects are achieved in optical emission lines at the DevonAO, and in radio recombination lines at Dominion Radio Astrophysical Observatory. These data, along with radio continuum and line observations are used to derive new physical properties of NRAO 655 and 3C434.1, contributing to the astrophysical knowledge of the objects and interstellar medium in the Galactic plane towards Cygnus.


University of Alberta

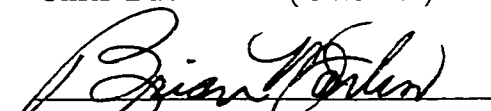
Faculty of Graduate Studies and Research

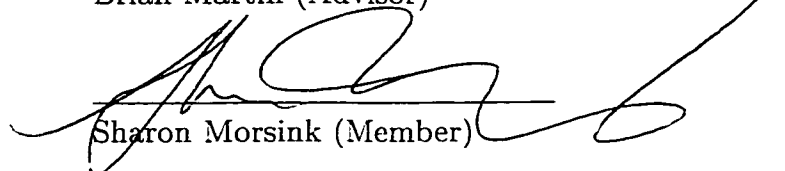
The undersigned certify that they have read, and recommend to the Faculty of Graduate Studies and Research for acceptance, a thesis entitled **A Multi-Wavelength Study of an HII Region/Supernova Remnant Pair in a Rich Galactic Environment** submitted by **Tyler J. Foster** in partial fulfillment of the requirements for the degree of Master of Science.


Douglas Hube (Supervisor)


David Routledge (Supervisor)


Chris Backhouse (External)


Brian Martin (Advisor)


Sharon Morsink (Member)

DATE: August 4, 2000.

Acknowledgements

This work is a testimony to the company and counsel of many people I am fortunate to be involved with. Dr. Douglas Hube and Dr. David Routledge were always supportive: from finance for travel opportunities, to allowing my independence in experiment and approach, to offering their patience, friendship and understanding. Dr. Brian Martin's years of encouragement, sound advice and friendship have positively influenced me personally and professionally. Albert VanSteenbergen's talented contributions to the software and hardware development are substantial, and his friendship is important to me. The technical expertise and good nature of Roy Schmaus and Barry Arnold made this project successful and fun. Dr. Fred Vaneldik's financial contributions are the backbone of the DevonAO project, and his friendly presence as a member of the Astrophysics Group will always be appreciated. Tom Landecker, John Galt, Ken Tapping and the staff at DRAO were always gracious and helpful. My father's support is most important to me. Finally, Marie's love is inspiring of confidence and success.

These many people are owed much more than this section can disclose.

Contents

1	INTRODUCTION	1
1.1	THE MULTI-WAVELENGTH APPROACH TO ASTRONOMY	1
1.2	CHAPTER DESCRIPTIONS	3
1.3	REFERENCES	4
2	DEVELOPMENT AND OPERATION OF THE DEVON ASTRONOMICAL OBSERVATORY	6
2.1	SUMMARY	6
2.2	HISTORY AND RATIONALE	6
2.3	CHOICE OF CCD AND DISCUSSION OF SIGNAL CONCERNS	7
2.4	DISCUSSION OF CCD NOISE CONCERNS	8
2.5	ACHIEVING OPTIMAL SIGNAL TO NOISE	12
2.6	THE ROLE OF THE DEVON TELESCOPE DESIGN IN S/N AND PRECISION PHOTOMETRY	14
2.7	DATA REDUCTION OF DEVON AO IMAGES	17
2.8	PHOTOMETRIC PERFORMANCE OF THE DEVON SYSTEM	19
2.9	REFERENCES	22
3	DEVONCB SOFTWARE	23
3.1	SUMMARY	23
3.2	INTRODUCTION TO DEVONCB	23
3.3	AN OVERVIEW OF THE INTERFACE	24
3.4	DESCRIPTIONS OF PRIMARY FUNCTIONS	28
3.5	DESCRIPTION OF MEASUREMENT AND VISUALIZATION FUNC- TIONS	33
3.6	DESCRIPTION OF CUSTOMIZABLE FEATURES	41
3.7	THE FUTURE OF DEVONCB	43
3.8	REFERENCES	44

4	RADIO AND OPTICAL OBSERVATIONS OF OBJECTS IN THE CGPS FIELD J8	46
4.1	SUMMARY	46
4.2	THE DRAO SYNTHESIS TELESCOPE (DRAO ST)	46
4.3	THE DRAO 26M TELESCOPE	52
4.4	THE DEVON 0.5M OPTICAL TELESCOPE	53
4.5	REFERENCES	64
5	HII REGION NRAO 655 AND THE GALACTIC ENVIRONMENT NEAR $l = 94^\circ$	65
5.1	SUMMARY	65
5.2	INTRODUCTION TO OBJECTS NEAR $l=94^\circ$	66
5.3	STRUCTURE AND APPEARANCE OF OBJECTS NEAR $l=94^\circ$	69
5.4	INTEGRATED FLUXES AND RADIO SPECTRA OF OBJECTS NEAR $l=94^\circ$	79
5.5	LINE EMISSION FROM HII, HI AND H ₂ SURROUNDING NRAO 655 AND 3C434.1	83
5.6	A MODEL FOR NRAO 655	89
5.7	EVIDENCE OF INTERACTION AND A COMMON ISM FOR OB- JECTS NEAR $l=94^\circ$	91
5.8	REFERENCES	93
6	THE FUTURE FOR THE DEVON ASTRO- NOMICAL OBSERVATORY	97
6.1	THE POSSIBILITIES	97
6.2	PROJECT SUMMARY STATEMENT	99
6.3	REFERENCES	99
A	PROCESSING OF 21CM AND 74 CM DRAO ST CONTINUUM IMAGES	100

List of Figures

2.1	The reflectivity profile of the Devon TK512 CCD sensor and optical window, across the spectral range of 350nm-800nm.	9
2.2	Histograms of zero frames obtained in different modes/environments.	10
2.3	Temperature dependence of non-MPP mode thermal generation rate for the Devon TK512 CCD sensor.	12
2.4	Log-log plot of the integration time dependence of thermally generated signal, during MPP and Non-MPP operation. The slope of each line is the thermal generation rate ($ADU \text{ pixel}^{-1} s^{-1}$) for each mode, values for which are beneath the chart's title. Standard deviation (σ_{rms}) from linearity (solid lines, least squares fit) is labelled for each mode.	13
2.5	The linearity breakdown of the Devon TK512 sensor, measured approaching the effective full well of 300000 electrons.	15
2.6	Results of aperture photometry performed on the SX Phe. variable star BL Cam.	21
3.1	The window interface of DevonCB. Note the field of the Devon CCD covers most of the Moon ($\sim \frac{1}{2}^{\circ} \times \frac{1}{2}^{\circ}$).	26
3.2	The image processing control window of DevonCB.	34
3.3	On the left, the original image of M51 obtained through the sky glow of Edmonton, Alberta. Histogram stretching (middle image) enhances the contrast of M51, while histogram equalization (right) strongly emphasizes the galaxy.	35
3.4	The raw image (left) is first processed with a strong high pass filter to accentuate detail in the spiral arms. The image was then weakly low pass filtered to remove noise. Finally, the image histogram was stretched to produce the fine detailed view of M51 (right).	36
3.5	An image of the Crab nebula (at left) is enhanced by the series of an erosion, high pass, and two weak low pass filters, along with a contrast boost from histogram stretching. Note the prominence of the filaments in the filtered image.	37
3.6	A portion of a DevonAO image in original form (left), masked (middle) and the result of subtracting this from the original (right). Details in the lunar highlands become apparent.	37

3.7	The Quick Photometry Window of DevonCB, performing aperture measurements on stars in a field near NRAO 655.	38
3.8	The FITS header editor window, changing the INSTRUME keyword in an image of supernova remnant 3C434.1.	42
3.9	The Observatory Setup window.	43
3.10	The COMM Settings window configured to use COM1.	43
4.1	Central $2.5^\circ \times 2.5^\circ$ of the 21cm DRAO ST map in CGPS J8 field.	50
4.2	Central $2.5^\circ \times 2.5^\circ$ of the 74cm DRAO ST map in CGPS J8 field.	51
4.3	Frequency-switched observations of radio spectral lines with the DRAO 26m telescope.	54
4.4	Radio recombination spectrum of NRAO 655, observed by the author with the DRAO 26m telescope. A 3rd-order polynomial baseline was fit to the filter band shape and subtracted to produce the curve shown. A Gaussian fit is overlaid on the broad $H158\alpha$ signal, and residuals plotted below. The $FWHM = 41\text{km.s}^{-1}$ line is centered on -71.8km.s^{-1}	55
4.5	$H\alpha + [NII]$ ($\lambda_{centre} = 656.3$ nm, $FWHM=7.5$ nm) emission composite image of NRAO 655 obtained at the Devon AO with a cumulative integration time of 13200 seconds. North is toward the lower-left corner of the frame, and east is to the lower right. Greyscale runs linearly from 300 ADU (dark) to 700 ADU (light).	59
4.6	21cm DRAO ST image of NRAO 655 scaled and rotated to match the DevonAO field size and orientation. Contours are from 21cm brightness temperatures (1.65K, 2.7K, 3.7K, 4.8K, 5.9K, 6.9K).	60
4.7	$H\alpha$ composite frame (same orientation as Figure 4.5) with stars removed and displayed with an inverted greyscale to highlight emission features. Greyscale is from 600 ADU (dark) to 400 ADU (light).	61
4.8	Planetary nebulae observations for calibrating $H\alpha$ emission line intensity of NRAO 655. Extra-atmospheric instrumental magnitudes (m_{inst}) are intercepts at $airmass = 0$, and extinction line slopes denote the $H\alpha$ extinction coefficient $k'_{H\alpha}$	63
5.1	A DRAO 74cm map of the galactic region near $l=94^\circ$, showing the location of objects listed in Table 5.1. Note the two supernova remnants 3C434.1 and CTB 104A among the number of HII regions in the field.	67
5.2	DRAO ST continuum image of SNR 3C434.1 at $\lambda = 21\text{cm}$ with galactic coordinates displayed. North is towards the upper-left corner, and east the lower-left.	70
5.3	DevonAO $H\alpha + [NII]$ image of 3C434.1 with $\lambda = 21\text{cm}$ brightness temperature contours ($2.0K$, $4.85K$) displayed. North is up. Optical image (stars removed) has been inverted to highlight nebulosity (emission is dark).	71

5.4	DRAO ST continuum image of NRAO 655 at $\lambda = 21\text{cm}$ with galactic coordinates displayed. The SNR 3C434.1 is immediately east of this emission, at $l = 94.0^\circ, b = 1.0^\circ$. NRAO 652 is visible at $l = 93.0^\circ, b = 2.0^\circ$. Contours are brightness temperatures at 1.6, 2.6, 3.3, 4.2 and 5.0 K.	72
5.5	Radial brightness temperature (T_b) and electron density (n_e) profiles through the tail of NRAO 655. T_b values are from the 21 cm DRAO ST image. Solid line is a least squares power law fit to density profile (eq. 5.2). Radius is measured eastward from the centre of the semi-circular kernel.	73
5.6	60 μm IRAS image of NRAO 655, iterated 20 times in a deconvolution technique (Maximum Correlation Method). Artifacts (“ringing”) around point sources are produced by MCM. Contours are brightness temperatures (1.6K, 3K, 5K) from a 21cm DRAO ST image of NRAO 655. North is up. The 7' finger runs ESE from $l = 93.3^\circ, b = 1.65^\circ$ to $l = 93.4^\circ, b = 1.55^\circ$	75
5.7	Sigma stepped contours ($4\sigma, 5\sigma, 6\sigma$ above the background), overlaid on the original composite $H\alpha + [NII]$ line image. Contours around edge and halo artifacts have been removed. The shape of NRAO 655 is very apparent. North is up, east is left, and the field is $24' \times 24'$	76
5.8	Devon AO $H\alpha + [NII]$ image (656.3nm) on a $53' \times 53'$ DRAO 21cm image of NRAO 655. Dramatically similar morphology in the radio and optical regimes is evident, as both wavelengths show a semi-circular, regular shell of emission. North is up. . . .	77
5.9	NRAO 655 at optical and IR wavelengths. The semi-circular shell is again evident in both images, but bright areas of $H\alpha + [NII]$ optical emission correspond to dim areas of dust emission. . . .	78
5.10	Radio spectra of 3C434.1 and NRAO 655.	81
5.11	Spectral index map of 3C434.1 and NRAO 655, calculated with radio continuum 11cm and 74 cm maps. The 21cm continuum contours are overlaid. Note the distinctly lower average index of NRAO 655, indicative of thermal emission. The westerly extension from 3C434.1 appears to have a high index, similar to the shell itself. The greyscale runs from index $\alpha = 0.7$ (dark) to $\alpha = -1.1$ (light).	82

5.12	Atomic and molecular hydrogen shells surrounding the kernel of NRAO 655. Both the HI emission (grayscale map) and the CO emission (dotted contour lines) have been integrated over a 13 km s^{-1} velocity interval centred on -71.5 km s^{-1} . White lines are 1.4 GHz continuum emission contours (1.5K, 3K and 5K of brightness temperature) from NRAO 655. The velocity-integrated CO contours (13, 26, and 39 K km s^{-1} of $\int T_b dv$) appear to wrap around the head of NRAO 655 in the form of a crescent, and the cavity in the velocity-integrated HI emission coincides well in position and shape with the kernel of NRAO 655. The mean has been subtracted from this image, and the greyscale runs linearly from $T_b = -130 \text{ K km s}^{-1}$ (dark) to $T_b = +195 \text{ K km s}^{-1}$ (light).	85
5.13	Radial profiles from NRAO 655's centre towards the western rim, showing the layered appearance of hydrogen.	86
5.14	The average HI T_b spectrum for $l = 94^\circ$ over a region of diameter $40'$. The vertical line at -72 km s^{-1} shows the central velocity of HI and CO emission associated with NRAO 655. Visible nearby gas in the local spiral arm, which peaks near 2 km s^{-1} . The Perseus spiral arm is visible at -68 km s^{-1} (8.3 kpc), and the outer spiral arm near -100 km s^{-1} (12.6 kpc).	87
5.15	A scenario similar to the observed structure of NRAO 655 today. An O-star forms inside a molecular cloud, and erodes and ionizes a cavity near the edge. Ionized gas breaks out of the side into the less dense surroundings, while the ionization front (IF) inside advances towards the center of the cloud. R is defined as the radius of curvature for the IF with respect to the ionized gas, and three configurations ($R^{-1} > 0$, $R^{-1} \sim 0$, and $R^{-1} < 0$) are defined by Whitworth, 1979.	90
5.16	Evolution of a dense HII region as it breaks through the edge of its parent cloud, and "champagne flows" into the surrounding ICM. From Tenorio-Tagle, 1979.	92
5.17	The galactic environment from $l = 88^\circ, b = -3.5^\circ$ (lower right) to $l = 98^\circ, b = +5.5^\circ$ (upper left), centred on $l = 93.12^\circ, b = 1.005^\circ$ (near NRAO 655). Many more objects are visible than are listed in Table 5.1. The large region surrounding 3C434.1 and NRAO 655 is enveloped in a halo of weak continuum emission, suggestive of an interstellar medium shared by these objects. Map derived from a CGPS continuum super-mosaic at $\lambda = 21 \text{ cm}$.	94

List of Tables

1.1	The various wavelengths of astronomical data obtained for this thesis. The observing bands for each data set are listed, as is the interstellar medium component that a particular band is intended to study. Data sources listed are (1) Mullard Radio Astronomy Observatory (Vessey et al., 1998), (2) Dominion Radio Astrophysical Observatory (Dougherty et al., 1996), (3) 100m Effelsberg telescope 2695 MHz Survey (Reich et al., 1984) (4) Harvard Smithsonian Center for Astrophysics (Dame et al., 1987), (5) California Institute of Technology (www.ipac.caltech.edu/ipac/IGA), (6) Canadian Institute for Theoretical Astrophysics (Kerton et al., 2000), and (7) University of Alberta, Devon Astronomical Observatory (Foster et al., 1999).	2
2.1	CCD Device Screening data (provided by Tektronix) of the University of Alberta's TK512 sensor. All measurements were performed at -90°C unless stated otherwise.	8
2.2	Broadband and Line Filter Characteristics for the Devon Telescope System. Each filter is 50.8 mm in diameter.	17
2.3	Devon Telescope/CCD Camera System performance specifications.	18
2.4	Details of Devon AO test observations of BL Cam, a SX Phe. type variable star.	20
3.1	Minimum recommended system requirements for DevonCB Software.	24
3.2	Description of primary function areas of the DevonCB interface.	25
3.3	Menu Items from the main DevonCB form and their nested functions.	27
4.1	Details of astronomical data observed and processed by the author.	47
4.2	Details of the DRAO Synthesis Telescope	47
4.3	CGPS J8 Field Observational Parameters.	48
4.4	Summary of Observations of CGPS J8 Field Objects, carried out at the Devon AO. Note: G93.6+1.3 was observed during bright sky conditions (full moon).	57

5.1	A list of HII regions and supernova remnants present in the rich galactic region near $l=94^\circ$ seen in Figure 5.1. Kinematic distances are published for only two of the objects: CO and NH ₃ velocities were found for WB43 by Wouterloot (et al.) and Molinari (et al.) respectively, while H112 α recombination line observations of BG2107+49 by Higgs et al. placed this object at $v=-80 \text{ kms}^{-1}$. An unpublished velocity ($v=-58 \text{ kms}^{-1}$) for CTB 102 was obtained by Fich, 1983 observing H109 α recombination line (5 GHz). References: (1) Pauliny-Toth et al. 1966; (2) Mantovani et al. 1982; (3) Molinari et al. 1996; (4) Miralles et al. 1994; (5) Wouterloot and Brand 1989; (6) Fich 1986; (7) Kallas and Reich 1980; (8) Reich et al. 1990; (9) Galt and Kennedy 1968; (10) van der Werf and Higgs 1990; (11) Landecker et al. 1985; (12) van der Werf and Higgs 1991.	66
5.2	Radio data used for spectral index study of J8 field objects 3C434.1 and NRAO 655. References: (1) Kassim, 1988, (2) Vessey et al., 1998, (3) Rengelink et al., 1996, (4) 1990, Reich et al. and (5) 1984, Reich et al.	80
5.3	Infrared and optical flux densities and fluxes for NRAO 655, as derived from IRAS (www.ipac.caltech.edu/ipac/iras/iras.html) and Devon AO observations. A strong IR point source at ($l=93.37$, $b=1.82$) is visible at 12 and 25 microns within the "head" of NRAO 655. This was individually measured and its flux density removed.	83
5.4	The four-component model of NRAO 655.	89
6.1	Previous optical identifications of sources surrounding $l = 94^\circ$, and the appearance of emission and absorption features near them. Only BG2107+49 has been optically identified in a 1983 red (700nm) CCD image from an extended study by Higgs et al., 1987. Faint optical emission features are seen near CTB 102 in the Digitized Sky Survey POSS plate scans, but studies of these have not been published by any author. Coordinates given are J2000.	98

Chapter 1

INTRODUCTION

1.1 THE MULTI-WAVELENGTH APPROACH TO ASTRONOMY

This work presents the design and operation of a unique astronomical telescope, achievements in software development, breadth and innovation in astronomical observing and data processing, and discovery in a rich region in the Milky Way Galaxy. Ultimately, through this thesis the author hopes to demonstrate the usefulness of a multi-wavelength approach to astronomical study, particularly in combining optical and radio observations of an unstudied object. This multi-wavelength approach is not new, and is becoming more common as the astronomical world embraces the diversified astronomer. However, publications of research on radio objects seldom include an optical component, or even attempts at optical observations. The success of this study shows that this broad approach should be taken more often, and that an individual astronomer need not specialize in a single window of the wide electromagnetic spectrum showering our planet.

A perfect example of cooperative multi-wavelength astronomy is the Canadian Galactic Plane Survey (CGPS). This is an international collaboration to map all of the major interstellar components of the Milky Way at a common resolution: neutral atomic gas, molecular gas, ionized gas, dust grains, and relativistic plasma. For many of these constituents, angular resolution is improved over previous studies by more than a factor of 10. The principal goal of the project is astrophysical research into all the major ISM components that make up our Galaxy, made possible by the creation of a database of panoramic, high resolution images. The cornerstone of this survey is the 1' angular resolution mosaics of radio continuum and line data produced at the Dominion Radio Astrophysical Observatory (DRAO). Astronomers at DRAO, and a consortium of astronomers from universities across Canada have completed observing for Phase I of the CGPS, with Phase II observations already under way. The CGPS consortium meets annually, and research papers presenting multi-wavelength looks at galactic objects and regions are given, attesting to the depth of astron-

λ	Observing Band	ISM Component	Data Source
190cm	Radio	Ionized	1
74cm	Continuum	Gas and	2
21cm		Relativistic	2
11cm		Plasma	3
21.1cm	HI Spectral Line	Atomic HI	2
21.042	HII Spectral Line	Ionized HII	2
18.153 cm	HII Spectral Line	Ionized HII	2
2.6mm	CO Spectral Line	Molecular H_2	4
100 μm	Infrared	Dust	5
60 μm	Continuum	Grains	5
25 μm			6
12 μm			6
672nm			Optical
656nm	Emission Lines	H α	7
502nm		and OIII	7

Table 1.1: The various wavelengths of astronomical data obtained for this thesis. The observing bands for each data set are listed, as is the interstellar medium component that a particular band is intended to study. Data sources listed are (1) Mullard Radio Astronomy Observatory (Vessey et al., 1998), (2) Dominion Radio Astrophysical Observatory (Dougherty et al., 1996), (3) 100m Effelsberg telescope 2695 MHz Survey (Reich et al., 1984) (4) Harvard Smithsonian Center for Astrophysics (Dame et al., 1987), (5) California Institute of Technology (www.ipac.caltech.edu/ipac/IGA), (6) Canadian Institute for Theoretical Astrophysics (Kerton et al., 2000), and (7) University of Alberta, Devon Astronomical Observatory (Foster et al., 1999).

omy that is accomplished. For more details, the reader is referred to the public information web site of the CGPS (www.ras.ucalgary.ca/CGPS), and English et al., 1998.

This thesis will concentrate on the relatively unstudied supernova remnant 3C434.1 and the nearby object NRAO 655, previously classed as a supernova remnant as well. The field with CGPS survey code J8 was centred near these objects (galactic coordinates $l = 93.74^\circ$, $b = 1.00^\circ$). To effectively contribute to the knowledge of 3C434.1, NRAO 655 and the surrounding ISM, the author gathered astronomical data at various wavelengths (listed in Table 1.1), which were used in the following astrophysical study. Some of the data were kindly made available only in a pre-release form.

1.2 CHAPTER DESCRIPTIONS

Each chapter in this paper-format thesis contains a summary of its own; hence the short length of this introductory chapter. However, for reference a brief description of each is included here. The order of these chapters has been chosen to give the reader appreciation of the complexities involved in astronomical instrument and software design, and of the true art involved in astronomical observing and processing. The thesis concludes with a presentation of original results in the most complete astrophysical study undertaken of 3C434.1 and NRAO 655, a supernova remnant (SNR)/HII region pair in the constellation of Cygnus.

Chapter 2 is purposefully written to be useful to any amateur or professional astronomer working with a CCD system with goals of precision photometry and faint object detection. Theoretical and practical aspects of the CCD system at the Devon Astronomical Observatory (Devon AO), and the many aspects of astronomical CCD observations are presented. The goal is to help Devon astronomers and others collect high quality CCD data which achieve an optimal signal-to-noise ratio for the objects studied. Photometric results, with the precision originally envisioned by the astrophysics group at the University of Alberta, are presented along with a detailed breakdown of the observing and reduction techniques used to achieve these results.

The success of the system at the Devon AO is due in part to positive changes in observing habits allowed by the control package, *DevonCB software*. Chapter 3 is essentially the user's guide to this software, presenting its operation in fine detail, and looking at the underlying theory used in the image processing and aperture photometry tasks. The automation of routine observing provided by the package is intended to allow an observer to focus his or her attention on the quality of the data as they are collected.

Chapter 4 presents details of the Dominion Radio Astrophysical Observatory synthesis telescope (DRAO ST) and observations, and the complex processing steps necessary to apply to raw aperture synthesis data (the actual steps of which are presented in Appendix A). Furthermore, this chapter discusses frequency-switched spectral line observations with the single dish 26m radio telescope at DRAO. This fourth chapter also brings chapters 2 and 3 together, demonstrating the capability of the Devon AO 0.5m telescope for faint-object emission line observations. The careful reduction and calibration of these optical data are discussed. The resulting calibrated images and spectra from the three telescopes are presented. Data from each telescope represent achievements of their own. DRAO ST data are the highest resolution (1') radio observations ever obtained of the objects in the $l = 94^\circ$ region. The DRAO 26m spectrum of the H158 α line from NRAO 655 represents the first detection of this object in recombination line emission. Finally, the discovery of NRAO 655 in H α optical emission line is presented in an image from the Devon AO system.

Chapter 5 compiles the results of an original astrophysical study on the SNR/HII region pair 3C434.1/NRAO 655 in the CGPS J8 observing field. Astrophysical properties of 3C434.1 and NRAO 655 are derived using the multi-

wavelength data presented in Table 1.1. A possible relationship between these objects is discussed. This chapter's original content is intended to contribute significantly to the knowledge of objects in the area near galactic longitude $l = 94^\circ$, a rich region of the Milky Way Galaxy.

Chapter 6 concludes this work, with a statement on the scope of the potential science waiting to be done with the Devon AO system in conjunction with the Canadian Galactic Plane Survey. A significant contribution to the astrophysical knowledge of our Galaxy awaits.

Appendix A is meant to serve as a recipe for DRAO ST data processing, and as a reference for future students of this field. Calculations of parameters and inputs are specific to the author's data, but the methods are applicable to any DRAO ST observations.

It is the sincerest hope that this work will serve the reader in his/her pursuits of astronomical science, whether in optical or radio wavelengths, perhaps in both.

1.3 REFERENCES

Dame T. M., Ungerechts H., Cohen R. S., de Geus E. J., Grenier I. A., May J., Murphy D. C., Nyman L., and Thaddeus P., 1987, *ApJ* 322, 706.

Dougherty S. M., Dewdney P., Galt J., Gray A., Higgs L., Landecker T., Purton C., Roger R., Tapping K., Willis T., Taylor A. R., Leahy D., Carignan C., St-Louis N., Fich M., Ghazzali N., Irwin J., Joncas G., Pineault S., Martin P., McCutcheon W., Routledge D., Vaneldik F., Matthews H., Moriarity-Scheiven G., Beichman C., Terebey S., Duric N., Green D., Heiles C., Heyer M., Langer W., Watson D., Wendker H., Zhang X., 1996, *AAS Meeting* 189, #17.04.

English J., Taylor A. R., Irwin J. A., Dougherty S. M., Basu S., Beichman C., Brown J., Cao Y., Carignan C., Crabtree D., Dewdney P., Duric N., Fich M., Gagnon E., Galt J., Germain S., Ghazzali N., Gibson S. J., Godbout S., Gray A., Green D. A., Heiles C., Heyer M., Higgs L., Jean S., Johnstone D., Joncas G., Landecker T., Langer W., Leahy D., Martin P., Matthews H., McCutcheon W., Moriarity-Scheiven G., Pineault S., Purton, C., Roger R., Routledge D., St-Louis N., Tapping K., Terebey S., Vaneldik F., Watson D., Willis T., Wendker H., Zhang X., 1998, *PASA* 15, 56.

Foster T., Hube D., Couch J., Martin B., Routledge D., and Vaneldik F., 1999, *ASP Conference Series* (E. Craine, R. Tucker and J. Barnes, editors) 189, 111.

Kerton C.R., and Martin P.G., 2000, *ApJS* 126, 85.

Reich W., Fūerst E., Haslam C. G. T., Steffen P., and Reif K., 1984, *A&AS* 58, 197.

Vessey S.J., and Green D.A., 1998, *MNRAS* 294, 607.

Chapter 2

DEVELOPMENT AND OPERATION OF THE DEVON ASTRONOMICAL OBSERVATORY

2.1 SUMMARY

To optically image faint, extended objects previously observed only at radio wavelengths requires a very sensitive imaging system. The Devon Astronomical Observatory (Devon AO) houses a system so designed. Coupled with optics capable of producing sharp stellar images over a wide field is a high sensitivity/low noise Charge-Coupled Device (CCD) held at the prime focus of the telescope. This design and construction is unique in Canada, and has now been proven to be effective, producing images of optically undiscovered HII regions and supernova remnants. This chapter discusses the history and current design of the telescope and camera. Efficiency and noise concerns of the Devon CCD system are discussed, and measurements and recommendations are presented towards understanding and obtaining an optimal S/N for various observing programs. Techniques of CCD data reduction are also discussed, and applied to test observations of a known variable star. The photometric results of these observations are presented, and a statement on the system's capability for precision photometry is made.

2.2 HISTORY AND RATIONALE

The DevonAO houses a 0.5m Cassegrain design telescope, and has been in operation with this instrument since 1979. Until the middle of the last decade, principal observing at the DevonAO was of variable stars of intrinsic types β Cephei and δ Scuti, as well as eclipsing and contact binary systems. Photometry was performed with a 2 star photometer at $f/8$ and $f/18$ focal ratios provided by interchangeable front-ends. A collaboration between optical and radio astronomy groups at the University of Alberta began in the early 1990's, to design and build a system for a medium format CCD camera.

The collaboration envisioned learning more about the interstellar medium

by combined optical and radio study of the objects within it. The types of objects proposed as targets were those observed at radio wavelengths by the radio astronomy group: primarily supernova remnants and HII regions. Normally, they would be observed as needed, using the DRAO synthesis telescope (see Chapter 4). However, as the Canadian Galactic Plane Survey (CGPS) came online in 1995, large high resolution radio mosaics of fields in the plane of the Milky Way Galaxy became available. The development of the Devon CCD system can thus serve a much broader community, by providing emission line images of radio objects to complement those from the CGPS. Optical and radio images of SNR's can collectively be studied for structural similarities (such as filamentary appearance), and independently to provide measures of gas density and temperature. Optical line observations can show the presence of shocked gas in SNR's, through line ratios of different elements. Optical detection and astrophysical analysis of these objects depends on a sensitive CCD sensor with low noise characteristics, a large chip and a fast telescope to image as wide a field as possible, and a good selection of emission line filters. The Devon system has been designed with all these characteristics, and is now delivering the first ever optical images of galactic objects previously detected at radio wavelengths only.

2.3 CHOICE OF CCD AND DISCUSSION OF SIGNAL CONCERNS

To maximize chances for detecting faint line emission from radio objects, the CCD chosen had to have two characteristics: 1) high efficiency over the broad spectrum range of optical emission lines (330nm - 1000nm), and 2) Low dark and read noise. These characteristics are fulfilled by the Tektronix TK512 CCD imager, a thinned, back illuminated optically flat sensor with Multi-Pinned Phase (MPP) operation. The chip is designed for low light level imaging from UV to near infrared (NIR), and has a very high dynamic range relative to readout noise. See Table 2.1 for our device specifications as provided by Tektronix on July 8, 1993.

Quantum efficiency essentially measures photon loss, and is the ratio of photoelectrons created to number of incident photons. The high quantum efficiency of the TK512 device is primarily due to the thinned, back illuminated design. Backside accumulation of photoelectrons overcomes the gate electrode absorption inherent in the less complex front illuminated designs. In front illuminated sensors, the gate electrodes (potential wells) for each pixel are located just under the front surface of the sensor. At $\lambda = 400nm$, the skin depth (where e^{-1} of the incident photons are absorbed) in silicon is only 200 nm, and most photons are absorbed by the gates themselves before creating an electron-hole (e^- -h) pair in the pixel. By thinning the silicon wafer, (typically from 300 μm to less than the skin depth of visible light in silicon, typically 8-10 μm), and subsequent placement of the gate electrodes on the back of the chip, efficiencies

Specification	Value (CCD Temp. = 183 K)
Dimensions	512×512 pixels (13.8mm×13.8mm)
Pixel Size	27μm×27μm
Readout Noise r_e	7.86 e^-rms
Full Well signal	3.56×10 ⁵ electrons
Dynamic range (relative to r_e)	48 dB
Quantum Efficiency→λ =400 nm	35%
λ = 550 nm (CCD Temp. = 263 K)	90%
λ = 700 nm	60%
Readout rate	50 000 pixels s^{-1}
Charge Transfer Efficiency (CTE)	0.999999

Table 2.1: CCD Device Screening data (provided by Tektronix) of the University of Alberta’s TK512 sensor. All measurements were performed at $-90^{\circ}C$ unless stated otherwise.

of $>70\%$ for $\lambda > 450nm$ are achieved. However, NIR photons ($\lambda > 1000nm$) penetrate several hundred microns, and the CCD appears essentially more and more transparent approaching these wavelengths (Janesick et al., 1992).

The presence of an anti-reflection coating on the SiO_2 surface also aids in faint object detection. An anti-reflection (AR) coating overcomes the loss of photons at the surface of the sensor due to reflection. With no coating, such losses peak as great as 70% in the UV ($\lambda = 250nm$) (Janesick et al., 1992). The reflectivity profile of the TK512 (Figure 2.1) shows reflection losses of only 25% for the Devon CCD chip, illustrating the beneficial effect of its UV enhanced AR coating. The reflectivity is surprisingly high across the visible spectrum (30-40%), and the problem is compounded by the optical window present, which itself reflects 25% of incoming light. Although the chip is not as efficient at visible wavelengths as we had envisioned, it performs very well at imaging faint objects, as shown in Chapter 4.

2.4 DISCUSSION OF CCD NOISE CONCERNS

In addition to recording as many photons as possible, a CCD for faint object imaging must maximize the dynamic range of the data by minimizing instrumental noise. CCD’s are subject to two dominant sources of intrinsic noise: readout noise and dark current. Both are discussed further in this section. Minimizing both of these by informed choice of one’s chip is the first step, but one should also monitor the camera’s noise characteristics continually, since, in the author’s experience, the values for read noise and dark current generation rate can vary.

The noise “floor” of a CCD chip is its readout noise (or readnoise) level. Readnoise is a general term that includes electron rms fluctuations from thermal generation during readout plus noise generated by the on-chip amplifier.

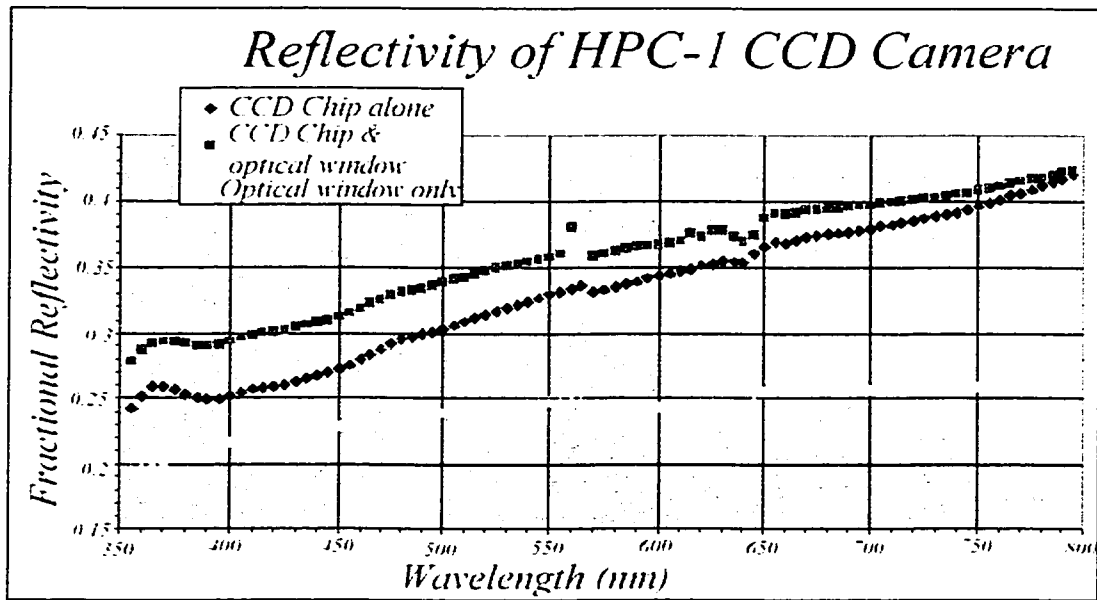


Figure 2.1: The reflectivity profile of the Devon TK512 CCD sensor and optical window, across the spectral range of 350nm-800nm.

Amplifier contribution to readnoise is a constant of the particular chip used, but the thermal component does depend on the dark current collected during the finite readout time, and thus on the operating temperature of the CCD. Readout noise can be measured by accumulating several readout images (or zero integrations) of the cooled CCD, and averaging. Provided no other noise sources (e.g. RFI contamination) are present, the distribution of pixels in this mean frame (after subtraction of pedestal, or overscan level) should be Gaussian about zero, with width σ defined by the readout noise (r_e) divided by the square root of the number n of coadded frames (Gilliland, 1992, and Massey et al, 1992). Measured in electrons (e^-), the readnoise is:

$$r_e = gain \times \sqrt{n} \times \sigma_{ADU} \tag{eq. 2.1}$$

where *gain* is defined as the number of electrons per single count, or analog-digital unit (ADU). The dependence of readnoise (measured for our TK512) on dark current is shown in Figure 2.2, histograms of several mean zero frames obtained in different conditions. This illustrates the contribution of dark current to the overall noise quality in an image. Large dark current skews the pixel distribution away from a mean of zero and spreads it out (implying increased readnoise). Figure 2.2 also graphically illustrates the importance of Multi-Pinned Phase (MPP, discussed below) in lowering the dark current, and hence the readout noise.

Tektronix quotes a level of $8 e^-$ rms for the TK512 operated at -90°C , with

TK 512 CCD Sensor Zero Frames

Different Operating Modes and Environments

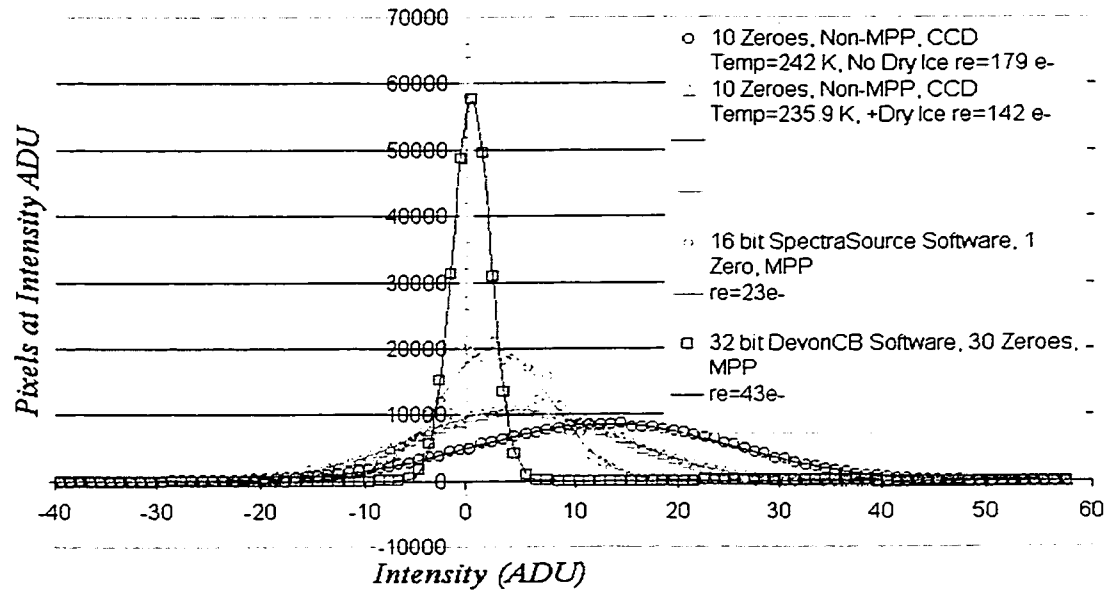


Figure 2.2: Histograms of zero frames obtained in different modes/environments.

a readout clock rate of 50000 pixels s^{-1} . The author has measured a changing level, ranging from $25 e^- < r_e < 47 e^-$ over the period of the last observing season (Sept. 1999 to April 2000). The higher readout clock rate (65000 pixels s^{-1} , quoted by SpectraSource) and the higher operating temperature of the chip (typically -30°C to -50°C) certainly have something to do with this discrepancy, but changing versions of the 32bit camera control library (for use in DevonCB software -see Chapter 3) may be primarily responsible. Prior to Sept. 1999, our software used libraries that did not enable MPP operation of our chip, and the dark current (and hence readnoise) was enormous ($>180 e^-$). The lowest readnoise ($27 e^-$) was reached with the first version of the MPP-enabled library (Sept. 1999): this library turns off the thermoelectric cooler (TEC) while the chip is in readout mode. The author requested a library that did not turn off the TEC during read out, and we received the currently used version on Oct. 4, 1999. The readnoise has been typically $r_e = 40e^-$ since the initial use of this library. It is possible that the cooler-enabled versions produce a higher noise floor, since high current (3-4 Amps) is flowing near the chip during readout. As of July 2000, with dry ice added to the coolant bath, $r_e = 40e^-$ at a CCD temperature $= -40^\circ\text{C}$ is the typical limit of the Devon camera's readnoise. Experimentation with the former camera control library (cooler disabled during readout) is under way.

Currently, CCD's that minimize dark and read noise have implants that allow for Multi-Pinned Phase (MPP) mode, or inverted operation. Dark current is a steady, temperature dependent source of electrons that collect in the potential wells during integration and readout. These are generated by different sources (e.g. impurities within the silicon substrate, and the neutral bulk of the chip itself) but surface generation (Si-SiO₂ interface) of thermally created charge dominates the other processes by two to three orders of magnitude. This source depends on the density of energy states and free carriers (holes or electrons) in the interface. The more interface states available, the more likely that electrons freed from valence bands by thermal agitation are to populate those states, and in turn hop over to the conduction band (where they are collected in the potential wells). The technique of *inverting* the CCD (MPP operation) populates the surface states with holes (that migrate up from the channel stops) by reducing the gate voltage. Holes are thus *pinned* to the surface, and a surface potential of zero is maintained, virtually eliminating electron hopping and the surface contribution to dark current (Janesick et al, 1992).

Non-MPP mode operation allows for significant production of thermal electrons, the rate of which is proportional to temperature (see Figure 2.3). Addition of dry ice to the liquid coolant reservoir helps dramatically when running in non-MPP mode. However, even at maximum cooling efficiency (60° lower than ambient temperature of 11°C) aided with dry ice, the chip is one quarter saturated with thermal electrons after only 1000 seconds integration in this mode.

Figure 2.4 shows the linearity of dark current with time for MPP and non-MPP modes of operation. Tektronix quotes a factor of 10 improvement in dark current levels during MPP operation at -90°C . However, the MPP mode thermal

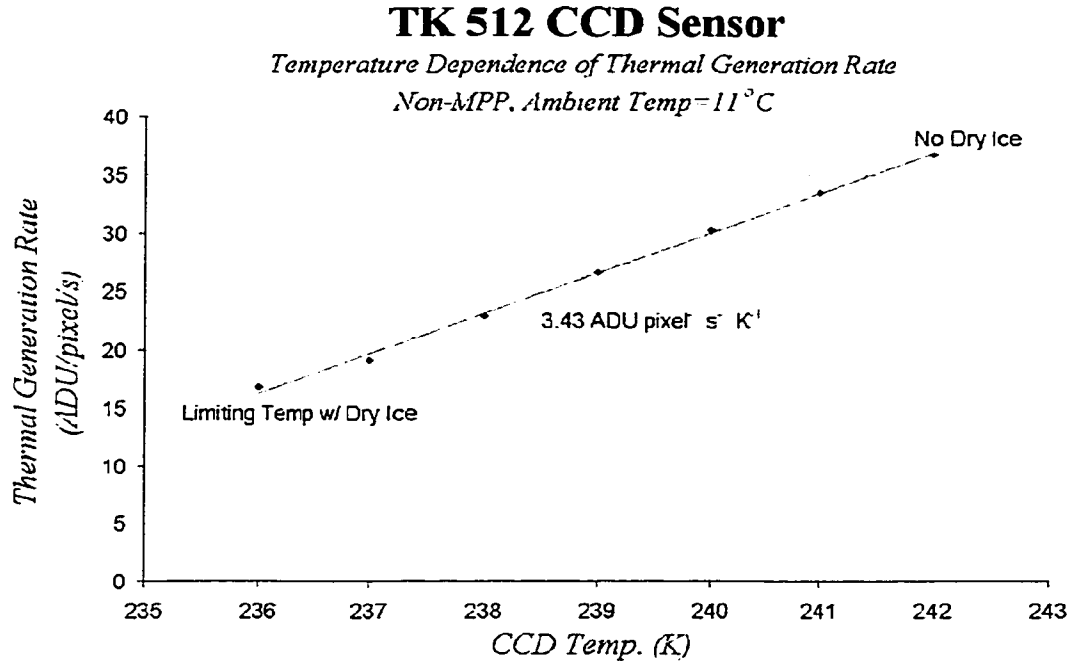


Figure 2.3: Temperature dependence of non-MPP mode thermal generation rate for the Devon TK512 CCD sensor.

generation rate measured by the author ($1.2e^{-pixel^{-1}s^{-1}}$) is two orders of magnitude lower than the rate during non-MPP operation ($173e^{-pixel^{-1}s^{-1}}$), at a typical operating temperature of $\approx -40^{\circ}\text{C}$. No significant change in the thermal generation rate (MPP) with decreasing temperature was measured.

2.5 ACHIEVING OPTIMAL SIGNAL TO NOISE

While cooling the chip to ever decreasing temperatures is desirable from a noise perspective, it can be detrimental to some observing programs, particularly emission line observations of faint objects. On one hand, observing a low surface brightness object through a narrowband filter results in very few photons per pixel, requiring dark and read noise levels to be absolutely minimal. However, quantum efficiency (q_{λ}) is reduced with lower operating temperatures, and this reduction is not linear throughout the visible spectrum. In particular, the red end of a chip's q_{λ} curve is affected more than the blue at lower temperatures (Tucker, 1999). The red lines at $\lambda = 656.3 \text{ nm}$ ($\text{H}\alpha + [\text{NII}]$) and $\lambda = 671.8 \text{ nm}$ ($[\text{SII}]$) are two of the most important for supernova remnants, and q_{λ} drops by $>15\%$ over a temperature reduction of 80K. Choosing an observing target

TK 512 CCD Sensor Mean Thermal Generation Rate

◊ $37.51 \text{ ADU pixel}^{-1} \text{ s}^{-1}$ at CCD Temp. = 242 K, Non-MPP

• $0.26 \text{ ADU pixel}^{-1} \text{ s}^{-1}$ MPP

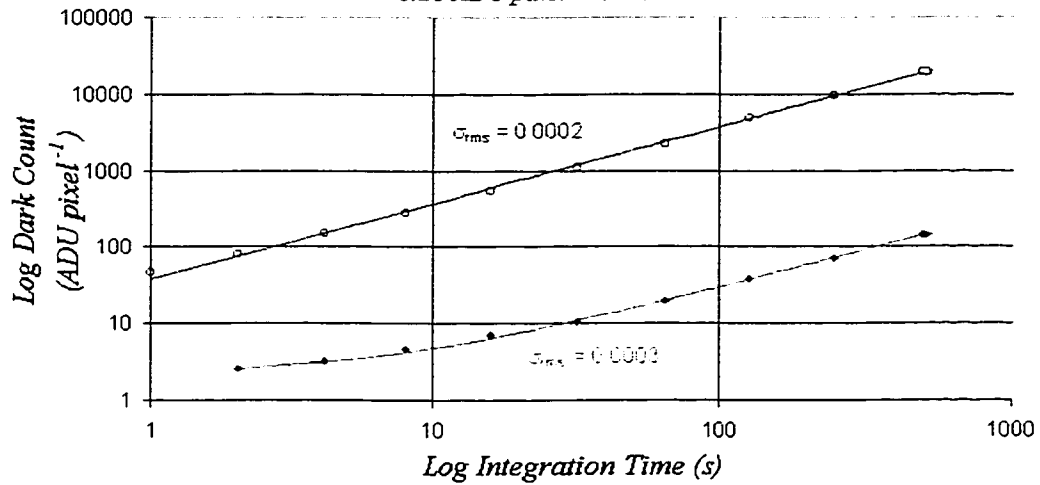


Figure 2.4: Log-log plot of the integration time dependence of thermally generated signal, during MPP and Non-MPP operation. The slope of each line is the thermal generation rate ($\text{ADU pixel}^{-1} \text{ s}^{-1}$) for each mode, values for which are beneath the chart's title. Standard deviation (σ_{rms}) from linearity (solid lines, least squares fit) is labelled for each mode.

thus necessitates choosing a level of cooling to achieve a positive detection with low noise. Individual observations of NRAO 655 for the author's work were performed with 600 second integrations, which generated only 150 ADU of dark current at an operating temperature of -30°C . This integration time was chosen to balance the dark shot noise of $\sqrt{N_{dark}} = \sqrt{150 \times 4.6e^{-}ADU^{-1}} \approx 6$ ADU against the typical readnoise of an image (10-12 ADU) while maintaining a high efficiency ($q_{\lambda} \geq 70\%$ in this temperature range).

The effect of cooling on quantum efficiency is less of a concern when observing stars through broadband filters. Only a moderate level of cooling will be required to lower the dark current level to well below the sky glow, which will probably be the limiting factor. However, higher photons per pixel levels can push an observation into a regime where CCD gain changes as a function of photoelectrons collected. A 16 bit analog-to-digital converter produces the same output ADU value (2^{16}) for inputs beyond $2^{16} \times gain$ electrons ($301000e^{-}$ for the Devon CCD), even if the full well capacity of a pixel has not been reached ($356000e^{-}$). Either condition is called saturation (detector or converter saturation). Prior to reaching a point of zero gain, detectors begin to lose their ability to hold a constant number of electrons per input photon. The author terms this condition *effective saturation*, as the point prior to hard saturation of the detector, but at which photoelectrons are still lost. A good knowledge of the level at which one's detector begins to behave in a non-linear way is prerequisite to precision photometry.

Previously, part of the Devon sensor's dynamic range (5000ADU-45000ADU) was measured by Steinbring, 1995, and this author's current measurements confirm the chip is linear to better than 0.3% over nearly the full range of the analog-digital converter. However, the previous study did not determine the *effective* full well (in e^{-}) of the chip, an important measurement. Figure 2.5 shows the Devon TK512 chip maintains linearity to better than 0.15% in the range $286000e^{-}$ up to $300000e^{-}$, the effective full well of the sensor, and point at which *gain* \neq *constant*. Thus, stars registering levels in excess of $300000e^{-} \div gain(4.6e^{-}ADU^{-1}) \approx 65200$ should be considered saturated with this detector for photometry purposes.

2.6 THE ROLE OF THE DEVON TELESCOPE DESIGN IN S/N AND PRECISION PHOTOMETRY

The chip receives the image from the 0.5 meter $f/3$ mirror, and requires a corrector lens system to produce a coma free, 1° wide image plane. Motion parallel to the optical axis and rotational motion are available for focusing and field rotation respectively. A bar filter slide capable of quick position changes holds five filters for multicolor, rapid time series photometry. Interference and broadband filters used at Devon, and their characteristics, are presented in Table 2.2. The system is housed in a cylinder that also holds the CCD, and is held in the image plane at the prime focus. The environment of the camera is

TK512 CCD Sensor Linearity

Linearity better than 0.2% up to Effective Full Well $\approx 3 \times 10^5 e^-$

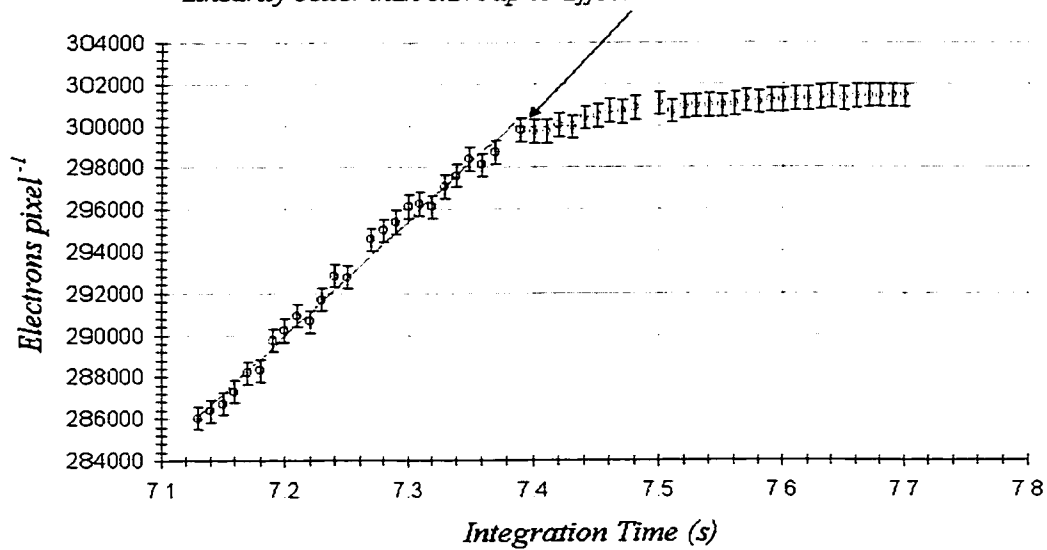


Figure 2.5: The linearity breakdown of the Devon TK512 sensor, measured approaching the effective full well of 300000 electrons.

completely enclosed and filled with dry nitrogen. Condensation and dust are not major concerns, but heat is. To maintain a low dark current, the CCD chip is cooled by a two stage thermoelectric Peltier device, which in turn passes its heat to a liquid chamber within the camera. To remove this heat, liquid coolant is circulated through the chamber out to an external reservoir, for efficient exchange with the surroundings.

The performance specifications of the Devon system are outlined in Table 2.3. The optical design is reminiscent of a slow Schmidt camera, and is unique among those operating in the Country. The wide field ($0.5^\circ \times 0.5^\circ$) provided by the fast optical system and chip size is sufficient for many of the large objects (SNR's and HII regions) found in the CGPS data. The excellent optics used in the Devon telescope design are important for resolving fine structure in these faint extended objects, but small stellar images are not needed for photometry. The Devon system produces very sharp stellar images. A Gaussian fit to the *Point Spread Function* (PSF, or the stellar profile in a CCD image) measures the typical FWHM as 1.5 - 2 pixels (the 4-6" seeing limit of the Devon site). The PSF therefore has a width $\sigma < 1$ pixel. What role does such a small image play in precision photometry?

The standard measure of the Point Spread Function (PSF, or the stellar profile in a CCD image) is a Gaussian. One integrates this function over the area of a circular aperture (radius r) to obtain the encircled energy (EE):

$$EE(r, \sigma) = \int_0^r \int_0^{2\pi} \frac{1}{2\pi\sigma^2} e^{-\frac{r^2}{2\sigma^2}} r dr d\theta = 1 - e^{-\frac{r^2}{2\sigma^2}} \quad \text{eq. 2.2}$$

The systematic error associated with this aperture radius is thus:

$$dEE(r, \sigma) = \frac{r}{\sigma^2} e^{-\frac{r^2}{2\sigma^2}} dr \quad \text{eq. 2.3}$$

As can be seen in equation 2.3, increasing the width of the PSF (σ) is advantageous from an error perspective (Mighell, 1999). As well, Poisson statistics force one to use many pixels when determining a star's flux in a photometric aperture. The S/N of a stellar image in the absence of instrumental errors increases as $\sqrt{N_*}$ (where N_* is the total counts collected in the star image), and a larger PSF allows longer integrations, increasing N_* (very important for low S/N ratios). One can increase the pixel area of a stellar image by slightly defocusing. In addition to increasing N_* , defocused images are less prone to saturation, and are easier to centre. The Devon telescope design, thus, is not optimal for stellar photometry, but can be adjusted by the defocusing technique.

Equation 2.4 (Howell et al., 1992) presents an important term that deals with the error associated with the sky determination, $\left(1 + \frac{n_{pix}}{n_B}\right)$, where $n_{pix} \equiv$ total number of pixels used in photometric aperture, and $n_B \equiv$ total number of pixels used in background determination (All other terms in eq. 2.4 are discussed throughout this chapter).

$$\frac{S}{N} = \frac{N_*}{\sqrt{N_* + n_{pix} \left(1 + \frac{n_{pix}}{n_B}\right) (N_{sky} + P)}} \quad \text{eq. 2.4}$$

$$P = N_{dark} + r_e^2 + gain^2 \sigma_f^2$$

where $\sigma_f \equiv$ quantization, or digitization noise (Newberry, 1999), and P is the instrumental noise term.

Name of Band/Line	$\lambda_C (\pm 1nm)$	FWHM ($\pm 0.5nm$)	Type
U	365	70	Broadband
B	440	100	Broadband
V	550	90	Broadband
R	700	220	Broadband
I	880	240	Broadband
[OIII]	502	5.4	Interference
Continuum	609	13.6	Interference
[OI]	630	4.8	Interference
H α + [NII]	656	7.5	Interference
[SII]	672	5.0	Interference
[Si III]	907	5.5	Interference
[Si III]	953	6.0	Interference

Table 2.2: Broadband and Line Filter Characteristics for the Devon Telescope System. Each filter is 50.8 mm in diameter.

To minimize the contributions of instrumental noise (\sqrt{P}) and Poisson sky noise ($\sqrt{N_{sky}}$), one must always use more sky background pixels than n_{pix} , while keeping the measuring aperture small ($FWHM \leq r \leq 3 \times FWHM$ is recommended).

Faint, extended object imaging in emission line filters is the Devon system's specialty by design. Observations in narrowband filters suffer from low object (N_{obj}) and sky (N_{sky}) counts, but similar instrumental noise levels (\sqrt{P}). One method of increasing the S/N when observing faint extended objects is compositing, discussed in Chapter 4. In any method, minimizing instrumental noise contributions by cooling the detector as cold as an appropriate q_λ allows will aid in achieving reasonable S/N values. Photometric measurements of extended objects, by nature, will use larger numbers of pixels in a non-circular aperture (n_{pix}). Thus, measurements through polygonal apertures should use large numbers of sky pixels (n_B) for determination of background levels.

2.7 DATA REDUCTION OF DEVON AO IMAGES

We now turn to a brief description of the appropriate reduction steps to apply to Devon AO data. For further information on these steps and how they are accomplished in software, the reader is referred to Gilliland, 1992, and Chapter 3 of this work. Reduction of additive/multiplicative noise present in CCD images proceeds in reverse order of the successive addition of each noise source to the frame, created in the integration/readout process. Thus, the first step in the reduction process (typically pedestal level removal, or *overscan*) removes noise generated at the last stage of CCD frame readout.

The very last artifact added to a CCD image is known as the *overscan*, and is the first to be removed. The overscan is a measure of the electronics

D_{mirror}	0.5m
f ratio	3
%Area obstruction by camera housing	>20%
Effective f ratio with 2 element field corrector	3.45
CCD chip scale	$3''.1 \text{ pixel}^{-1}$
Field size (measured)	$27'.1 \times 27'.1$
Typical Stellar Image FWHM (measured)	1.5-2 pixels
Bits pixel^{-1}	16
Gain (measured)	$4.6 e^- \text{ ADU}^{-1}$
Mean Readnoise (measured)	$25-40 \pm 2 e^-$
CCD Linearity Range (measured)	10 ADU - 65200 ADU
Mean thermal generation rate (241 K)	$173 e^- s^{-1} \text{ pixel}^{-1}$ (non-MPP) $1.2 e^- s^{-1} \text{ pixel}^{-1}$ (MPP)

Table 2.3: Devon Telescope/CCD Camera System performance specifications.

bias level added to all pixels during the sequential shifting of pixels. Essentially, this level indicates how many quantification units (ADU) are present in empty, unexposed pixels. To measure this, one continues to read out the CCD past its physical extent, where, in effect, one is reading the CCD's amplifier. A mean level per image is found (see chapter on DevonCB Software for the method) and subtracted from that image.

The overscan is a changing level that varies with time, telescope position and ambient temperature. However, many CCD cameras produce a two-dimensional stationary electronics pattern across the chip (a non-varying component of the electronic bias level). Further, readout time is a finite length and, during readout, charge accumulation (from thermal sources, light leakage, etc) produces another bias level in empty, unexposed pixels. One should always verify whether a significant *zero* pattern exists, and work to remove any non-stationary interference (e.g. RFI banding) before considering this reduction step as necessary. If no pattern exists, a histogram of the mean of many zero frames will reflect only the readnoise, and no zero subtraction is necessary. With an electronically quiet camera and a well-cooled chip, this additive zero level may not be significant, but verifying this by collecting zero frames is wise. The author has always found zero removal necessary for Devon AO data, especially if targets are located near the edges of the object frames.

Electrons that thermally 'hop' from the Si-SiO₂ interface of the CCD chip to the conduction band accumulate in the potential wells of each pixel. This release of e^- is constant with time, and causes the third additive artifact, the *dark* count. The linearity of this process makes it relatively straightforward to account for; one integrates the CCD with the shutter closed for some time to collect dark frames. The mean dark map is then subtracted from the object images after scaling it to the object's integration time. This is the removable component of dark noise; what remains is dark shot noise ($\sqrt{N_{dark}}$), and is Poisson in nature. This therefore becomes an irreducible contribution to one's

error budget, and minimizing the dark charge per pixel (by cooling or other means) reduces this.

For detection of faint, extended objects, the most important calibration of a CCD image is *flat fielding*. Individual pixel variations in quantum efficiency account for small scale differences, while an obstructed optical path in the telescope causes large scale gradients in the background of the image. This effect is a multiplicative scaling of sensitivity. One collects images of a uniformly illuminated surface, and a division of the object frames by the mean flat field is performed. If the observed sky background in object frames is relatively even, a uniform background on which faint nebulosity can be more easily seen results. Flat field calibration always removes sensitivity variations, but other scattered light can cause gradients in the background level of the calibrated image. If, for example, the object image was obtained near the bright moon or through an auroral display an uneven, residual field illumination is left which cannot be removed by this calibration step. Detecting faint nebulosity is difficult to impossible in such contaminated fields, thus the need for dark sky conditions while observing faint, extended objects.

2.8 PHOTOMETRIC PERFORMANCE OF THE DEVON SYSTEM

The preceding portion of this chapter is devoted to presenting measurements of the Devon system's characteristics. As well, this chapter has detailed the noise sources to be aware of, and the observing and reduction procedures to be followed to minimize them. The remainder of the chapter is devoted to the photometric capability of the Devon system. Observations of a variable star under typical sky conditions were performed and reduced by the author, using these techniques. Aperture photometry results are presented here as a demonstration of the Devon system's performance.

Observation, camera and data details are presented in Table 2.4. The evening's observations began with collecting 40 twilight sky flat fields in the V filter, made with the telescope pointed overhead. The telescope was offset slightly between flats to move unseen stars around the frame, and the flats were all exposed to >80% full well (>50000 ADU). While awaiting darkness, 20 dark frames of 200s each (half of the target integration time) were prepared. During each readout the camera's TEC is disabled, and so a delay between dark exposures of 30 seconds was used, to allow time for the chip's temperature to stabilize. A series of twenty 400s integrations were then performed on BL Cam, with the target consistently positioned on the same pixels for all frames. The telescope was slightly defocused for these data, spreading the stellar FWHM to 5-6 pixels. Finally, 50 zero images were collected after target observations ceased. A delay between zero frames was again used.

About half way through the target observations, a bright auroral display contaminated several frames, doubling the sky background in some. Later,

Target (V)	BL Cam
Magnitude (mean)	$m_V = 12.8$
Check Star (C1)	GSC 4067 723, $m_V = 11.8$
Comparison Star (C2)	GSC 4067 350, $m_V = 12.4$
Coordinates (J2000)	$\alpha = 3^h 47^m 19^s$ $\delta = 63^\circ 22' 48''$
Filter	V
Integration	400s
Date of Observation	26/01/2000
Time (GMT)	04:18:39 - 06:28:08
Camera Gain	$4.6 e^- ADU^{-1}$
Readnoise	$42 e^-$
Mean Dark Count	$1 e^- pixel^{-1} s^{-1}$
Typical Target S/N	222
Typical Stellar FWHM	5 pixels

Table 2.4: Details of Devon AO test observations of BL Cam, a SX Phe. type variable star.

BL Cam was found to lie within a “halo” of a nearby field star of magnitude $m_V = 5.4$, which further increased the sky noise. The author believes this halo is the out-of-focus star image reflected at the surface of the optical window (in front of the chip by 2.1 cm), imaged by the camera.

Aperture photometry was performed on BL Cam and two other stars of similar brightness in the reduced object images. The aperture radius was chosen as $r = \text{FWHM}$ (for reasons fully discussed in Mighell, 1999), and used for all three stars. Figure 2.6 shows the time-series lightcurve data of BL Cam, in which differential magnitudes (V-C1) and (C1-C2) are plotted. The scatter of C1-C2 (standard deviation) throughout the sequence is $\sigma = 0.0034$, or 3 millimagnitudes. Even through changing bright sky conditions, the Devon CCD system is capable of delivering photometric precision on the millimagnitude level.

It was primarily the author’s responsibility to bring the Devon system to an operational state, and to produce the productive working environment now enjoyed at the DevonAO. The Devon telescope/CCD system currently is able to perform photometric observations at the millimagnitude level of precision. The observer should be familiar with the above chapter, and following careful and informed observing and reduction procedures will ensure accurate photometric work is accomplished. Following the above proven success, the Devon system’s capability for faint, extended object detection and measurement in optical emission lines is shown in Chapter 5.

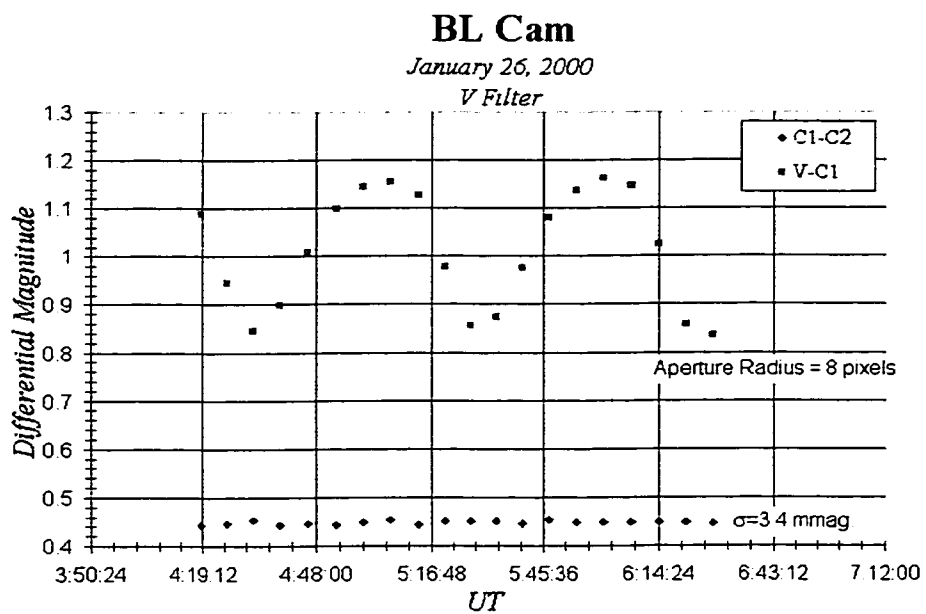


Figure 2.6: Results of aperture photometry performed on the SX Phe. variable star BL Cam.

2.9 REFERENCES

Janesick, J. and Elliott, T. **History and Advancements of Large Area Array Scientific CCD Imagers.** From *Astronomical CCD Observing and Reduction Techniques*, ASP Conference Series (Steve B. Howell, editor), Vol. 23, 1992, 1.

Gilliland, R. L. **Details of Noise Sources and Reduction Processes.** From *Astronomical CCD Observing and Reduction Techniques*, ASP Conference Series (Steve B. Howell, editor), Vol. 23, 1992, 68.

Howell, S.B. **Introduction to Differential Time-Series Astronomical Photometry Using Charge-Coupled Devices.** From *Astronomical CCD Observing and Reduction Techniques*, ASP Conference Series (Steve B. Howell, editor), Vol. 23, 1992, 105.

Massey, P., and Jacoby, G. H. **CCD Data: The Good, the Bad, and the Ugly.** From *Astronomical CCD Observing and Reduction Techniques*, ASP Conference Series (Steve B. Howell, editor), Vol. 23, 1992, 240.

Mighell, K.J. **CCD Aperture Photometry.** From the *CCD Precision Photometry Workshop*, ASP Conference Series (E. Craine, R. Tucker and J. Barnes, editors), Vol. 189, 1999, 50.

Newberry, M. **Increasing Precision and Accuracy in Photometric Measurements.** From the *CCD Precision Photometry Workshop*, ASP Conference Series (E. Craine, R. Tucker and J. Barnes, editors), Vol. 189, 1999, 50.

Tucker, R. A. **Some Practical Aspects of CCD Camera Construction.** From the *CCD Precision Photometry Workshop*, ASP Conference Series (E. Craine, R. Tucker and J. Barnes, editors), Vol. 189, 1999, 24.

Steinbring, E. *The Devon Observatory CCD Imaging System and its Applications to Photometry of the Ellipsoidal Variable HR 4646.* M.Sc. Thesis, University of Alberta, Edmonton, 1995.

Chapter 3

DEVONCB SOFTWARE

3.1 SUMMARY

Software development was undertaken by the author to provide a scientifically rigorous system to obtain, process, and analyze images obtained at the Devon Astronomical Observatory (Devon AO). This chapter describes the design of DevonCB, the organization of its interface and the software's features. The main form and intention of its design are described. The interface is broken down into distinct functional families, each of which is separately illustrated. Visualization and measurement functions and their algorithms are discussed. Techniques of astronomical CCD observing and reduction are presented throughout this entire work. This chapter is meant to serve twofold: as a manual documenting the features of DevonCB, and as a guide to using DevonCB for a successful night's observing at the Devon AO.

3.2 INTRODUCTION TO DEVONCB

The successful research conducted by the author in part relied upon efficient observing sessions at the DevonAO and equipment working at peak performance. In addition to hardware development and installation at Devon (covered in the preceding chapter), such an evening could only be realized by producing an observer-friendly interface for computer control of this hardware. The purchase of the SpectraSource HPC-1 CCD camera included software for simple image taking, but lacked an easy means to obtain a stream of accurately timed stellar or faint object images. Quality data acquisition (e.g. precision photometry) is as much a function of observing techniques as it is of good equipment. To realize this, the observer needs to devote more time to this skill, without having to worry about software shortcomings. Thus, the research undertaken necessarily included development of professional standard software for telescope and camera control.

The ultimate goal of developing DevonCB was to allow an observer to concentrate on the data, rather than the operation of acquiring it. Useful CCD data begins with the observer keeping an eye on the data coming in from the telescope, looking at each image for non-linearity, sky noise and radiation events, spontaneous defocusing and tracking errors, and other problems. Obtaining precision measurements of astronomical light from a CCD is truly an art, and begins with good observing techniques. For a discussion on the

art of obtaining CCD data, refer to Massey et al., 1992. Automated observing through intuitive software control is deemed most important by the experience of the author, and is liable to increase one's chances of taking home useful CCD data.

DevonCB was developed in the C++ programming language. Although this guide was written for the Tektronix TK512 CCD chip, the software will handle chips with different pixel dimensions. However, only the control library for the HPC-1 camera is supported. Other system requirements for DevonCB are listed in Table 3.1. Memory requirements are the most stringent. DevonCB uses several megabytes of memory to store the master frames for the Auto Calibration routines. As well, the software can be used to combine many images together into a single one, and requires memory to store each frame. The computer will slow down significantly if one tries to average together 50 frames or more with only 32 megabytes of RAM.

Some of DevonCB's advantages are listed below. All are discussed thoroughly in various sections throughout this guide.

- Uses advanced features (e.g. Multi Pinned-Phase, MPP) for very low noise operation.
- Ability to create an automated observing queue, with single/multiple exposures of variable length & filter settings.

Operating System	MS Windows 95/98
Processor Class	Pentium 133 MHz (minimum); Pentium II 333 or > recommended.
Hard Disk Space	4 MB
Memory	32 MB minimum; recommend 64 MB or more to use Image Combining and Auto Calibration features.
Camera System	SpectraSource HPC-1 + control library (independent of CCD chip installed)
Display	1024x768, 16 Bit. Large Font (120 dpi) recommended.

Table 3.1: Minimum recommended system requirements for DevonCB Software.

- Complete astronomical record of every image written into a customizable image header, plus conformity to the Flexible Image Transportation System (FITS) image standard.
- Enhanced image processing and arithmetic operations, plus automated image combining algorithms to produce master bias, dark and flat calibration frames.
- Automatic calibration of CCD frames in real time.
- Complete aperture photometry package allowing for onsite photometric measurement of stellar data.

3.3 AN OVERVIEW OF THE INTERFACE

The interface of DevonCB is presented to the user upon starting the program. The main form is constructed of various individual windows, each parenting a separate family of program functions. Each window has caption text of a different colour. Figure 3.1 presents the interface, with Table 3.2 listing each control window and its descendant functions. The form design is intended to place *all control and image processing functions* that the user could be expected to employ within a common control interface.

The user then need not hunt for nested functions, and is free to monitor and explore the incoming data with image processing while maintaining camera control. The interface has been criticized as being cluttered, but experience has shown that the principal observers at Devon adapt to it quickly and easily.

The image box displays the 547×512 pixel array that holds the real data pixels plus overscan. Double clicking on this image will present the user with a dialog box to load and display another image. One should note that loading an image displays that image's header information in appropriate boxes on the form, replacing existing entries with its own. Only the boxes within the Header Information window and the EXPTIME box in the Single Exposures window are written into. This offers a quick way of viewing a previous image's attributes.

The image coordinates and corresponding pixel value (in ADU) are updated in boxes labeled IC and PV (in the Status window) while moving the mouse around in the main image. Automatic display of these values as the mouse moves can be switched to a mouse clicking operation from the **Image Measurement→Pixel Value Display** menu option. Clicking the mouse on the main image can also perform image centroiding and aperture photometry on the pixels around the cursor's centre (see description of photometry routines later in this chapter) if the menu item **Image Measurement→Quick Photometry** is checked.

Astronomical information associated with each frame is displayed alongside the image, as are statistics of the image itself. The central location was chosen due to the important role these data play in quickly assessing a frame's quality. Basic image processing routines (Brightness, Contrast and Histogram Equalization) are located directly below the image, separate from the other functions. These functions (in particular histogram equalization) are very useful for quickly stretching low contrast images to a broader dynamic range, to see hidden objects.

Status	Astronomical and statistical information associated with the current frame.
Configuration	Controls the filename base and extension of an auto-saved image.
Header Information	Observer, object, filter and camera information to be saved in the image header.
Image Processing	Image brightness and contrast scaling, filters, and mathematical image operations.
Auto Calibration	Automatic image reduction using overscan, zero, dark, flat field and deferred charge calibration frames.
Filter	Displays filter used for current image.
Single Exposures	Enables the user to obtain a stream of identical time/type exposures, and combine these into one master frame. As well, controls what type of exposure is performed.
Multi-Exposures	A programmable queue to automatically obtain a stream of different integration time exposures of a single type through different filters.

Table 3.2: Description of primary function areas of the DevonCB interface.

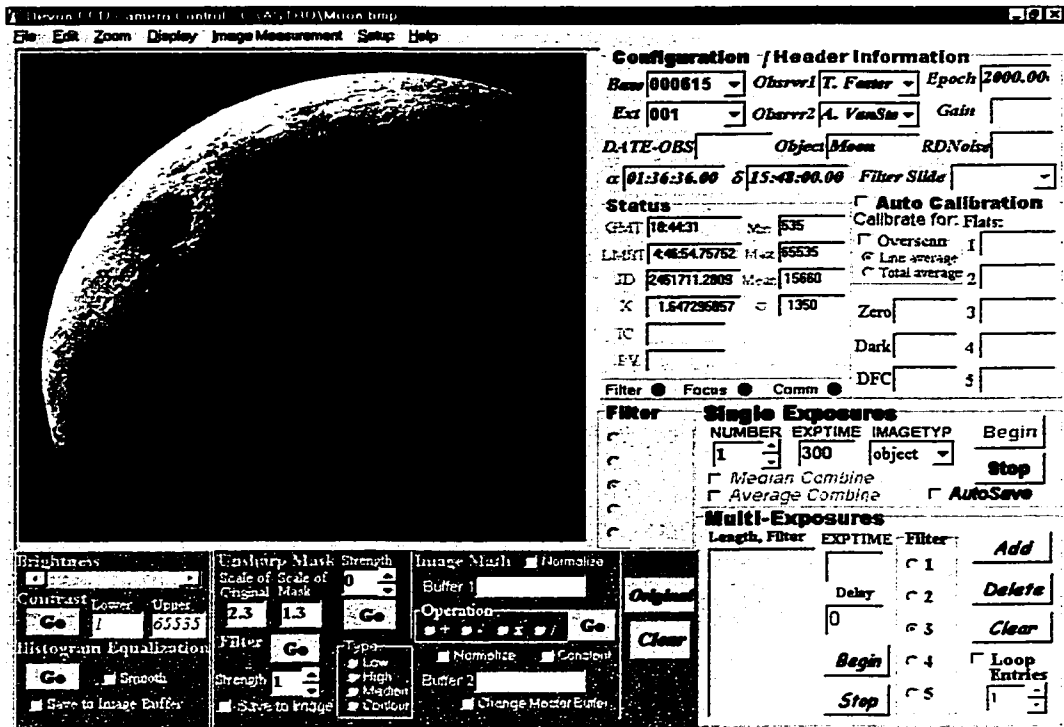


Figure 3.1: The window interface of DevonCB. Note the field of the Devon CCD covers most of the Moon ($\sim 1/2^\circ \times 1/2^\circ$).

Single and multi-exposure control boxes are grouped together on the bottom right half of the screen, and share some of the same entries (e.g. delay box). They are intended to work together, and their design is intentionally simplified to avoid distraction from the data. Handily placed next to them is the Filter button group, to see easily which filter one is working in or to change the filter for a new exposure. Header information boxes are clustered together at the top right. The user can enter information in these boxes: e.g. the object name, the coordinate (α, δ) location of the field centre, and the date of the observation. This information is recorded in the header of every image saved thereafter.

Functions not available in the immediate window environment were deemed secondary functions, and were placed in the menu bar along the top of the form. They are still easily accessible, and were considered less important to the principal goal of allowing the observer to scrutinize the incoming data. The menu items are listed in Table 3.3, along with descriptions of their descendant functions.

Certain menu items are disabled if no FITS data are loaded, meaning these functions are not appropriate for graphics files. For example, the FITS header editor displays only if FITS data are present.

File→Open FITS Open Graphic Save FITS Save as BMP Print Print Setup	Loads and displays header and data contained in a 16-bit FITS file. Displays a standard bitmap Write current image data/header information to 16-bit FITS file. Save the current screen to a bitmap graphic. Print the displayed image to the Windows default printer. Standard Windows printer setup dialog box.
Edit→Edit FITS Header Clear Image Display	Loads a FITS Header Editor window, for customized Header entries. Removes all pixel data from memory and screen, clears Header entries.
Zoom→ 50% To 800%	Displays FITS image or graphic at various screen magnifications, from 50% to 800% actual size. Scroll box appears on the display to move around the zoomed image.
Display→Greyscale/ Aqua Invert Magnifier	Alternately displays data in 16-bit greyscale and Blue-Green Palettes. Blue-Green palette is useful for seeing faint patterns in the image/noise. Inverts greyscale image: useful for seeing faint objects and Nebulosity. 2× magnifying box attaches to cursor: can quickly inspect image areas.
Image Measurement→ Quick Photometry Pixel Value Display Find Gain/Readnoise	Opens Photometry box first to allow magnitude filename entry and aperture selection, then reopens on each click of image, displaying photometric results to screen and writing information to a magnitude file. Toggles display to IC and PV Status boxes from mouse motion or click. Finds camera gain and readout noise with appropriate zero and flat frames entered; uses equations 3.1 and 3.2.
Setup→ Initialize Camera Initialize Camera Controls Rotate Camera Angle Cooler Camera Status Focus CCD COMM Settings Low Gain Observatory	Flushes CCD sensor of charge, closes shutter and starts camera cooler. Centres filter slide, moves camera to focus limits, back to original focus. Not yet implemented; rotates camera to an angle between 0° and 45°. Toggles CCD thermoelectric cooler on/off. Reports status of cooler and shutter mechanism. Opens box enabling fine (0.125mm) and coarse (1mm) focus adjustment. Opens COMM Settings box; change communication port address/speed. Toggles CCD to low/high gain mode. Default = Low gain. Opens box enabling entry of geographical location (L, φ) of observatory.
Help→ Help About	Opens this manual. Box displaying version, author and date information.

Table 3.3: Menu Items from the main DevonCB form and their nested functions.

3.4 DESCRIPTION OF PRIMARY FUNCTIONS

We now turn to describing each of the seven primary function areas, which collectively form the interface of DevonCB. To better understand how to use the software for a productive observing session, we will detail each sub-function within a function area. **Bold text** indicates the name of the described feature as seen onscreen.

STATUS WINDOW

- **GMT** Greenwich Mean Time, defined as $GMT = LMT + \text{timezone}$, or $LDT - 1.0 + \text{timezone}$.
 - **LMST** Local Mean Sidereal Time, or the right ascension of one's celestial meridian. $LMST = GMST - \text{west longitude}$, where GMST is defined by Meeus.
 - **JD** Julian Date. Day number since Jan. 1, 4713 BC, measured at Greenwich. Julian Day begins noon GMT.
 - **X** Airmass of object being observed, defined as $X \sim \sec(z)$, where $z \equiv$ object's angular distance from zenith.
 - **IC, PV** Image coordinates and pixel value at cursor position. Use this to inspect your stellar images for over-clocked pixels.
 - **Min, Max** Minimum and maximum pixel values in physical data. Can range from $(2^0 - 1)$ to $(2^{16} - 1)$ ADU for a 16-bit image (0-65535). Written to FITS header as PIXMIN and PIXMAX.
 - **Mean, σ** Mean pixel value and RMS standard deviation of pixel values in physical data.
 - **Im#, ETL** Image number being exposed; Exposure Time Left in current integration (in seconds). ETL will indicate the time left in either the current integration or the delay between exposures. These boxes are not visible unless an integration is being performed.
- LED's at bottom are green when camera or filter is in motion and red when they are not. All information from the Status box is recorded in FITS header on saving the array. For accuracy, astronomical times (GMT, JD, LMST) are written prior to readout of the chip.

- Status			
GMT	18:44:31	Min	535
LMST	4:46:54.75752	Max	65535
JD	2451711.2809	Mean	15660
X	1.647295857	σ	1350
IC			
PV			

Filter ● Focus ● Comm ●

CONFIGURATION WINDOW

- **Base, Ext** Base filename and extension number of file to be Saved, where **Base** = yymmdd (local date). Default saved filename is "yymmdd-Ext". **Base** configures itself to an appropriate value on program start; Extension number automatically increments with each saved image. Other extensions (e.g. .FITS, .FITS) are available for **Ext**.

- Configuration	
Base	000615 ▾
Ext	001 ▾

HEADER INFORMATION WINDOW

- **DATE-OBS** Greenwich date image array was created, defined as dd/mm/yy. Configures self on program start.
- α, δ Right ascension and declination of field centre, defined at **Epoch**. Recorded in FITS header as values for RA, DEC keywords.

-/ Header Information			
Observer1	T. Foster ▾	Epoch	2000.00
Observer2	A. VanSte ▾	Gain	
DATE-OBS		Object	Moon
α	01:36:36.00	δ	15:43:00.00
		Filter Slide	▾
		RDNoise	

- **Observer1, Observer2** Name(s) of principal observer(s).
- **Epoch** Equinox of coordinates used in α , δ . Defaults to 2000.000.
- **Gain, RDNoise** Camera *gain* ($e^- ADU^{-1}$) and readout noise (e^-). Can be previously known (and entered manually), or calculated by the user with menu item **Image Measurement**→**Find Gain/Readnoise**. Results are entered here automatically, and are thereafter written to the image header as GAIN, RDNOISE.
- **Filter Slide** Filter sequence of slide currently in telescope. Changing this updates the labels in FILTER, and writes to FILTERS keyword in FITS header.

AUTO CALIBRATION

This is a very powerful set of algorithms for real time CCD reductions on site. When **Auto Calibration** is checked, all images made at the telescope thereafter are partially or wholly reduced before being saved to disk, depending on the user's choice of the following:

- **Overscan** If this box is checked, the program will determine an average overscan value to subtract from the physical data. The overscan is an array of values that fluctuate about a mean level. It is an additive level to the readout of every pixel on the chip, and hence biases a pixel's true count. Overscan data are read out after each row of the CCD array of real data, by simply reading beyond the physical extent of the chip. In effect, one is reading the CCD amplifier. Since this bias level can change with telescope position and ambient temperature, it is individually read for every image made. DevonCB reads 547 pixels for each row (for a 512×512 array chip), thus producing a 547×512 array of data in the saved FITS image. DevonCB will subtract the average overscan determined on a row by row basis (using **Line average**), or the average of all overscan data (**Total average**). See Gilliland et al., 1988 for a discussion of both techniques. It is possible for this bias to vary as a function of time during readout: if your images show slightly different overscan levels at the first and last readout rows, use **Line average** to determine the mean overscan level.
- **Zero** If this box displays a filename, the frame in this buffer will be subtracted from every image made. To create a mean zero frame in this buffer, make several (> 25) overscan-subtracted zero frames, and combine them together using **Average Combine** in the Single Exposures window. To load a previous overscan-subtracted zero frame in the buffer, click this box. To clear the buffer, click and select "Cancel". While overscan is a dynamic bias level, the zero frame is meant to be a picture of static pixel to pixel bias levels. Static patterns may remain in overscan-subtracted frames, and a zero frame should show this. Reading out the CCD sensor, after flushing it of charge makes a zero frame. If your overscan-subtracted zero frame has a mean value near 0 and no pattern to it, then this calibration is not necessary, and may add more noise to your final image (see Gilliland, 1992).
- **Dark** If this box displays a filename, the frame in this buffer will be scaled to **EXPTIME** (in Single Exposures) and subtracted from every image made. To load a previous (overscan and zero corrected) dark frame in this buffer, click the box once. To create one,

Auto Calibration	
Calibrate for: Flats:	
<input type="checkbox"/> Overscan	1 <input type="text"/>
<input checked="" type="radio"/> Line average	
<input type="radio"/> Total average	2 <input type="text"/>
Zero	3 <input type="text"/>
Dark	4 <input type="text"/>
DFC	5 <input type="text"/>

make several (>10 overscan and zero corrected) dark frames of the longest exposure time you expect to use, and combine them using **Median** or **Average Combine** (both eliminate cosmic ray events). Save this master dark frame, and load it into **Dark**. Since the program scales the frame in the buffer before subtracting, one should not use a dark that is not bias corrected, as the bias level in a CCD is not a function of time, and hence should not be so scaled. The amount of dark charge in a CCD pixel is a linear function of time (see previous chapter), and is unique to each pixel. Dark charge accumulates from a current of thermally created electrons. A map of this dark count over the CCD array, made by integrating the CCD with the shutter closed, is subtracted from the target image after being scaled to an identical exposure time.

- **Flats** These five boxes display the names of corrected flat fields for each of (up to) five filters used in one's observing program. These flat fields are normalized (mean =1.0) and are divided into one's object images. The program determines in what filter an image was made and applies the appropriate flat field correction. Flats entered here should be corrected with prior reduction steps (overscan and zero bias levels, dark count). A flat field is the CCD image of a uniformly illuminated surface. It therefore maps out *a)* small-scale pixel to pixel gain variations, and *b)* large-scale gradients caused by uneven illumination of the chip by optical path imperfections. Make several twilight sky flats (corrected) in each filter, with the telescope pointing slightly offset for each (thereby moving star images around the frame). Combining these using **Median Combine** produces a star free master flat field.

The first four boxes are also used as temporary buffers for calculating CCD gain and readout noise. Box 1 and box 2 hold two similar unprocessed zero frames (Z_1, Z_2) while boxes 3 and 4 hold two similar raw flat fields (F_1, F_2). If one must use twilight sky flats, one should ensure they were made with identical light conditions and exposure times. Equations 3.1 and 3.2 are used to calculate *gain* ($e^- \text{ADU}^{-1}$) and read noise r_e (e^-) from the average levels of the frames and the RMS standard deviation of their differences ($\sigma_{F_1-F_2}, \sigma_{Z_1-Z_2}$). One simply enters the required images, and selects the menu item **Image Measurement**→**Find Gain/Readnoise**. Gain and read noise are automatically entered in the FITS header of every image thereafter.

$$gain = \frac{(\overline{F_1} + \overline{F_2}) - (\overline{Z_1} + \overline{Z_2})}{\sigma_{F_1-F_2}^2 - \sigma_{Z_1-Z_2}^2} \quad \text{eq. 3.1}$$

$$r_e = \frac{gain \cdot \sigma_{Z_1-Z_2}}{\sqrt{2}} \quad \text{eq. 3.2}$$

- **DFC** If this box displays a filename, the *Deferred Charge* frame in this buffer will be added to every image made. Deferred charge (or non-linearity at low charge levels) is a pixel to pixel variation of the response to photoelectron creation. The DFC frame is a map of "missed" (or deferred) ADU over the CCD array that is added to one's object frame. Making a DFC map is not trivial (consult Gilliland, 1992), but only needs to be done once. This is the last reduction step to be applied, since it is the first instrumental

problem encountered in the integration process. It is often ignored, but is important if one's target falls on different areas of the chip throughout a night's data set.

A hidden danger to photometric precision is measuring star images containing one or more non-linear (*gain* ≠ constant) pixels. Saturated pixel values could be *lowered* to a non-saturated condition by division by a flat field pixel > 1.0 ADU, and treated as a normal pixel in photometry. All **Auto Calibration** functions selectively treat data values, and will not modify non-linear pixels.

SINGLE EXPOSURES

This window controls what type and how long a CCD exposure is, and how many subsequent integrations are to follow. It performs the integration, saves and combines images by mean or median measures.

- **NUMBER** To obtain multiple exposures of the same exposure time, this box must display integer $N > 1$. These N exposures can be successive with no pause between them, or separated by a user-specified delay (as found in **Delay**, MULTI-EXPOSURES window).
- **Average, Median Combine** When $N > 1$, the user is offered the choice to combine them by average or median algorithms. The combined image is saved with the header keyword **NCOMBINE = N**. Because individual buffers are created in memory to hold

$$\bar{X} = \frac{\left(\sum_{i=1}^N X_i \right) - (X_{>} + X_{<})}{N - 2}, \quad N > 2 \quad \text{eq. 3.3}$$

each of N frames, this process can be very memory and CPU intensive. Be patient when combining a large number ($N > 30$) frames.

Averaging is useful for combining images with minimal differences between them (e.g. zeroes). However, the algorithm used by DevonCB (equation 3.3) reduces the mean's sensitivity to extreme values by removing the highest and lowest values from the array, before computing the arithmetic mean. For each location (x,y) in a frame, the i 'th pixel, carrying value X_i (ADU), is summed over the array of N images. The summed value is reduced by the sum of the highest and lowest pixel values ($X_{>} + X_{<}$), and divided by $N-2$ frames. The resulting image is unlikely to be affected by cosmic ray events present in one of N pixels.

One can also combine images by median algorithm. The median is less sensitive than the mean to extreme values (e.g. radiation events). It is useful for combining frames certain to be affected by cosmic rays (e.g. darks), or other sporadic values (e.g. a series of twilight flats offset from one another to move star images around). One can also employ the *shift and stare* technique (Tyson, 1988) to create a *superflat* image (Gullixson, 1992) by setting a delay and offsetting the telescope slightly between exposures. The median image of this series is free of stars, and shows the background illumination pattern of one's field. The algorithm sorts an array of N values from the i 'th pixel (X_i), in ascending order. If N is odd, the central pixel is then the median of the array. When N is even, the mean of pixel $N/2$ and $N/2+1$ is taken as the median value.

- **EXPTIME** The integration time of the image, written into the header as EXPTIME. The minimum useful value for dark, flat, or object images is 0.01 seconds, while zero images have a value of 0 seconds. If EXPTIME > 1 sec., the camera's pre-amplifier is turned off for the exposure, to prevent corner glow in the frame.

It is known that a 10ms delay occurs after opening the camera shutter, but since this is a constant for all exposures, it is not accounted for. However, long exposures (>10

$$\tau = \frac{L \times s - S \times l}{S - L} \quad \text{eq. 3.4}$$

seconds) are timed from the computer clock, and therefore are subject to its accuracy. The user interested in precision photometry is encouraged to measure the actual integration time by measuring the shutter correction (τ). This "extra" integration time varies with position from the field center.

The following method (Massey et al., 1992) details the calculation of τ . Centre a star bright enough to produce a large S/N (>100) in a 1 second exposure, but not overclock in 10-20 seconds. Take a series of eight exposures (1 sec, 20 sec, 20 sec, 1 sec, 1 sec, 20 sec, 20 sec, and 1 sec) during photometric conditions, and perform quick aperture photometry on them with a large aperture radius (3-4 FWHM). The shutter correction is then related to the mean flux S and L (ADU in aperture from short and long exposure times, s and l respectively) by equation 3.4. Enter τ in the Shutter Correction box on the Quick Photometry form (described later in this chapter).

- **IMAGETYP** Determines what type of image is created. Users can choose from zero, dark, flat and object. This entry is written to the FITS header keyword IMAGETYP. Selecting *zero* will automatically set **EXPTIME** to 0 sec., and the integration performed is a simple "flush and read" of the chip. Selecting *dark* will result in a timed integration with the shutter closed. *Flat* and *object* images are made with the shutter open.
- **AutoSave** If AutoSave is checked, the array of data values from chip readout are saved along with all header information, after being displayed. The filename is determined from the **base** and **extension** present in CONFIGURATION, and the format is FITS (Berry, 1995).
- **Begin, Stop** The **Begin** button sets in motion a loop that calls a function called SingleCameraExposure. This function integrates, reads out, auto-calibrates (if selected), calculates the minimum, maximum, mean and RMS standard deviation of the new image, displays, and writes the data array plus header information to a file. The loop repeats N times, where N=NUMBER of images selected, and may include a delay between exposures (if **Delay** \neq 0 in MULTI-EXPOSURES). During an integration or delay, the computer is available for other functions (e.g. performing photometry) but during the several seconds of readout time for each image, it is not.
Stop will discontinue this loop, read out the chip's signal, adjust the exposure time to $I_{adjusted} = I_{original} - ETL$, and display the adjusted image (and save it if **AutoSave** is checked).

MULTI-EXPOSURES

This window gives the user the ability to create, edit, and execute a series of different exposures in different filters.

- **Length, Filter** This list box displays the current exposure queue, listing the length and filters of each integration to be performed. The user can select individual items in this list

for editing or deletion.

- **EXPTIME** The entry in this box is the desired exposure time (in seconds) to go with selected **Filter**.
- **Filter** This button group selects the filter to be entered in the list box alongside **EXPTIME**. Button labels are determined by the **Filter Slide** selection in HEADER INFORMATION.
- **Delay** Indicates the delay time (in seconds) between exposures in a series launched from MULTI-EXPOSURES or SINGLE EXPOSURES.
- **Begin, Stop** The Begin button starts a loop that reads the items in the list box, and loops the function SingleCameraExposure() (described in SINGLE EXPOSURES) with filter changes and exposure times. If AutoSave is checked, each exposure will be saved before filter change is activated. A **Delay** time between exposures is executed if required. **Stop** discontinues this loop, reads out the charge wells, adjusts the exposure time to $I_{adjusted} = I_{original} - ETL$, and displays (and saves) the adjusted image (if **AutoSave** is checked).
- **Add, Delete, Clear** Editing buttons for adding an exposure to the queue, deleting a selected item from the queue, and clearing the list box completely.
- **Loop Entries** If checked, the series of exposures in the queue will be looped by the number in the box.

Multi-Exposures

Length, Filter	EXPTIME	Filter	
120, 1	55	1	Add
90, 2	Delay	2	Delete
60, 3	0	3	Clear
55, 4	Begin	4	<input checked="" type="checkbox"/> Loop Entries
	Stop	5	3

3.5 DESCRIPTION OF MEASUREMENT AND VISUALIZATION FUNCTIONS

DevonCB is equipped with advanced image processing features and a professional grade photometry package to fulfill its primary goal of allowing the astronomer freedom to look at and measure the data as they come from the camera. These features may be operated at the telescope while collecting data. It is thus possible for the user to visually assess the data and perform stellar photometry on calibrated images while acquiring more. Observing time spent efficiently means better data, and the user may take home a single diskette of differential time-series photometry rather than a tape of raw images.

IMAGE VISUALIZATION FUNCTIONS

The processing control window is shown in Figure 3.2, and is organized in three distinct areas, each with functions operating in fundamentally different ways to modify an image.

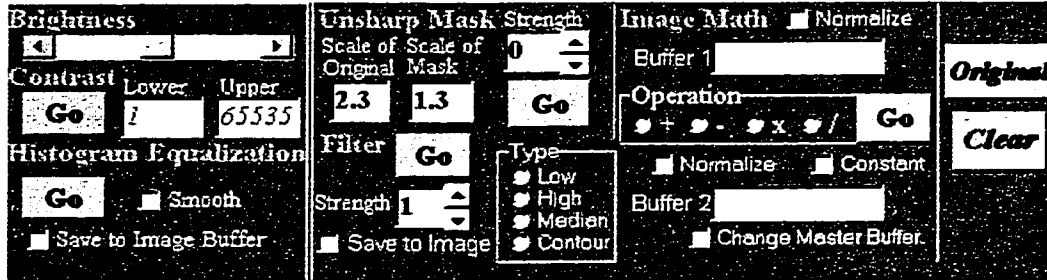


Figure 3.2: The image processing control window of DevonCB.

Functions in the left portion of the processing control window modify the *histogram* (the

$$P(x_i) = \frac{n_i(x_i)}{N}, \quad \sum_i P(x_i) = 1 \quad \text{eq. 3.5}$$

pixel intensity distribution) of an image (equation 3.5). This is a discrete probability distribution of finding the i 'th pixel at intensity x_i . Modifying the histogram redistributes pixel intensities, amplifying or suppressing any value or range of values. Histogram functions in DevonCB are simple.

- **Brightness** A scroll bar that simply adds or subtracts the same counts to every pixel in the histogram, increasing or decreasing the apparent brightness of an image. The ceiling of $2^{16}=65536$ ADU is reached by some pixels before others, and thus the histogram tends to flatten towards the origin, populating further out to high pixel values.

$$x_{i_{new}} = \frac{x_i - x_{<}}{x_{>} - x_{<}} 2^{16}, \quad x_{<} \leq x_i \leq x_{>} \quad \text{eq. 3.6}$$

- **Contrast** This is known as stretching the histogram, and is useful if the bulk of pixels in an image occur at low intensities. The user redefines the boundaries of the histogram by redistributing intensities within a lower $x_{<}$ and upper $x_{>}$ limit. Pixels with $x_i < x_{<}$ assigned a value of $2^0=1$, and $x_i > x_{>}$ assigned a value of 2^{16} . The remainder are assigned intensities proportional to their original values, determined by equation 3.6. The result is that faint objects lost in the sky background are amplified while the heavy population of background values is outside the histogram, and thus assigned $x_i=1$.
- **Histogram Equalization** or histogram leveling is a way of redistributing the histogram such that every intensity level has roughly the same probability of existing. This populates the higher intensity pixels, which has the effect of disproportionately amplifying pixels belonging to minority groups. One first constructs a lookup table (equation 3.7). This table is then normalized (equation 3.8):

$$y_i(x_i) = \sum_{j=0}^i P(x_j) \quad \text{eq. 3.7}$$

$$y_i = 2^{16} \frac{y_i(x_i)}{\sum_i y_i(x_i)} \quad \text{eq. 3.8}$$

Each intensity in the image is transformed as $x_i = w_i(x_j)$. This “spreads out” the intensities, sharing them roughly equally between the sky and object.

Illustrations of histogram stretching and equalization are presented in Figure 3. Each tool, by default, does not modify the master pixel map: only what is displayed, unless **Save to Image Buffer** is checked. This is useful if one wishes to add another step to the processing, such as a **Filter**.

In the **middle** portion of the processing control window are more specialized functions called *filters*. A filter interpolates a pixel’s value by evaluating surrounding pixels, located under a *mask*. Filters work by modifying the spatial frequencies in an image, not just the amplitudes of those pixels. They emphasize image details on a coarse or fine scale. DevonCB includes an assortment of filters.

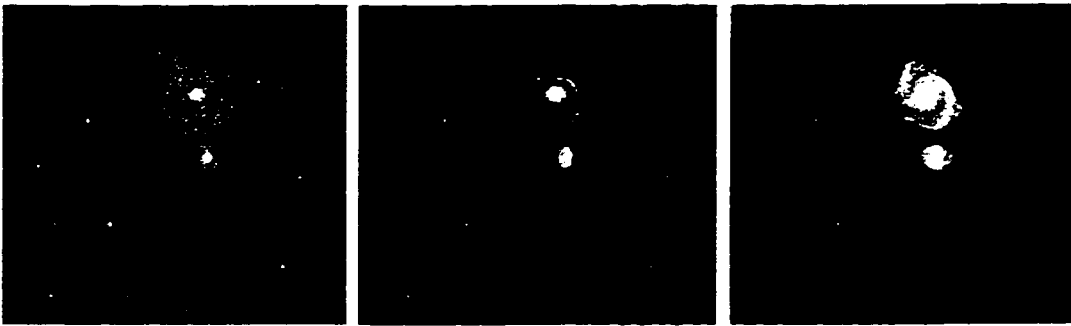


Figure 3.3: On the left, the original image of M51 obtained through the sky glow of Edmonton, Alberta. Histogram stretching (middle image) enhances the contrast of M51, while histogram equalization (right) strongly emphasizes the galaxy.

- **Low, High Pass** The low pass filter emphasizes low spatial frequencies (or low resolution features) while removing the high frequencies (or fine detail) in an image. The

$$x_i = \frac{\sum_{j=1}^i n_j x_j}{\sum_j n_j} \quad \text{eq. 3.9}$$

high pass filter does the opposite. Both filters work by first forming a *convolution matrix* and centering it on the pixel of interest. That pixel’s value is then reassigned as a weighted average of all matrix elements (equation 3.9), where n_j is the coefficient of the convolution matrix’s j ’th element. The image is then *convolved* (multiplied in the Fourier Transform domain of spatial frequencies) or “swept” by this matrix. Different values for these elements determine the type (high, low pass) and strength of the convolution. An illustration of how powerful filtering is when combined with histogram functions is provided in Figure 3.4.

- **Median, Erode and Expand** These non-linear filters can selectively remove noise, while leaving real structure relatively untouched. The median, statistically, is insensitive to strongly deviant points in a distribution. Thus, a median filter will tend to remove noise from a distribution of pixels (x_j). A convolution matrix with $n_j=1$ is swept over the image, and the central pixel’s value is determined by the median score, or central value of the sorted (lowest to highest value) distribution.

A stronger version of the median is called the **Erode** filter. This filter has the unique property of removing stars from an image, while leaving larger structure intact.

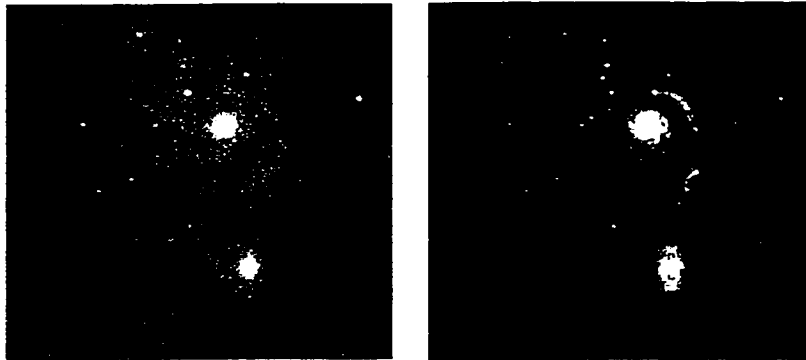


Figure 3.4: The raw image (left) is first processed with a strong high pass filter to accentuate detail in the spiral arms. The image was then weakly low pass filtered to remove noise. Finally, the image histogram was stretched to produce the fine detailed view of M51 (right).

Instead of replacing the central pixel's intensity with the median, we replace it with one of the lesser values to the left of the median. Or, oppositely, we can **Expand** the image by replacing the central pixel's intensity with greater values to the right of the median.

A fine example of the power of these filters, together with modifying the histogram, is seen in Figure 3.5. The tendrils of the Crab supernova remnant, invisible in the original image, are brought into prominence by the combined action of erosion, high pass filtering, histogram stretching, and two weak low pass filters.

- **Contour** To very strongly emphasize detail, the contour (or gradient) filter can be applied. This is a convolution matrix with negative coefficients in its upper left, and identical, but positive ones in the bottom right. The diagonal is given zero weight (matrix elements $n_j=0$). Sometimes called directional filtering, it can greatly enhance invisible spiral structure in a faint galaxy. This is more of an inspection tool, since the strength of this filter often leaves the image with an unrealistic, shadowed 3D effect.
- **Unsharp Mask** A specialized application of the low pass filter to make a very powerful high pass filter, with spectacular results when applied to images of solar system objects. Fine details on the moon stand out clearly with an application of this technique (see Figure 3.6). One creates an “unsharp” version of the original image (via a low pass filter) where only low spatial frequencies are left. Subtracting this from the original (containing both high and low spatial frequencies) leaves an image with more high than low spatial frequencies. Low contrast zones now stand out in high relief. A higher spatial frequency cutoff in the original low pass filter will leave a higher proportion of fine details, although one can easily overdo this powerful filter. Leave some low frequencies in for a look of realism.

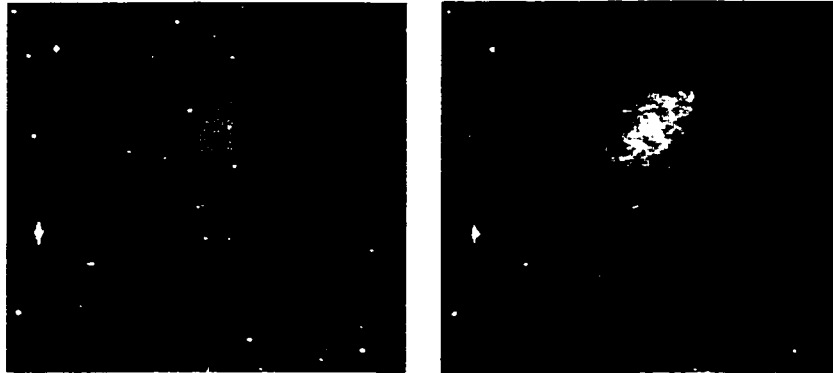


Figure 3.5: An image of the Crab nebula (at left) is enhanced by the series of an erosion, high pass, and two weak low pass filters, along with a contrast boost from histogram stretching. Note the prominence of the filaments in the filtered image.

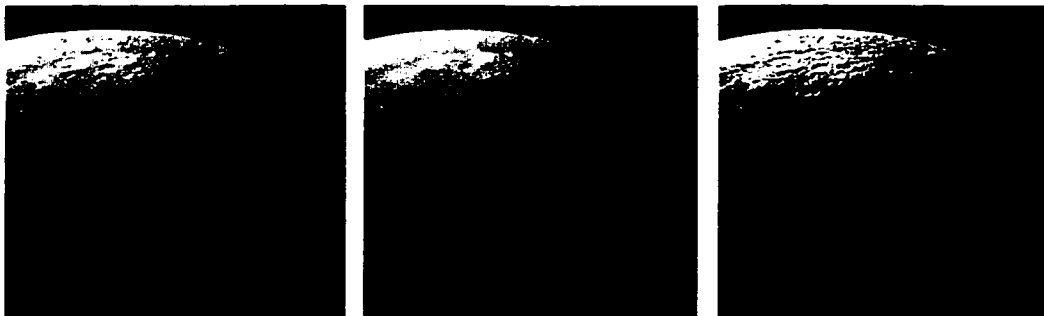


Figure 3.6: A portion of a DevonAO image in original form (left), masked (middle) and the result of subtracting this from the original (right). Details in the lunar highlands become apparent.

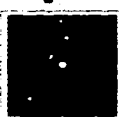
Checking the box **Save to Image** in the **Filters** control area will write any changes to the master buffer.

The **rightmost** portion of the control window provides the user with *arithmetic* image processing functions. These furnish the ability to modify an image by addition, subtraction, multiplication and division by both constants and other images. These operations differ from filters and histogram manipulation, in that two or more images can determine the output image. Image correction can also be done here (overscan, zero and dark subtraction, flat field division, and deferred charge map addition). The **Buffer** text boxes present the user with a load dialog when clicked. An image can be loaded, or, by canceling, a constant can be entered (ensure the **Constant** box is checked). Entering **Buffer 2** is not permitted until **Buffer 1** is filled, and both buffers must contain images of the same pixel dimension. Checking **Normalize** will divide a buffer by its own mean value before any other operation. An **Operation** (addition, subtraction, multiplication and division are possible) is selected, and carried out by the **Go** button. The results can be saved to the master pixel map for further work.

An important feature of any image manipulation routine used with astronomical data is that it *does not alter the real data in any way*, unless the user wishes. Image processing functions in DevonCB display and store processed data in buffers entirely separate from the master pixel map. If one does wish to save their processing efforts, one can do so in both FITS and graphical (bitmap) formats from the **File** menu. However, the original FITS image always remains in memory: if a mistake has been made, the user can return to the original data.

The **Original** button at the far right will undo *all* processing and return the master pixel map to the display, even after saving a modified version of that image. **Clear** resets all pixel maps in memory and displayed, but will first confirm this operation and offer the user the chance to save any modifications.

IMAGE MEASUREMENT FUNCTIONS

<input checked="" type="checkbox"/> Star Image Centroiding	Instrumental Magnitude	Nsky	Nrej	Target Star 
Centering Box Width	m 11.6542	525	31	
Aperture Radius (Pixels)	Photometric Error	Sky Value (ADU/Pixel)	Osby	Warning!! Star Overclocked
Width of Inner Sky Box	δm 0.0012 Dominated by Sky noise	1912.9311 ± 33.05		
Width of Outer Sky Box	X Center of Image	Area of Aperture (pixels ²)		Previous Measurements
Instrumental Z Point	326.381	314.74035		
Shutter Correction	Y Center of Image	Flux (ADU Pixels ⁻²)		(263.085, 277.856) = 13.5842
Filter	433.417	520550.87		(326.382, 433.417) = 11.6542 OC
FWHM	Time	UT at Mid. Exposure		
Filename	600	03:12:58		
Output to File	Airmass			
Ok	Ha+NII			
	Clear Values			
	1.0010725			
	FWHM			
	2.13997			

Enter parameters under blue headings!

Figure 3.7: The Quick Photometry Window of DevonCB, performing aperture measurements on stars in a field near NRAO 655.

Built into DevonCB are powerful image measurement tools that perform stellar image centering and aperture photometry. These allow stellar positions and instrumental magnitudes to be extracted in real time. Onsite light curve construction and analysis is then possible. Photometry options in DevonCB are similar to those in IRAF (Davis, 1999), but the DevonCB package is currently useful only for uncrowded fields. Refer to Figure 3.7 for presentation of the quick photometry control window.

To activate the photometry package, check the menu item **Image Measurement**→**Quick Photometry**. This brings up the photometry window initially, allowing one to set the options below.

- **Star Image Centroiding** When checked, the centre of the stellar image of interest is determined, and the photometry aperture is centred on these coordinates. The method of *image centroiding* (or moment analysis) is implemented here (described by

$$\rho(x_i) = \sum_{j=-a}^a I_{ij}, \quad \rho(y_j) = \sum_{i=-a}^a I_{ij} \quad \text{eq. 3.10}$$

DaCosta, 1992). The equations work on the premise that the star's true centre lies within the brightest pixel, and find the intensity equivalent of the star's "centre of mass". The equations begin by placing a square box of side length $2a$ on an initial guess of the star's centre (x_0, y_0) as determined by the cursor position when clicked. Parameter a is the **Centering Box Width**. *Marginal sums*, defined by equation 3.10, are computed by summing pixel intensities I_{ij} down the columns ($\rho(x_i)$) and across the rows ($\rho(y_j)$). Mean values of each set of marginal in x and y are calculated (X, Y), and a new image centre (x_1, y_1) is determined by a weighted average of $\rho(x_i) - X$ and $\rho(y_j) - Y$, as in equation 3.11. This new centre becomes the new guess and the algorithm is iterated, until (x_1, y_1) lie within one pixel of (x_0, y_0) . The final centre is recorded in **X Center** and **Y Center** boxes on the photometry form. Reasonable accuracy (< 0.1 pixel) is achieved with this method, but for rigorous astrometric analysis, a preferred method is Gaussian fits to each marginal.

$$x_1 = \frac{\sum_{i=-a}^a (\rho(x_i) - X)x_i}{\sum_{i=-a}^a (\rho(x_i) - X)}, \quad \rho(x_i) \geq X$$

$$y_1 = \frac{\sum_{j=-a}^a (\rho(y_j) - Y)y_j}{\sum_{j=-a}^a (\rho(y_j) - Y)}, \quad \rho(y_j) \geq Y \quad \text{eq. 3.11}$$

Aperture Radius The radius of the circular aperture placed on the star's true centre. To contain "all the light" from the star, the aperture radius should be at least $3 \times \text{FWHM}$ (from a Gaussian fit to the stellar profile), but depends largely on the brightness of the star. Fainter stars call for *smaller* apertures, since large ones contain significant sky noise, the errors of which can dominate a faint star's signal.

Aperture photometry is accomplished by summing pixel intensities inside the aperture after subtracting a mean sky background. The star's brightness is expressed

$$m = Z_{pt} - 2.5 \log \left(\sum I_{ij} - n_{pix} I_{sky} \right) - 2.5 \log(I_{time}) \quad \text{eq. 3.12}$$

(equation 3.12) as an **Instrumental Magnitude**, where I_{sky} = modal background value per pixel, n_{pix} = number of pixels contained in the aperture, Z_{pt} = arbitrary **Instrumental Zero Point** magnitude, and I_{time} = true integration time (I_{time} = requested exposure time - **Shutter Correction** τ).

Since the aperture is a circle, placing it on a rectangular grid of pixels will necessitate the inclusion of *partial pixels* in the term n_{pix} . To include light from these pixels, a method similar to DAOPHOT (Stetson, 1987) is employed, whereby the pixel intensity is linearly weighted according to the fractional portion of that pixel located inside the aperture.

- **Width of Inner/Outer Sky Box** To properly determine the background flux the star sits atop of, one forms a *sky annulus* around the star. The annulus must be far enough from the star's centre, as not to include pixels for which flux from the star has been recorded. Some measure of the central tendency of pixel intensities within the annulus is then taken to be I_{sky} . DevonCB does not use the pixels within a true annulus, but rather those in a region between two square boxes of different widths (**Inner, Outer**), centred on the star. In this way, the bias created by using pixels all at a constant radius from the star's core is avoided, and the need for a partial pixel scheme is gone. DevonCB computes I_{sky} as the *mode* ($\approx 3 \times \text{median} - 2 \times \text{mean}$) of the distribution of these pixels. This calculation is iterated by trimming pixels $> 3\sigma$ away from the mode (**Nrej**), until the value of I_{sky} has settled. The result and the rms standard deviation of the trimmed distribution are recorded in **Sky Value** $\pm \sigma_{sky}$. This algorithm is relatively insensitive to stars that may lie between the sky boxes. The widths of these boxes should be large enough to include many sky pixels (**Nsky**), for a good representation of the sky, but not so large that bright nearby stars contaminate the pixel intensities within.
- **Output to File, Filename** When the **Output to File** box is checked, one can enter a **Filename** to which to write all measurements. This is a plain ASCII text file consisting of nine columns, ordered by these headers:
Filename, X Center, Y Center, Itime, Filters, UT, AIRMASS, m, δm
This file can be imported into a spreadsheet or plotting program for light curve construction and analysis. These parameters are set when the **OK** button is pressed, and the window closes. The user then selects a star in the main image. The window opens upon clicking the stellar image and displays results (if entered, the measurement is written into the file **Filename**). The window re-appears for each click of the image, and subsequent measurements are appended to **Filename**.
- **Photometric Error (δm)** A function of instrumental limitations (camera *gain* and readout noise r_e), as well as Poisson statistics (n_{pix} , I_{sky} , I_{star}) (Newberry, 1999). The function is given by equation 3.13.

$$\delta m = \frac{1.0857}{I_{star} \times gain} \sqrt{I_{star} \times gain + n_{pix} (r_e^2 + I_{sky} \times gain)}$$

eq. 3.13

Notice that large apertures (large n_{pix}) contribute to reducing the precision of the measurement of m , as does a bright background (I_{sky}). For low readout noise CCD's, the readnoise term ($n_{pix} \times r_e^2$) is usually dominated by sky noise ($n_{pix} I_{sky} \times gain$).

This is recorded beside the box for δm .

We can glean important information about the precision of our measurements from the above equation. Bright stars have dominant Poisson noise terms ($I_{star} \times gain$), and larger apertures should be used, to include more light from the star. Fainter stars against bright backgrounds should be measured through tighter apertures, and an aperture correction applied (see DaCosta, 1992).

- **Area of Aperture, Flux** The area contained within the photometric aperture (in square pixels) and the measured stellar flux through that aperture (in $\text{ADU} \times \text{pixels}^2$).
- **UT at Mid. Exposure, Airmass** Greenwich mean time, and the airmass at the field centre, calculated at the time of mid-exposure.
- **Target Star** A magnified portion of the stellar image and surroundings. The photometric aperture (red), and the sky boxes (grey) are drawn, centered on (**Xcenter, Ycenter**). This

allows one to visually gauge the centering accuracy and the aperture size. If the centered star contains saturated pixels, a warning appears beneath this box.

- **Previous Measurements** Displays all previous measurements made while the photometry option was active. An “OC” indicates an over-clocked star image. One may clear the entries in this list box by pressing **Clear Values**.

3.6 DESCRIPTION OF CUSTOMIZABLE FEATURES

As DevonCB software evolves to function with different CCD cameras, a more widespread community of observatories may use it. Thus, some configurable features were needed to assist new users of the program. The program has the flexibility to function at different locations with different observing systems, and the following portion of the guide describes this functionality.

FITS HEADER EDITOR

To completely customize each image from a data series, a text header is included with each saved file. The FITS format permits 2880 bytes of ASCII information to be written before the binary data stream, and it is used for image-critical record entries. DevonCB writes a very comprehensive FITS header, inclusive of all astronomical information that describes the observing. For custom entries, or to change header errors, DevonCB includes a FITS header editor, the screen of which is presented in Figure 3.8.

- **File Name** This box displays the name of the FITS file being edited, and the full directory path to the displayed file.
- **Keywords, Values** The **Keywords** box lists the current set of keywords DevonCB is built to output to saved images. The list represents the most descriptive elements of an astronomical FITS image. Most of these are described in the text of this guide. For more detailed keyword descriptions, refer to Berry 1995, and Kay et al. 1995. **Values** for these **Keywords** are all derived from relevant parts of the program, and are all written from program settings prior to saving the data array. Important time keywords (GMT, JD, MST) are recorded immediately after the shutter closes on an exposure.
- **Update Data** Clicking a header entry in the **Keywords** list box will offer the user a chance to change it. The keyword appears alongside its **Value** in the boxes next to the **Update Data** button. After changing the text in the value box, pressing this button writes the change to the header stored in memory. Upon saving the file, the header is written with this new information.

OBSERVATORY PARAMETERS

This window allows entry of the name and geographical location of the observatory using the program, and is opened from the **Setup→Observatory** menu item. This configures DevonCB for calculation of the proper local standards, such as mean sidereal time and object airmass. At the very least, the user can enter different locations in this window, and use the output as a handy calculator of these values. The window layout is illustrated in Figure 3.9.

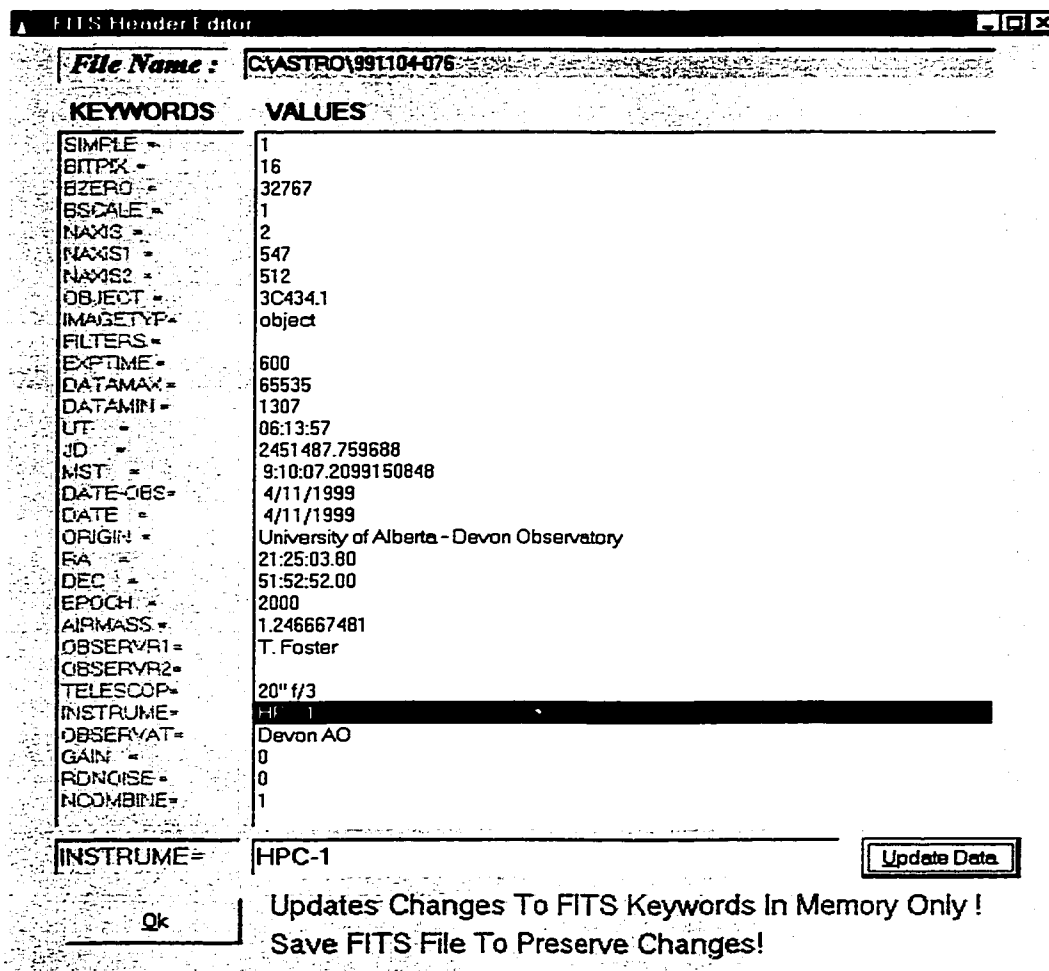


Figure 3.8: The FITS header editor window, changing the INSTRUME keyword in an image of supernova remnant 3C434.1.

- **Name** For file records, the name of your observatory can be entered, and will appear in the FITS header under the keyword OBSERVAT.
- **Latitude** The latitude of the working observatory. Positive for Northern Hemisphere locations. This must be entered in decimal degrees.
- **Longitude** The longitude (positive west) of the working observatory. This must be entered in decimal degrees.
- **Altitude** The altitude above sea level (in meters) of the working observatory.
- **Save** When pressed, this button appends the current entry to the observatory database file "obsdb.txt". This observatory entry is then available for the next observing session as a call up, rather than having to be entered again.

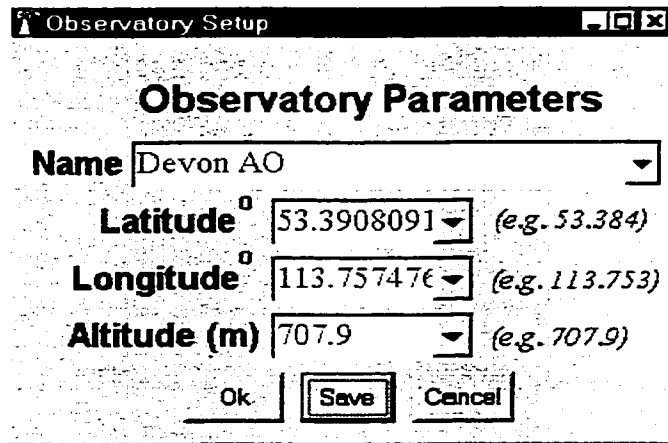


Figure 3.9: The Observatory Setup window.

COMM SETTINGS

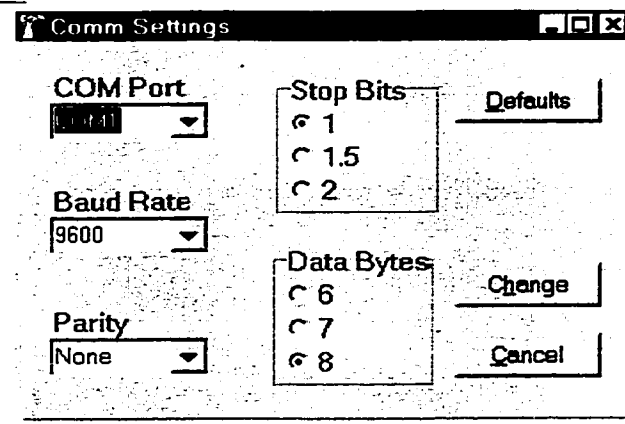


Figure 3.10: The COMM Settings window configured to use COM1.

Maximum compatibility is offered to observatories with motor driven camera focus, rotation and filter changes, in the form of communications. DevonCB can send to and receive data from PC COMM Ports, to read position encoders and control camera motions. This capacity makes developing communications code easy for any observatory that wishes the program to control hardware. For flexibility, DevonCB uses one of four typical ports in use in PC's. The **COMM Settings** window configures the use of this port, and is shown in Figure 3.10. The defaults are typical of most port settings. To hook your custom control code that uses COM1-COM4 into DevonCB, contact the author.

3.7 THE FUTURE OF DEVONCB

DevonCB was built as a professional tool for gathering high quality CCD data. As it currently stands, it easily competes with most CCD Control Software packages available

today. It is hoped that this chapter has described DevonCB well enough to inspire reader input to the program's future. DevonCB should not reflect the ideals of one astronomer, but many in the professional and amateur community. The immediate future for Cookbook CCD camera owners is promising, as this is the next planned camera to be controlled. It is hoped that DevonCB's ability to obtain and analyze astronomical time series data will stimulate the Cookbook CCD astronomer's participation in amateur-professional collaborations, such as the Center for Backyard Astrophysics.

3.8 REFERENCES

Berry, R. *FITS: File Format for the Astronomical World*. CCD Astronomy, Vol. 2, No. 4, 1995.

Buil, Christian. *CCD Astronomy*. Willmann Bell, Inc., Richmond VA, 1991.

Davis, L. E. *Stellar Photometry Tools in IRAF*. From the *CCD Precision Photometry Workshop*, ASP Conference Series (E. Craine, R. Tucker and J. Barnes, editors), Vol. 189, 1999, 35.

DaCosta, G.S. *Basic Photometry Techniques*. From *Astronomical CCD Observing and Reduction Techniques*, ASP Conference Series (Steve B. Howell, editor), Vol. 23, 1992, 90.

Foster, T. et. al. *A High Performance CCD System for Detection of Optical Supernova Remnants*. From the *CCD Precision Photometry Workshop*, ASP Conference Series (E. Craine, R. Tucker and J. Barnes, editors), Vol. 189, 1999, 50.

Gilliland, R. L. *Details of Noise Sources and Reduction Processes*. From *Astronomical CCD Observing and Reduction Techniques*, ASP Conference Series (Steve B. Howell, editor), Vol. 23, 1992, 68.

Gilliland, R. L. and Brown, T. M. *Time-Resolved CCD Photometry of an Ensemble of Stars*. PASP, 100, 1988, 754.

Gullixson, C.A. *Two Dimensional Imagery*. From *Astronomical CCD Observing and Reduction Techniques*, ASP Conference Series (Steve B. Howell, editor), Vol. 23, 1992, 130.

Kay, D. C. and Levine, J.R. *Graphics File Formats (2nd Edition)*. Windcrest/McGraw Hill, New York, 1995.

Massey, P., and Jacoby, G. H. *CCD Data: The Good, the Bad, and the Ugly*. From *Astronomical CCD Observing and Reduction Techniques*, ASP Conference Series (Steve B. Howell, editor), Vol. 23, 1992, 240.

Meeus, Jean. *Astronomical Formulae for Calculators, 2nd Edition*. Willmann Bell, Inc., Richmond VA, 1982.

Mighell, K.J. *CCD Aperture Photometry*. From the *CCD Precision Photometry Workshop*, ASP Conference Series (E. Craine, R. Tucker and J. Barnes, editors), Vol. 189, 1999, 50.

Newberry, M. *Increasing Precision and Accuracy in Photometric Measurements*. From the *CCD Precision Photometry Workshop*, ASP Conference Series (E. Craine, R. Tucker and J. Barnes, editors), Vol. 189, 1999, 50.

Stetson, P. B. *DAOPHOT: A Computer Program for Crowded-Field Stellar Photometry*. PASP, 99, 1987, 191.

Tyson, J.A., and Seitzer, P. *A Deep CCD Survey of 12 High-Latitude Fields*. Ap.J., 335, 1988, 552.

Chapter 4

RADIO AND OPTICAL OBSERVATIONS OF OBJECTS IN THE CGPS FIELD J8

4.1 SUMMARY

Comprehensive analysis of the CGPS J8 field (centered near galactic coordinates $l = 94^\circ, b = 1^\circ$) calls for data at multiple wavelengths. This project required much astronomical observing to be undertaken by the author, using different telescopes in different windows of the electromagnetic spectrum. Further time is required for processing and calibration of these observations. Data at other wavelengths from databases of past observations must also be acquired and processed for comparison. Observations and data processing were done by the author at radio continuum wavelengths ($\lambda = 21\text{cm}$, $\lambda = 74\text{cm}$), atomic and ionized hydrogen lines ($\text{HI} = 21.106\text{cm}$, $\text{H}166\alpha = 21.042\text{cm}$ and $\text{H}158\alpha = 18.152\text{cm}$) and optical emission lines ($\lambda_{\text{OIII}} = 502\text{nm}$, $\lambda_{\text{H}\alpha} = 656\text{nm}$, $\lambda_{\text{SII}} = 672\text{nm}$). Details of these observational data, such as origin in astronomical sources and observatories are presented in Table 4.1. Astronomical sources, and data origins are discussed here in detail. Steps in processing these data are thoroughly treated throughout this chapter and the accompanying appendix to this thesis (Appendix A). The final processed images and spectra are presented, and data artifacts are discussed at length, as are details of the calibration the optical emission line data.

4.2 THE DRAO SYNTHESIS TELESCOPE (DRAO ST)

Objects were observed at $\lambda = 21\text{cm}$ and $\lambda = 74\text{cm}$ with the Synthesis Telescope (see Table 4.2) at the Dominion Radio Astrophysical Observatory, and are within the telescope's $2^\circ.5$ field (at 21cm). These continuum observations were carried out in April, 1998, as part of the Canadian Galactic Plane Survey's J8 field in northern Cygnus. Observational details are presented in Table

λ	Bandpass	Origin	Astronomical Source
21 cm	broad 0.446 cm	DRAO ST	HII, synchrotron emission
21.106 cm	line 0.15 mm	DRAO ST	Atomic HI
21.042 cm	line 0.6 mm	DRAO 26m	H166 α recombination
18.153 cm	line 0.44 mm	DRAO 26m	H158 α recombination
74 cm	broad 0.63 cm	DRAO ST	HII, synchrotron emission
502 nm	line 5.4 nm	Devon AO	Ionized gas -[OIII]
656 nm	line 7.5 nm	Devon AO	Ionized gas - H α + [NII]
672 nm	line 5.0 nm	Devon AO	Ionized gas -[SII]

Table 4.1: Details of astronomical data observed and processed by the author.

ST Feature	Value (1420 MHz)	Value (408 MHz)
Maximum Baseline	617.2m	-
Minimum Baseline	12.9m	-
Baseline Increment	4.3m	-
Angular Resolution	1' x 1' cosec δ	3'.4 x 3'.4 cosec δ
RMS Noise T_b (K), map centre	0.049 sin δ K	0.670 sin δ K
Field of View	2.6 $^\circ$ to 20%	8.1 $^\circ$ to 20%
Spectrometer	1420 MHz	
Available Bandwidths	0.125, 0.25, 0.5, 1.0, 2.0, 4.0 MHz over 256 Channels	
Velocity Coverage	211 $km s^{-1}$ x Spectrometer BW	
Channel Width	1.32 $km s^{-1}$ x Spectrometer BW	
Channel Separation	0.824 $km s^{-1}$ x Spectrometer BW	

Table 4.2: Details of the DRAO Synthesis Telescope .

4.3. The J8 field centre is at $\alpha(2000) = 21^h 22^m 36.7^s$, $\delta(2000) = 51^\circ 30' 33''$. As part of this survey, 256 velocity channels (width 1.32 km/s, separated by 0.824 km/s) of HI line observations along the line of sight were obtained for the field. The DRAO synthesis telescope is an array of seven 9m diameter telescopes, distributed along a 600m EW baseline. Working at 1420MHz, it achieves an angular resolution of 1' x 1' cosec δ , with a beam 107.6' at FWHM, and can observe total intensity (I), linear polarizations (Q and U), as well as circular polarization (V), i.e. all four Stokes parameters. At 408 MHz, a single left hand circular polarization is observed. Resolution decreases to 3'.4 x 3'.4 cosec δ over a field 8 $^\circ$ wide. A fully sampled uv plane for both frequencies results from several 12 hour observations at various antenna spacings from 12.9m to 604.3m . While other surveys supplement DRAO ST images with the broad structure missed by the lack of antenna spacings lower than 12.9m, lower order spacings for ST HI spectral line images are made by the DRAO 26m paraboloid.

HI line images were received with these short-spacings added, and needed minimal post processing. However, the continuum images were received by the author as raw ST telescope data, and were processed in the following order.

J8 Field Parameters	1420 MHz	408 MHz	HI Line
Epoch of Observation	1998.35	1998.35	1998.35
$\nu_{central}$	1420.6108 MHz	408 MHz	1420.406 MHz
Bandwidth	30.0 MHz	3.5 MHz	1.0 MHz
AGC Correction Factor	-	1.235	-
Resolution	1' 13" x 0' 58"	4' 12" x 3' 24"	1' 13" x 0' 58"
Central Velocity	-	-	60.000 $km s^{-1}$
Stokes Parameters	I,Q,U,V	I	I
Spectrometer	1420 MHz		
Velocity Coverage	211 $km s^{-1}$		
Channel Width	1.32 $km s^{-1}$		
Velocity Channel Separation	0.824 $km s^{-1}$		

Table 4.3: CGPS J8 Field Observational Parameters.

Polar-diagram correction was applied to even the gain across the field, which varied due to the shape of the primary beam. A cosine power of order 6 is measured to fit the primary beam shape the most satisfactorily. This step was applied to both continuum and HI line data, as well as to polarization data.

Polarization data from the DRAO ST require an extra correction to be applied, to account for the addition of instrumental polarization to the images. This addition is some fraction of the total intensity map (Stokes I), and has been well-mapped over the whole synthesized beam (at 21cm) in 15' increments. Stokes V,Q,and U maps were instrumentally corrected.

The uv plane visibilities are symmetric in amplitude. A point (u,v) on one half of the plane has a corresponding point (-u,-v) 180° away. This can be seen from the symmetry of the grating rings around a bright source. The visibilities, however, are anti-symmetric in phase: the source is observed over only half of the full uv ellipse, the other half of the visibilities being determined by the complex conjugate of the observed ones. Thus, errors in amplitude manifest themselves symmetrically around strong, small-diameter sources, and phase errors, anti-symmetrically. Continuum ST images are systematically contaminated with these two errors. In addition, some uv plane data are missing (e.g. incomplete hour-angle coverage and interference removal by editing), so further processing is needed.

Continuum images were thus processed with the CLEAN algorithm, removing the symmetric sidelobe responses first from around small-diameter sources (Clark, 1980) and then from broader features (Steer, 1984). This algorithm iteratively deconvolves the ST map with a gaussian determined from a "dirty" beam map of the same dimensions, down to a user specified level. It also restores some of the flux lost from an object to its sidelobe responses, back to the original source.

Both symmetric and antisymmetric rings around strong sources are often left over after CLEANing, indicative of amplitude and phase errors, respectively, in uv visibility data. These errors reposition flux from sources around the image.

If, for example, phase errors are instrumental (such as time variations in antenna gain) and hence systematic, this flux will appear consistently in such artifacts as the anti-symmetric rings. Removal of such rings and flux restoration to sources involves the processing technique known as Self-Calibration. One models the visibility data (the Fourier transform of the brightness distribution) of an ST observation from the observation itself, and uses this model to extract systematic errors. This proceeds iteratively on continuum images. An initially CLEANed image is transformed into uv space. Model visibility data are computed, using CLEAN components of the “dirty” image’s brightness distribution, but only those parts free from errors. One writes a new self-calibrated visibility set, and switches back to real space for examination of the results. Self calibrated continuum maps showed improvement, with considerably weaker anti-symmetric rings around small-diameter sources.

Large, diffuse structures (greater than 20' in extent) present in the galactic plane fields observed by the DRAO ST are not visible, since antenna spacings less than 12.9 m are missed. Fortunately, low resolution surveys at similar wavelengths exist for these fields. Kallas and Reich (1980) surveyed the Milky Way over longitudes 355° to 162° ($l = -4^\circ$ to $+4^\circ$) at 21cm with the 100m telescope near Bonn, Germany, with a 8.4' beam. The all-sky survey by Haslam (1982) provides 0.85° resolution data from which short-spacing information can be derived and added to DRAO 74cm ST observations. In both wavelengths, continuum images from these surveys were transformed to the uv plane, scaled, and filtered to remove any redundant spatial frequencies already present in the DRAO ST images. The DRAO ST images themselves were filtered to remove any undesired overlap with the single antenna data, and the two were added together such that a smooth transition through the overlap in spatial frequencies was achieved.

Finally, galactic plane survey observations made at 74cm with the ST require a correction factor to restore the proper flux density to maps. The receiver output is controlled by an AGC system, which reduces the gain between the calibration and observation if the field being observed contains a large amount of flux. Thus, 74cm maps contain a fraction of the true observed flux, which can be restored by deriving a constant correction factor and applying it to the map. This is derived from observations taken from the Haslam survey, using calibration sources 3C147 and 3C295. The 74cm map is then multiplied by our derived AGC factor (1.235) to correct its flux density scale.

For particulars on reductions of the Galactic Plane Survey J8 field, please see Appendix A entitled PROCESSING OF 21CM AND 74 CM DRAO ST CONTINUUM IMAGES. Figures 4.1 and 4.2 display the central portion of the J8 field at 21cm and 74 cm respectively, centred on the objects of interest. NRAO 655 is the western nebula in the fields.

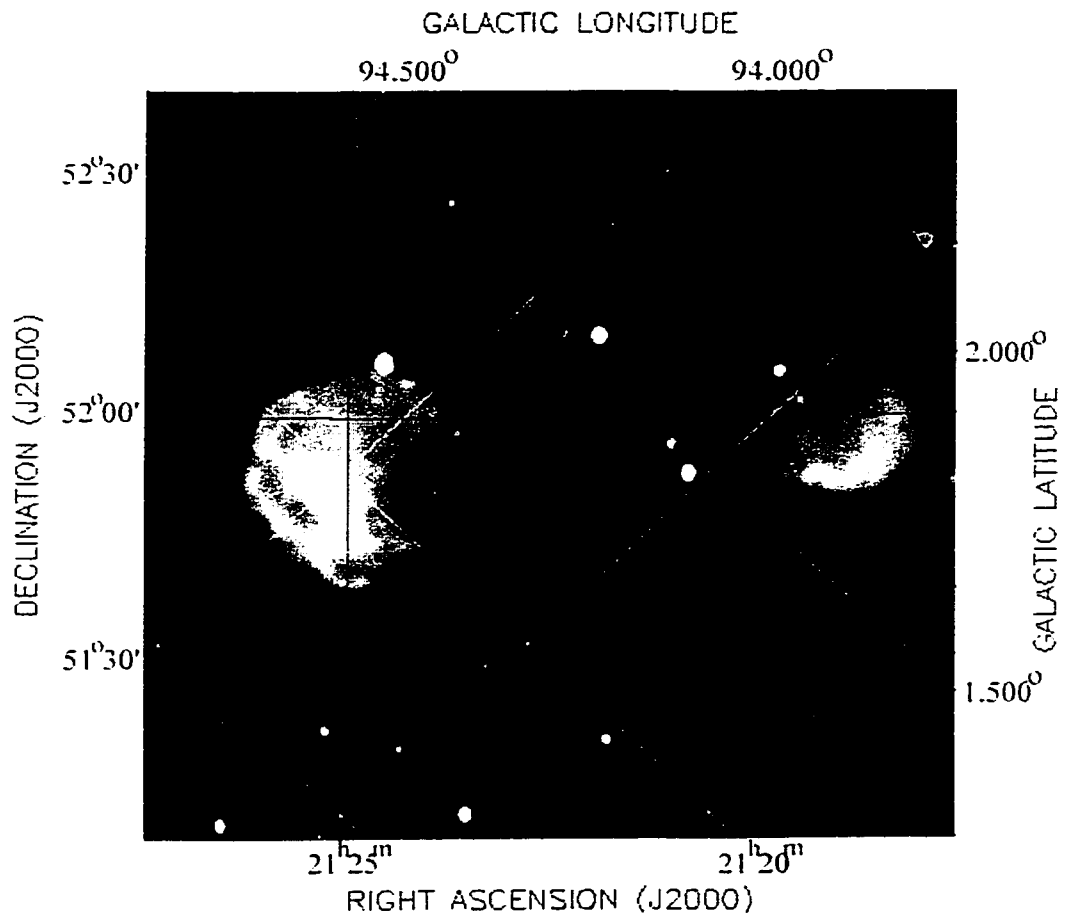


Figure 4.1: Central $2.5^\circ \times 2.5^\circ$ of the 21cm DRAO ST map in CGPS J8 field.

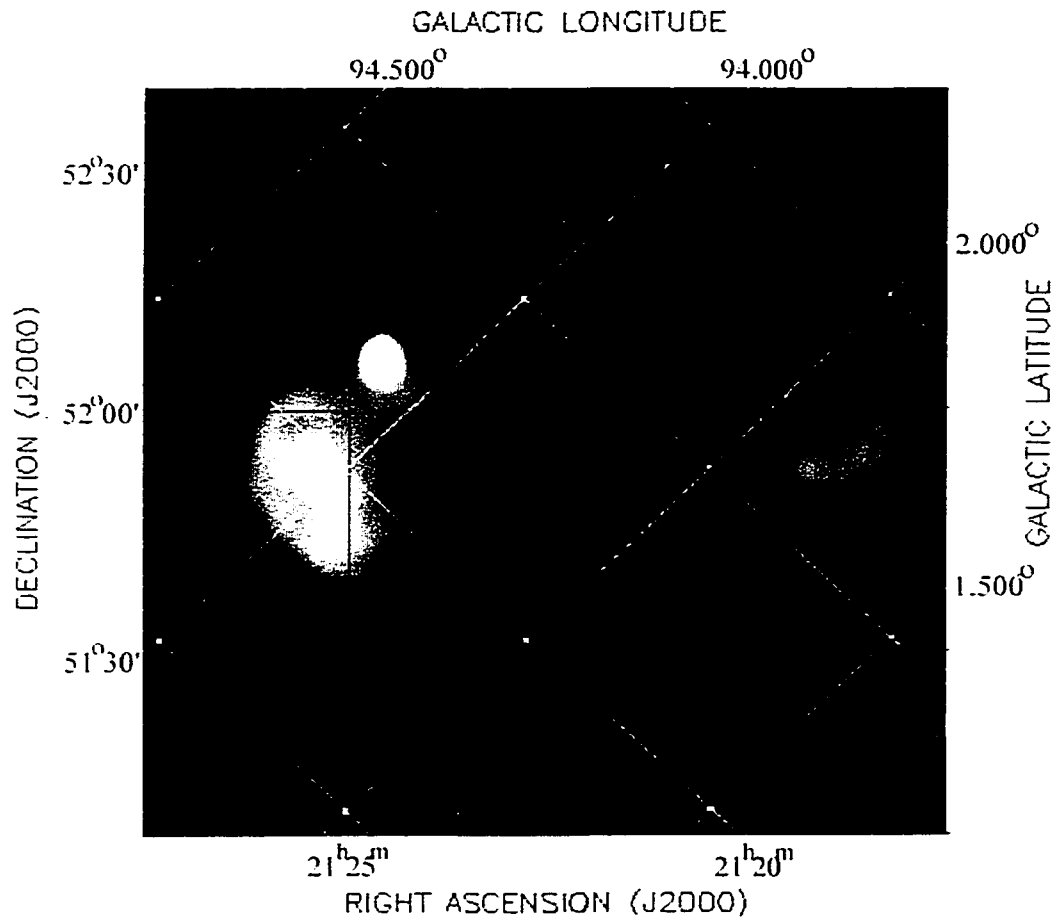


Figure 4.2: Central 2.5° × 2.5° of the 74cm DRAO ST map in CGPS J8 field .

4.3 THE DRAO 26M TELESCOPE

To positively identify NRAO655 and G93.6+1.3 as HII regions, and to conclusively determine their distances, it was decided that these objects should be observed with the DRAO's 25.6m paraboloid, in search of hydrogen recombination line emission.

Such emission is expected in ionized hydrogen clouds, where equilibrium exists, and free electron-proton recombinations balance the ionizations by photons ($\lambda < 91.2$ nm) from young, luminous stars embedded within the cloud. The resulting excited atoms settle to a ground state as the newly bound electrons cascade down the quantum levels. For single quantum number transitions from $n+1$ to n , the radiation is strongest, and the emission is termed α -line emission. When $n > 60$, a radio photon of $\lambda > 1cm$ is produced, and, although the resulting spectral signature is weak, it is observable.

The DRAO 25.6 m antenna is used primarily with the 1.4 GHz broadband receiver installed at the prime focus, for HI line observations at $\nu = 1420.406$ MHz at a beamwidth of $36'$ (to augment those from the ST with short spacing information). The receiver can operate up to 1.7 GHz, inclusive of several prominent recombination lines. The open mesh surface of the antenna allows an aperture efficiency range of 55% to 52% for operating frequencies of 1.4 GHz - 1.7 GHz, respectively. Each of two orthogonal linear polarizations is measured by this receiver. Spectrometer bandwidths of 0.125, 0.25, 0.5, 1, 2, and 4 MHz are available.

Figure 4.3 shows how frequency-switched line observing is done with the DRAO 26m system. To observe the spectrum of an object, the receiver is first centred on the line of interest's rest frequency (f_{line}). For example, H166 α has $f_{line} = 1424.734$ MHz. The observer sets a frequency known as the first local oscillator (1st LO) to 150 MHz lower than f_{line} , and a reference LO frequency to a value $\Delta f + 150MHz$ lower than f_{line} , where Δf is typically $\frac{1}{2} \times bandwidth$. Thus, the 1st LO and REF LO are spaced by $\Delta f = 2MHz$ for a selected bandwidth of 4 MHz. The frequency switching system in place then alternately observes what is called the first intermediate frequency (f_{IF}), $\frac{1}{2}\Delta f$ below the 1st LO (at $f_2 = f_{line} - 150 - \frac{1}{2}\Delta f$) and $\frac{1}{2}\Delta f$ above the 1st LO frequency (at $f_1 = f_{line} - 150 + \frac{1}{2}\Delta f$). Each (roughly 10 second) cycle of this is converted to the 150 MHz range by $f_{line} - f_{IF}$, and the subtraction $f_1 - f_2$ is performed. The resulting spectrum is further reduced by 120 MHz, the second LO setting, and then by roughly 24 MHz (the third LO setting determined by both the suspected Doppler velocity of the rest frequency f_{line} and the Local Standard of Rest). The result is near 6 MHz, in the middle of the 4 - 8 MHz measurable range of the 256 channel spectrometer. Both polarizations are received through the above path, and are recorded as a 512 channel single spectrum of 10 sec. integration. Since these spectra are the difference between two observations centered on frequencies Δf above and below f_{line} , they will contain identical positive and negative signals spaced $2\Delta f$ apart. The many individual spectra of a long observation are averaged at the processing stage, and the positive and negative signals are folded together by subtraction of one half of the spectrum

from the other to produce a single, 256 channel spectrum of the object observed.

With consideration given to the receiver that was currently installed on the telescope, it was decided that detection of $H166\alpha$ line radiation would be attempted. Photons of rest frequency $\nu = 1424.734$ MHz (near the neutral HI line of 1420.406 MHz) are produced from this recombination ($n = 167 \rightarrow n = 166$).

A week long observing run during Feb. 7-14, 2000, on this line produced nothing conclusive. A broad line at the expected doppler frequency of NRAO655 appeared, but an unknown source of narrowband interference at a frequency immediately adjacent to this made the results difficult to trust. It was decided that another recombination line should be observed, to avoid this source of interference. Readily available with a filter change on the telescope's receiver was the $H158\alpha$ line, at a higher frequency (where $\nu = 1651.541$ MHz and $n = 159 \rightarrow n = 158$) and a narrower beam (31'). A positive (10.6σ) detection of $H158\alpha$ emission from NRAO655 was achieved with a cumulative integration time of 95.8 hours. A 3rd-order polynomial baseline was fit to the filter band shape and subtracted to produce the $H158\alpha$ spectrum of NRAO 655, shown in Figure 4.4.

4.4 THE DEVON 0.5M OPTICAL TELESCOPE

Until now, no positive optical identification of any object in the first table of Chapter 5 has been achieved, yet the science in waiting is enormous. Studies of a shell SNR's interaction with the dense clouds and density gradients in the interstellar medium are possible with optical images combined with those in radio and infrared continuum (Lozinskaya, 1992). Fundamental properties such as electron and gas density, temperature, and emission measure are available for those objects imaged in the optical lines of $H\alpha + [NII]$, $[OIII]$, $[OI]$, and $[SII]$. Such measures complement radio study, by permitting a comparison of related features detected in radio continuum and line images. Thus, the usefulness of a sensitive, wide field optical imaging telescope becomes apparent. The University of Alberta's 0.5m telescope at the Devon Astronomical Observatory is such an instrument.

The Devon design is based on a Cassegrain optical configuration. A 0.5 meter $f/3$ paraboloidal mirror sits in a short barrel on a fork-mounted equatorial drive. Various front-end tubes hold different secondary mirrors, and are interchangeable, allowing for short (Newtonian focus) and long (folded Cassegrain focus) effective focal lengths. The telescope is capable of keeping stars centered to better than the typical seeing limit of 3-5" over long unguided exposures, up to ~ 1000 seconds.

The telescope has been in use since 1979, and primarily fit with a dual channel photometer permitting simultaneous variable and comparison star measurements. However, the availability of sensitive CCD imagers in the early 1990's led to a collaboration between optical and radio astronomers on campus to develop the telescope into a leading instrument for wide field emission line imaging of

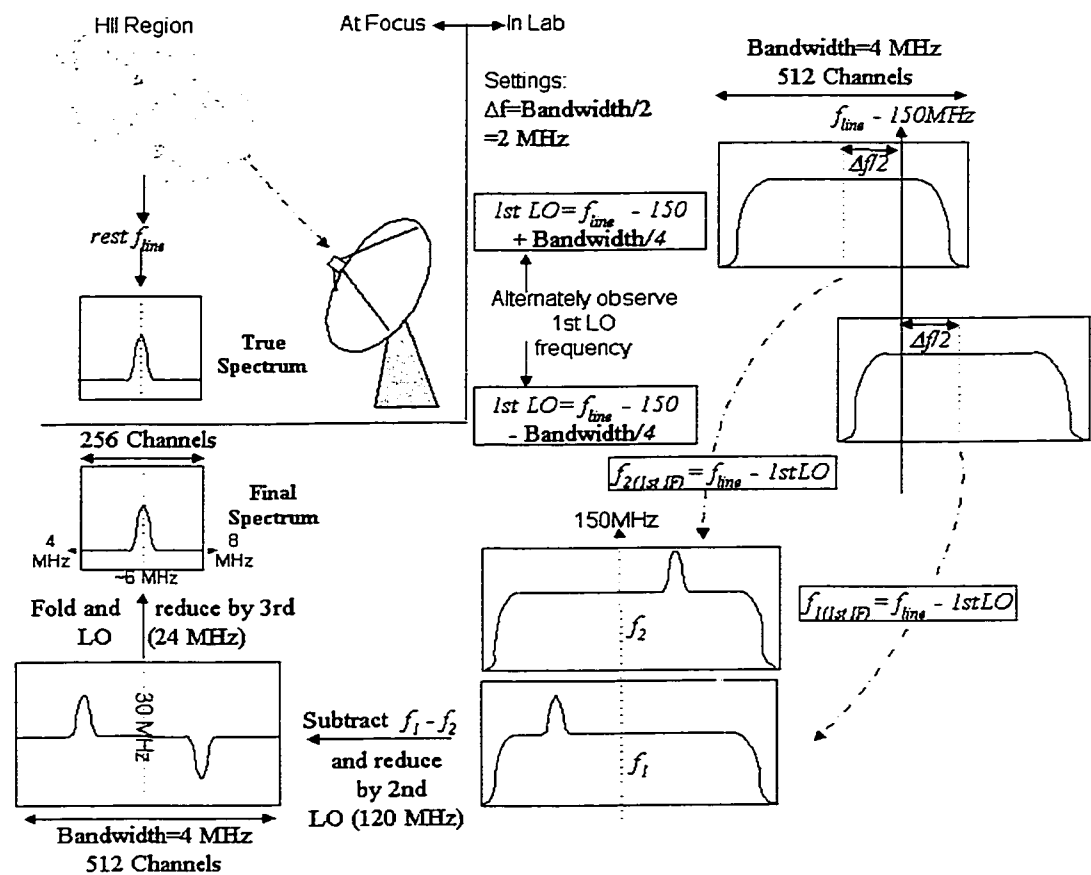


Figure 4.3: Frequency-switched observations of radio spectral lines with the DRAO 26m telescope.

H158 α Recombination Line - NRAO655

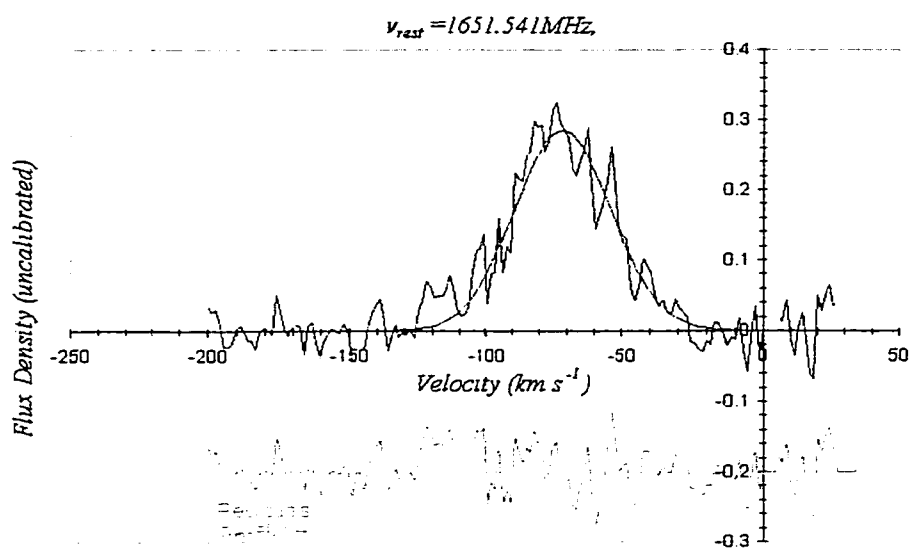


Figure 4.4: Radio recombination spectrum of NRAO 655, observed by the author with the DRAO 26m telescope. A 3rd-order polynomial baseline was fit to the filter band shape and subtracted to produce the curve shown. A Gaussian fit is overlaid on the broad $H158\alpha$ signal, and residuals plotted below. The $FWHM = 41 \text{ km s}^{-1}$ line is centered on -71.8 km s^{-1} .

SNR's and HII regions. The system has the advantages of a sensitive imager operating over a wide field, with efficient and observer-friendly control software taking advantage of the camera's capabilities. For particulars on the system design, the reader is referred to Foster et al., 1999, and Chapter 2 of this work.

Observations took place on moonless nights of good to very good transparency. The author arrived just prior to sunset to gather several (>20) filtered exposures of the dusk sky (at $\sim 80\%$ full well level of 65535 Analog-Digital Units, or ADU) with the camera focused for each filter of interest. The telescope was pointed near the zenith for these flat fields, since this part of the sky has the least gradient at twilight (Brian Skiff of Lowell Observatory, private communication). The field was moved slightly between individual flats to randomly relocate any stars present in the frame. After stellar images became apparent in flat frames, several (≥ 6) "dark" images of the chip's thermally generated signal were made until twilight had subsided enough to observe the target. Each dark frame was of equal integration time to the target frame (600 sec). Finally, many (>50) zero frames were collected and averaged using a clipped average routine (where the maximum and minimum values of a data series to be averaged are trimmed). The resulting image was later overscan subtracted, and plotted as a histogram for calculation of the readnoise (see Chapter 2 for plots and details). After collecting the zero data, observations on the target commenced.

Table 4.4 summarizes target observations carried out at the Devon AO from Sept. 1999 to January 2000. Occasional auroral displays during an observing session, combined with a finite number of clear nights in the seasonal visibility range of the objects, meant that it was not possible to observe all objects through all filters. On a given night, many frames of identical exposure length (600s) were obtained on the target objects through airmasses ranging from 1.0 to 1.4 (zenith angles of 0° to 45°). Extinction coefficients could be derived nightly from several field stars, but photometric measurements were poor, due to the very low brightness of these stars in the $H\alpha+[NII]$ filter.

More than twenty images per filter of each object in Table 4.4 were prepared from frames obtained on moonless nights of good transparency. The integration time of 600 seconds was chosen for several reasons: a) S/N concerns (Chapter 2), b) stars within the field do not saturate the CCD pixels in this time, and c) the telescope drive can easily keep a star image centered to within 1.5 - 2 pixels (the typical FWHM of the gaussian profile of a Devon stellar image). Each frame was processed very carefully, in the manner described below (see Chapter 2 for a description of CCD reduction techniques, and Chapter 3 for their implementations in software).

Every raw frame was first corrected for the additive overscan bias, using the 35 pixel wide strip appended to every 512×512 CCD image. To avoid contaminating the average overscan value with high counts, columns near the edge of the image (512-514) and the edge of the overscan strip (545-547) were avoided, since these columns contain pixels with higher than average counts. The raw object frames were then trimmed to 512×512 pixels. The average zero bias frame from the night was then trimmed, overscan corrected, and subtracted from target frames. The dark frames were calibrated for overscan and zero biases, and

Object	Field Center (J2000)	Frames	Total I_{time}	Filter
NRAO 655	$\alpha = 21^h 18^m 15^s$ $\delta = 51^\circ 55' 40''$	22	13200	H α + [NII] 656.3nm
3C434.1	$\alpha = 21^h 25^m 4^s$ $\delta = 51^\circ 52' 52''$	16	9600	H α + [NII] 656.3nm
3C434.1	$\alpha = 21^h 25^m 4^s$ $\delta = 51^\circ 52' 52''$	28	16800	[OIII] 502.1nm
3C434.1	$\alpha = 21^h 25^m 4^s$ $\delta = 51^\circ 52' 52''$	22	13200	[SII] 671.8nm
G93.6+1.3	$\alpha = 21^h 22^m 0^s$ $\delta = 51^\circ 47' 30''$	13	7800	H α + [NII] 656.3nm

Table 4.4: Summary of Observations of CGPS J8 Field Objects, carried out at the Devon AO. Note: G93.6+1.3 was observed during bright sky conditions (full moon).

trimmed. A median algorithm was used to combine all darks into one master frame per night. Calculation of the median of these data removes cosmic ray events (pixels with inordinately high counts), which were obvious. All darks were purposely collected with an integration time of 600s, and thus the master frame was simply subtracted from the same night's target frames without being scaled. Each flat field was processed (to remove overscan, zero, and dark noise additions), trimmed and median combined (to remove stars) into one master frame per filter. The master flat field was normalized (divided by its own mean), and finally, every target frame was divided by its corresponding filter's flat field.

The resulting processed object images were inspected, and measured to have average sky backgrounds across the frame that were flat (consistent) to better than 1% on small (25 pixels) scales. Large scale gradients were not present, and faint nebulosity present would not be lost amid such gradients. Each image was shifted to register with the first to within 0.01 pixel, and all frames were scaled to a common airmass of $X = 1.0063$, and a composite frame was made.

The technique of compositing increases the S/N of faint objects, but due to the readout noise of each frame (a constant of the CCD chip), the gain is not as dramatic as a single, longer integration time would produce. For a constant night sky background, compositing n images increases the S/N as:

$$\frac{S}{N} \approx \sqrt{n} \frac{N_{obj}}{\sqrt{N_{obj} + N_{sky} + N_{dark} + n \times r_e^2}} \quad \text{eq. 5.1}$$

where $N_{obj} \equiv$ counts (ADU) from the observed object in a single frame, $N_{sky} \equiv$ counts from sky background in a single frame, $N_{dark} \equiv$ dark counts in a single integration, and $r_e \equiv$ readout noise. If not for instrumental noise and the night sky background, the S/N would be the noiseless, Poisson result of $\sqrt{N_{obj}}$, and would increase as \sqrt{n} . One can see that due to readnoise, a very large number of individual integrations is undesirable, especially on faint objects, as one quickly reaches a point of no gain in the S/N. However, long exposures have

problems of their own, being limited by an increasing N_{sky} (of which the error contribution is $\sqrt{N_{sky}}$), as well as such factors as blooming and trailing. The *sky fog* limit is reached when the S/N no longer increases significantly with a long integration. At observatories such as Devon (with sky limited sites and low readout noise CCD chips), compositing offers a way of increasing S/N on faint objects, with modest penalties in precision.

The composite image of NRAO 655, assembled from 22 single frames, is presented in Figure 4.5. Significant optical nebulosity is present near the areas of radio-bright thermal emission (Figure 4.6). To better measure this optical nebulosity, the stars in the composite image were removed by point spread function (PSF) fitting routines found in IRAF. (see Figure 4.7). However, stars that were saturated were not removed. These stars appeared in the composite image with low brightness haloes surrounding them (see Chapter 2, section 2.8 for an explanation of this effect). Since nebulosity from NRAO 655 is expected to be dim, the signal present in the composite could be confused with these optical artifacts. Is the nebulosity seen produced by the sum of haloes from nearby stars?

To answer this question, many measurements of the background, the halo from the brightest field star (SAO 33306 near the N corner of the frame, $m_V = 8.3$), and the brightest portion of nebulosity (the north-west piece) were taken and the mean and standard deviation reported for each area. Since the CCD's response to signal is linear (Chapter 2), we can find the magnitude of a star needed to produce a halo as bright as the NW patch of emission. This magnitude is $m_V = 7.83$, but there are no stars brighter than SAO 33306 in the frame. Surrounding the NW patch of emission are eight stars of magnitudes $m_V = 11.6$, $m_V = 11.6$, $m_V = 12.1$, $m_V = 12.7$, $m_V = 12.8$, $m_V = 13$, $m_V = 13.1$, and $m_V = 14.4$. Collectively, these stars could produce the equivalent halo of a 10.1 magnitude star (accounting for only 12% of the flux from that area). However, these stars are spread out enough to prevent their haloes from summing in this way. The halo from a single bright star ($m_V = 11.6$) within the NW patch is essentially the readnoise of one image (9 ADU), and would be undetectable in each of the frames that make up the composite. It is therefore safe to conclude that the nebulosity seen is not produced or significantly affected by the optical artifacts of nearby stars.

The nebulosity seen in the NRAO 655 composite cannot be accounted for by flat fielding errors, or optical artifacts from stars. When convolved to approximately 1' resolution, the contoured appearance of the emission is very similar to the shape of NRAO 655 in 21 cm and 74 cm radio maps, and in 60 μm and 100 μm infrared maps (see Chapter 5 for comparison images). Furthermore, areas of strong $H\alpha$ emission appear where emission from dust is minimum in 60 μm and 100 μm IRAS images of NRAO 655 (also shown in Chapter 5). This body of evidence strongly suggests the $H\alpha$ emission seen is originating from NRAO 655. This represents the discovery of emission from this HII region at optical wavelengths.

Irregular aperture photometry was performed on NRAO 655, with contours serving as a guide for drawing the polygon encompassing the nebula. The in-

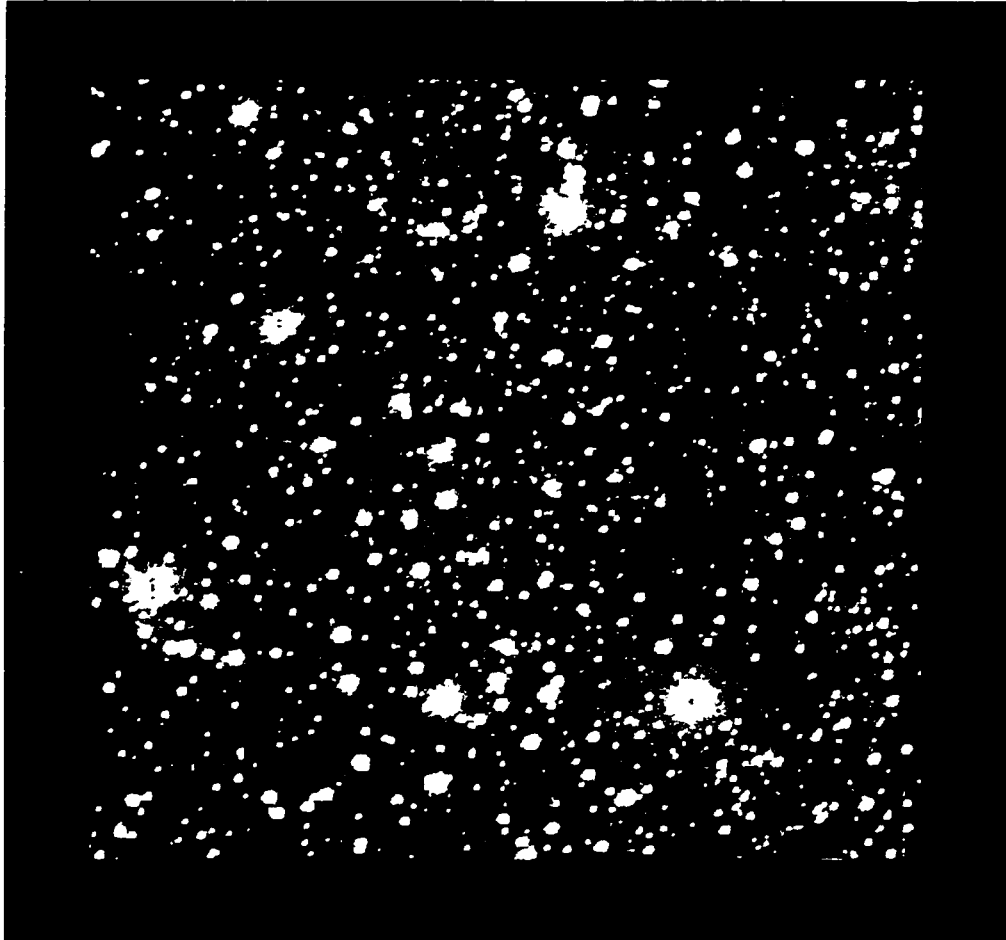


Figure 4.5: $H\alpha + [NII]$ ($\lambda_{\text{centre}} = 656.3$ nm, FWHM=7.5 nm) emission composite image of NRAO 655 obtained at the Devon AO with a cumulative integration time of 13200 seconds. North is toward the lower-left corner of the frame, and east is to the lower right. Greyscale runs linearly from 300 ADU (dark) to 700 ADU (light).

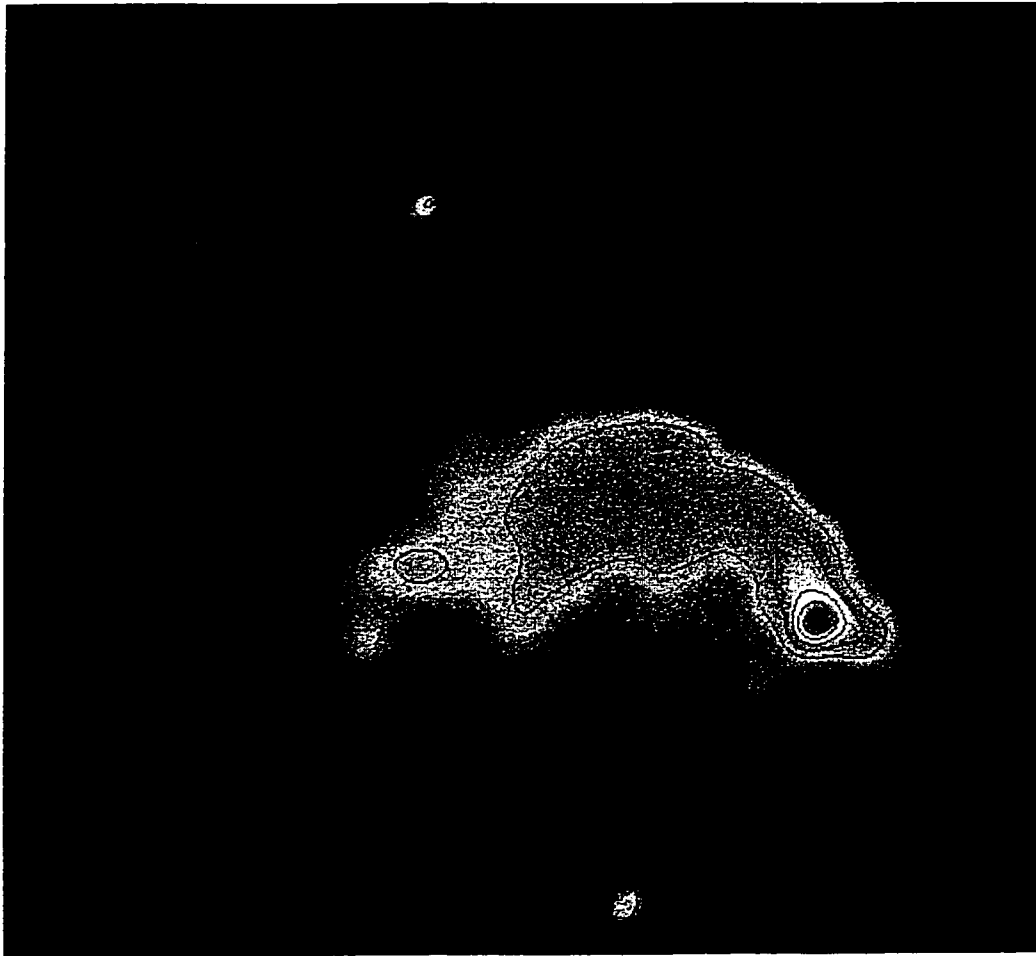


Figure 4.6: 21cm DRAO ST image of NRAO 655 scaled and rotated to match the DevonAO field size and orientation. Contours are from 21cm brightness temperatures (1.65K, 2.7K, 3.7K, 4.8K, 5.9K, 6.9K).

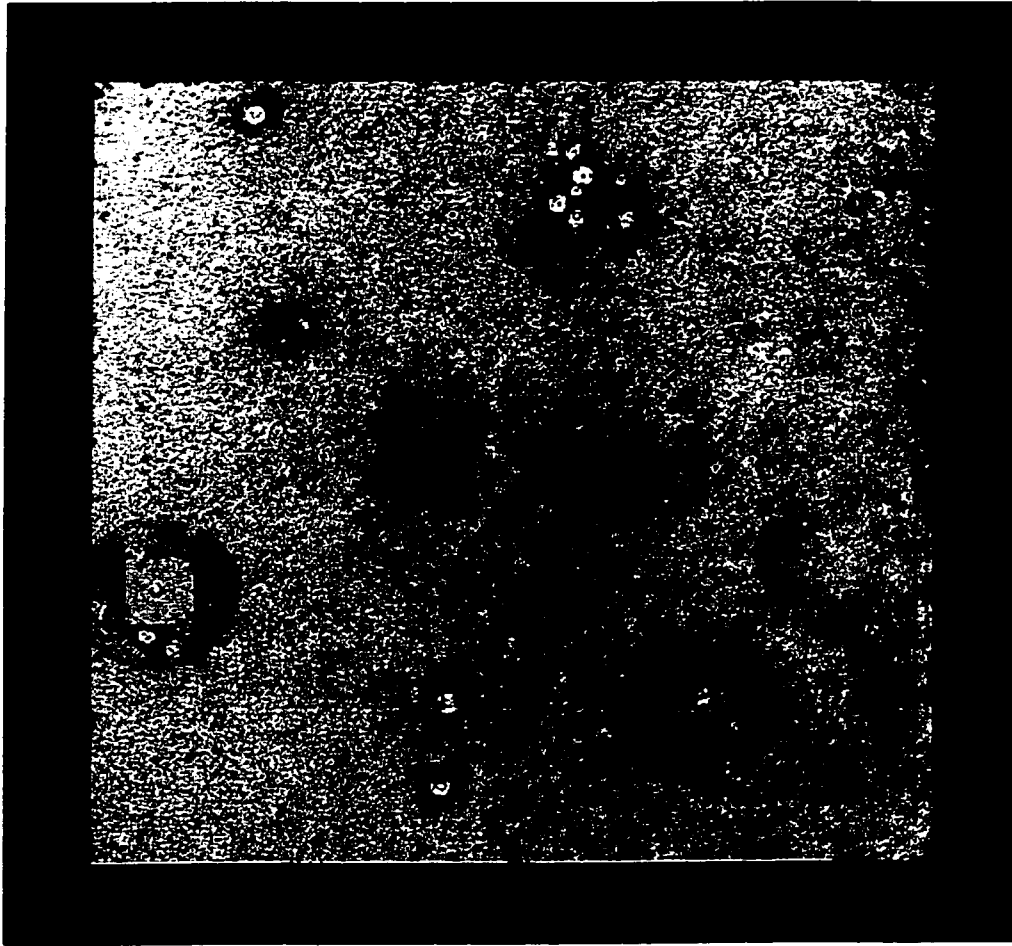


Figure 4.7: $H\alpha$ composite frame (same orientation as Figure 4.5) with stars removed and displayed with an inverted greyscale to highlight emission features. Greyscale is from 600 ADU (dark) to 400 ADU (light).

strumental $H\alpha$ flux (in ADU) of NRAO 655 was measured in this manner. To transform this to a standard system, observations of several bright planetary nebulae in the $H\alpha$ filter were obtained on April 21, 2000. Chosen were NGC 6720, NGC 6543, and NGC 6210. Each planetary was observed at several different airmasses, and its extra-atmospheric instrumental magnitude found (see Figure 4.8). The $H\alpha$ extinction coefficient from these observations was used for that of NRAO 655, since both observations occurred on nights of good transparency. The photometry on NGC 6720 (M57) was of the highest quality, so this nebula was used for calibration.

Emission line intensities at six positions on M57 were observed by Hawley et al. (1977). Spectra were obtained for the $H\alpha$ (656.3 nm) and both [NII] lines (654.8 nm and 658.3 nm) at a FWHM resolution of 0.4 nm, and corrected for atmospheric extinction. Entrance apertures were $2''.4 \times 4''.0$ (or $2.256 \times 10^{-10} sr$). Reported by Hawley are individual line intensities ($erg\ cm^{-2}s^{-1}$) normalized to the $H\beta$ line. Two of Hawley's positions were chosen for calibration: position 1 ($8''.4E$ and $2''.1S$ of the central star, $F_1(H\beta) = 8.21 \times 10^{-14} erg\ cm^{-2}s^{-1}$) on the dimmer central portion was within the ring, and position 4 ($26''.6W$ and $2''.1S$ of the central star, $F_4(H\beta) = 1.91 \times 10^{-13} erg\ cm^{-2}s^{-1}$) was on the bright ring itself. The sum of the three line intensities was converted to $Wm^{-2}sr^{-1}$ for each position, and the average of these two values was used. The average $H\alpha + [NII]$ intensity found by Hawley et al. for M57 is $5.4 \times 10^{-6} \pm 8.1 \times 10^{-7} Wm^{-2}sr^{-1}$, not corrected for interstellar reddening.

The extra-atmospheric m_{inst} of M57 (as observed at the DevonAO) was converted to an instrumental flux (4721906.5 ± 10405.8 ADU) and finally to an intensity ($1.413 \times 10^{13} \pm 3.11 \times 10^{10} ADU sr^{-1}$). A first order coefficient was then found for transforming DevonAO observations to those of Hawley:

$$\frac{F_{M57}(Hawley)}{F_{M57}(DevonAO)} = 3.82 \times 10^{-19} \pm 5.74 \times 10^{-20} Wm^{-2} ADU^{-1}$$

The $H\alpha$ extinction coefficient from the M57 observations ($k'_{H\alpha} = 0.261 \pm 0.021$) was used to find NRAO 655's extra-atmospheric instrumental intensity ($6.93 \times 10^{10} \pm 5.82 \times 10^9 ADU sr^{-1}$). Finally, the integrated $H\alpha + [NII]$ line intensity of NRAO655 was found as:

$$\frac{F_{M57}(Hawley)}{F_{M57}(DevonAO)} \times F_{NRAO655} = 2.65 \times 10^{-8} \pm 5.07 \times 10^{-9} Wm^{-2} sr^{-1}$$

Converted to Janskys ($1Jy = 10^{-26} Wm^{-2} Hz^{-1}$) this becomes $4.79 \pm 0.92 Jy$. NRAO655 is 204 times fainter (5.8 magnitudes) than M57 in $H\alpha + [NII]$ light at the surface of the Earth.

Sources of possible error for this calibration are numerous. Flux measurement uncertainties of M57 (manifested as the error in extra-atmospheric instrumental magnitude) amounted to only 0.2%. Differences in $k'_{H\alpha}$ for observations of NRAO 655 and M57 are likely to be small, as well. The low S/N of NRAO 655 itself accounts for the bulk of the uncertainty. Using Howell (1992), p. 133, equation 2 gives $S/N=12$ (or, uncertainty $\sigma \sim \frac{S}{N}^{-1} = 0.08$) for the 22 image composite of NRAO 655. Errors reported by Hawley in line intensities of M57 are large as well ($\pm 15\%$). The final error reported for NRAO 655 is 19%.

In the next chapter the astrophysics of NRAO 655 is extracted from the processed data presented here, and from data observed at other wavelengths.

H α Extinction Plots for 3 Planetary Nebulae

Observed at Devon AO 2000/04/21

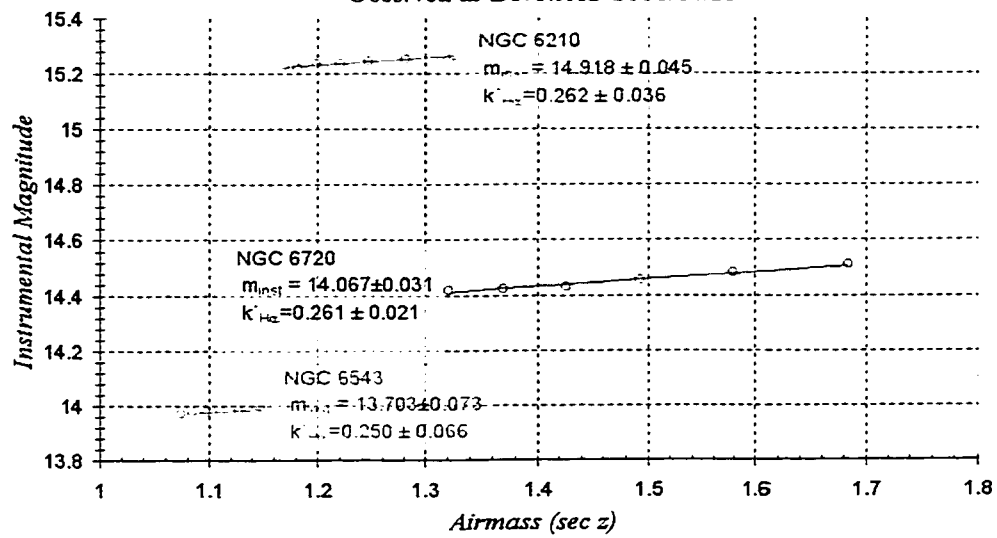


Figure 4.8: Planetary nebulae observations for calibrating H α emission line intensity of NRAO 655. Extra-atmospheric instrumental magnitudes (m_{inst}) are intercepts at $airmass = 0$, and extinction line slopes denote the H α extinction coefficient $k'_{H\alpha}$.

4.5 REFERENCES

Clark, B. G., 1980, *A&A* 89, 377.

Foster T., Hube D., Couch J., Martin B., Routledge D., and Vaneldik F., 1999, *ASP Conference Series* (E. Craine, R. Tucker and J. Barnes, editors) 189, 111.

Haslam C.G.T., Salter C.J., Stoffel H., and Wilson W.E., 1982, *A&AS* 47,1.

Hawley S.A., and Miller J.S., 1977, *ApJ* 212, 94.

Howell, S.B., 1992, *ASP Conference Series* (Steve B. Howell, editor) 23, 105.

Kallas E., and Reich W., 1980, *A&AS* 42, 227.

Lozinskaya, T. A. *Supernovae and Stellar Wind in the Interstellar Medium*. American Institute of Physics, New York, 1992.

Steer D. G., Dewdney P. E., and Ito M. R., 1984, *A&A* 137, 159.

Chapter 5

HII REGION NRAO 655 AND THE GALACTIC ENVIRONMENT NEAR $l = 94^\circ$

5.1 SUMMARY

Radio, optical, and infrared emission observations of galactic surroundings near $l = 94^\circ$ are compared, revealing new information about the medium and objects in this locale. Presented in this chapter are new continuum and line observations of objects in the J8 field of the CGPS: HII region NRAO 655 and supernova remnant 3C434.1. Continuum radio ($\lambda = 21$ cm and $\lambda = 74$ cm) and infrared ($\lambda = 12 \mu\text{m}$, $25 \mu\text{m}$, $60 \mu\text{m}$, $100 \mu\text{m}$) wavelengths, and emission line observations at optical ($\lambda_{H\alpha} = 656.3$ nm) and radio ($\lambda = 21$ cm) wavelengths are presented. Radio spectra of these objects confirm their emission as either thermal or non-thermal in origin. HI cavities and shells are found associated with these objects, and confirm the implied kinematic distance of NRAO 655 (8.85 kpc, far side of the Perseus spiral arm) with that determined from recombination line spectra. The astrophysical properties of the ionized region and surrounding neutral hydrogen are discussed, and a physical model for NRAO 655 is proposed. The first ever detection of optical emission line features from both objects is presented as CCD images, and the $H\alpha$ emission line intensity for the HII region is determined. NRAO 655's shape and structure is compared in different wavelengths, and a good correlation between optical-radio and infrared-radio morphology and anti-correlation between optical and infrared features is found. Electron densities, emission measures and the mass of optically emitting material in NRAO 655 are derived from the optical image, and compared to similar values found from radio observations. Integrated infrared flux densities are found for this object as well. A statement on the probability of a common interstellar medium shared by NRAO 655 and 3C434.1 is made, and evidence is presented.

Name	Alias	Type	v_{LSR} (km s ⁻¹)	References
G93.1+2.8	CTB 102, KR1	HII	$v=-58$	9,12
G92.7+3.1	WB43, Mol 133	HII	$v=-6.1,-6.5,-6.8$	3,4,5
G94.4+2.6	KR6			6,7
G93.7+2.6	KR4			6,7,8
G93.0+2.0	NRAO 652	HII		1,2
G92.3+1.5				10
G93.9+1.6	Mol 135, WB93	HII		3
G94.3-0.3	CTB 104A	SNR		2,11
G93.4+1.8	NRAO 655	HII		2
G94.0+1.0	3C434.1	SNR		2,11
G91.11+1.58	BG 2107+49	HII complex	$v=-80 \pm 1$	10

Table 5.1: A list of HII regions and supernova remnants present in the rich galactic region near $l=94^\circ$ seen in Figure 5.1. Kinematic distances are published for only two of the objects: CO and NH₃ velocities were found for WB43 by Wouterloot (et al.) and Molinari (et al.) respectively, while H112 α recombination line observations of BG2107+49 by Higgs et al. placed this object at $v=-80$ km s⁻¹. An unpublished velocity ($v=-58$ km s⁻¹) for CTB 102 was obtained by Fich, 1983 observing H109 α recombination line (5 GHz). References: (1) Pauliny-Toth et al. 1966; (2) Mantovani et al. 1982; (3) Molinari et al. 1996; (4) Miralles et al. 1994; (5) Wouterloot and Brand 1989; (6) Fich 1986; (7) Kallas and Reich 1980; (8) Reich et al. 1990; (9) Galt and Kennedy 1968; (10) van der Werf and Higgs 1990; (11) Landecker et al. 1985; (12) van der Werf and Higgs 1991.

5.2 INTRODUCTION TO OBJECTS NEAR $l=94^\circ$

The rich region of the galactic plane near $l=94^\circ$ is home to a number of HII regions, and at least two SNRs, 3C434.1 (G94.0+1.0) and CTB 104 A (G93.7-0.3) (see Figure 5.1). These SNRs have received more extensive attention than the HII regions by previous observers, but the distance to these objects is still essentially unknown (see Table 5.1). Mantovani et al. (1982) find a Σ -d-z distance to the large apparent diameter SNR CTB 104 A of 2.5 - 3.1 kpc, and 4.5 - 6.4 kpc for the smaller apparent diameter 3C434.1. Landecker et al. (1985) classify 3C434.1 as a shell type remnant on the basis of its circular appearance and steep outer rim, but do not find a distance. Except for BG2107+49 and WB43, most of the HII regions have no published distances ascribed to them. A weak emission background envelops the entire region with darker patches at many radio wavelengths, and a patchy emission structure in the optical H α line. In particular, the field of SNR 3C434.1 and NRAO 655 gives the impression of being one physical complex, with emission extension of the SNR blending with NRAO 655. The author has studied this region at high resolution in radio, optical and IR wavelengths, and presents the first comprehensive solution for the objects in this field.

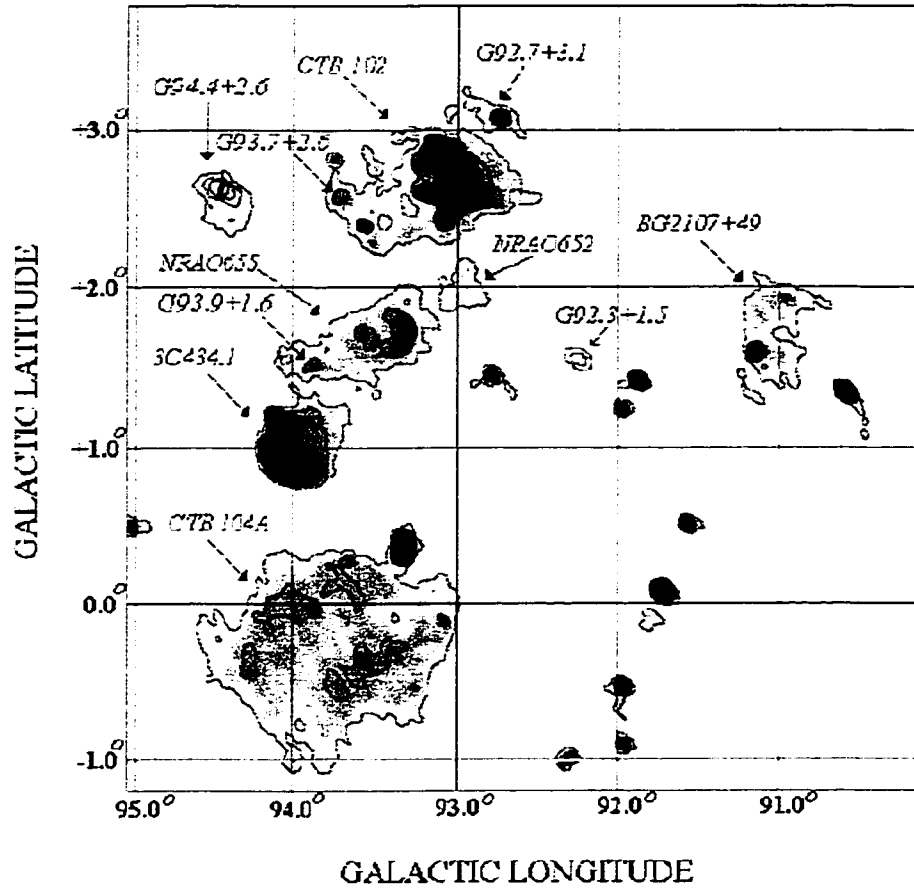


Figure 5.1: A DRAO 74cm map of the galactic region near $l=94^\circ$, showing the location of objects listed in Table 5.1. Note the two supernova remnants 3C434.1 and CTB 104A among the number of HII regions in the field.

NRAO 655 (G93.4+1.8) is an emission nebula situated near the galactic plane in northern Cygnus. It has been identified previously only at radio and infrared wavelengths. Its positive identity as a thermal emitter has not always been certain. A crescent form and shell structure, as observed by Velusamy and Kundu (1974) and later by Mantovani et. al. (1982) with the Effelsberg 100m radio dish, along with an inferred spectral index of $\alpha = 0.30 \pm 0.05$, led to their suggested SNR classification. On the basis of a measured spectral index of $\alpha = 0.04 \pm 0.03$, Goss et. al. (1984) tentatively reclassified NRAO 655 as an HII region, leaving suggestions that it could be an unusually flat spectrum SNR. Arendt (1989) classes it with other galactic SNRs in his infrared survey of these objects, but notes the possibility of confusion with other types of galactic objects. No previous recombination line observations of this object have been made, but are suggested by Goss as a logical step towards a definitive identity.

Typical flux densities found by other observers for this object are in the range of 6.0 - 6.9 Jy (± 0.7 average), over a spectral range of 608.5 MHz to 4.75 GHz, somewhat lower than current measurements, but comparable to other galactic HII regions (e.g. S183, Landecker et. al., 1992). The object is apparently brighter at lower frequencies. Caswell (1970) found $S = 14.4 \pm 3.0$ Jy at 178 MHz, although it is demonstrated by Goss that this flux density is highly discordant with others (this value was the cornerstone of Mantovani's steep spectral index, and subsequent designation of NRAO 655 as a SNR).

Previous derived distances for NRAO 655 have placed this object in the Perseus spiral arm. Early classification of this object as a SNR led to Σ -d-z relation determined distances. The group led by Mantovani (1982) found a distance of 4.3 - 6.5 kpc, at 135-206 pc above the galactic plane, based on this classification. As a result of subsequent work on the nature of NRAO 655, this distance must be concluded to be erroneous. No work on HI along this object's line of sight has been done previously, and no optical identification of NRAO 655 has ever been made. Thus, a radial velocity derived from HI cavities or $H\alpha$ line emission is not available, and a kinematic distance for NRAO 655 has not previously been measured.

Filling a void that was recognized by Goss, high angular resolution radio observations of the region are presented. This thesis intends to show definitively the identity of NRAO 655 as an HII region, and presents HI and recombination line observations, providing evidence that it lies just beyond the Perseus spiral arm of the Galaxy. Presented are the first optical images of this nebula, and a comparative study of its morphology at radio, optical, and infrared wavelengths is offered. A proposed physical model of NRAO 655 demonstrates physical conditions within the nebula, and its possible evolution and age.

5.3 STRUCTURE AND APPEARANCE OF OBJECTS NEAR $l=94^\circ$

Images at many different wavelengths present a unique opportunity to comparatively study an object's morphology as seen throughout the electromagnetic spectrum. We shall first look at the high resolution radio image of SNR 3C434.1 at 21cm, and then concentrate on a comparative look at NRAO 655 in radio, optical, and infrared wavelengths.

Although the remnant 3C434.1 is not visible at infrared wavelengths, it is very detailed in the radio regime, is visible in Xrays, and resides within an optical field of patchy $H\alpha$ line emission (see Figure 5.3). The DRAO 1420 MHz continuum map (Figure 5.2) shows it to be highly circular with a diameter 29 arcminutes, centered on $l = 93.95^\circ, b = 1.05^\circ$. The appearance is of a spherical balloon being ripped open on the west side and spilling gas in this direction. Hook like features over the remnant's face give a knotted appearance, with a very prominent hook at the southern edge of 3C434.1. The remnant quite nicely displays shell-type SNR structure, with a brighter rim wrapping more than 180° clockwise across the eastern edge from S to NNW. The author finds the eastern rim circular, matching a $29'$ circle to better than $1'.5$ around this partial circumference, also a finding of Landecker et al. 1985. Emission visibly drops towards the west, and is seen extending from the remnant's centre towards $l = 93.6^\circ, b = 1.3^\circ$. Willis (1973) suggests this westward extension is a background feature, while Landecker et al. (1985) conclude that the emission seen in this area displays the same spectral index as the SNR. The author's present work using spectral index maps (see section 5.4) shows, however, the existence of non-thermal emission in this area. The bright point source on the north edge is 4C 51.54, and is found to have a flux density of $S = 1.019 \pm 0.006 Jy$. Landecker notes a steep spectral index for 4C 51.54, and concludes that it is extragalactic.

Optically, 3C434.1 is in a field of patchy $H\alpha + [NII]$ emission (Figure 5.3). No significant emission from 3C434.1 was seen in deep OIII ($\lambda_{OIII} = 502.1$ nm) and SII ($\lambda_{SII} = 671.9$ nm) emission line CCD images. There seems to be a NS band of absorption running through the brightest portion of 3C434.1 (inner contour, $T_b = 4.85K$), and optical emission flanking much of the south-eastern rim, in particular from the hook feature on the southern-most edge. A patch of emission also appears directly west (outside the brightest 21cm contour). The features range from 4σ to 5σ above the sky background. Whether this emission represents that from the remnant or not is undetermined.

The radio structure of NRAO 655 is remarkably similar to that of the neighboring SNR. NRAO 655's "head" is highly hemispherical, and the nebula is symmetric along an axis nearly parallel to the galactic plane. At $\lambda = 21$ cm (Figure 5.4), within brightness temperature contours of $T_b \geq 1.7K$, the head is a hemisphere of diameter $25'.5$, around a 180° perimeter clockwise from $l = 93.35^\circ, b = 2.0^\circ$ to $l = 93.35^\circ, b = 1.6^\circ$. A smaller, brighter portion (the "kernel") resides inside the head (within brightness temperature contours $T_b \geq 5K$), and is semi-circular (diameter= $12'$) with a mean $T_b = 7K$. The

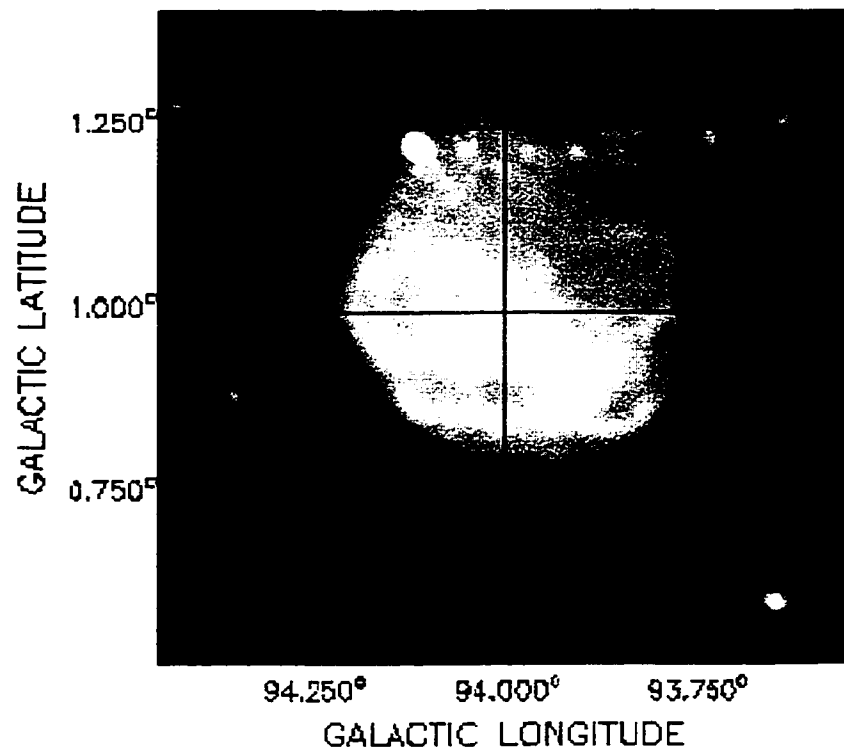


Figure 5.2: DRAO ST continuum image of SNR 3C434.1 at $\lambda = 21\text{cm}$ with galactic coordinates displayed. North is towards the upper-left corner, and east the lower-left.

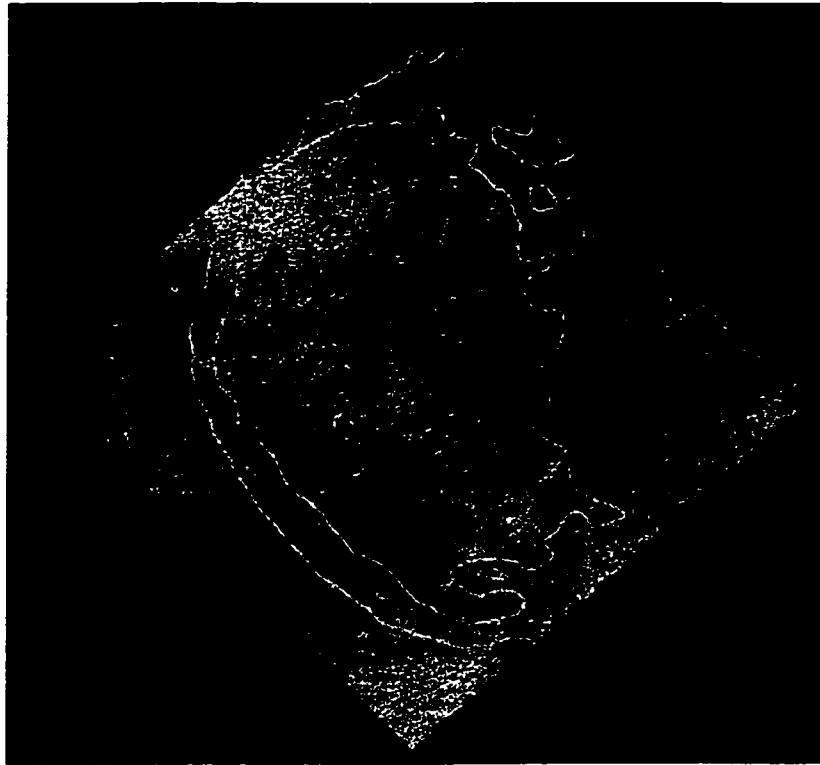


Figure 5.3: DevonAO $H\alpha + [NII]$ image of 3C434.1 with $\lambda = 21cm$ brightness temperature contours (2.0K, 4.85K) displayed. North is up. Optical image (stars removed) has been inverted to highlight nebulosity (emission is dark).

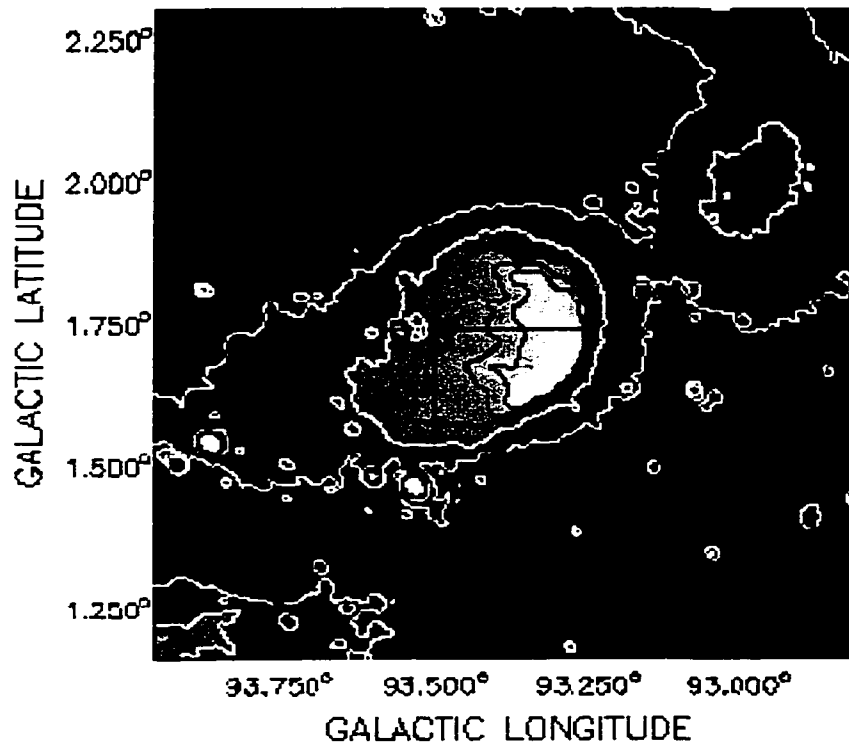


Figure 5.4: DRAO ST continuum image of NRAO 655 at $\lambda = 21\text{cm}$ with galactic coordinates displayed. The SNR 3C434.1 is immediately east of this emission, at $l = 94.0^\circ, b = 1.0^\circ$. NRAO 652 is visible at $l = 93.0^\circ, b = 2.0^\circ$. Contours are brightness temperatures at 1.6, 2.6, 3.3, 4.2 and 5.0 K.

Radial Profiles of NRAO 655's Tail

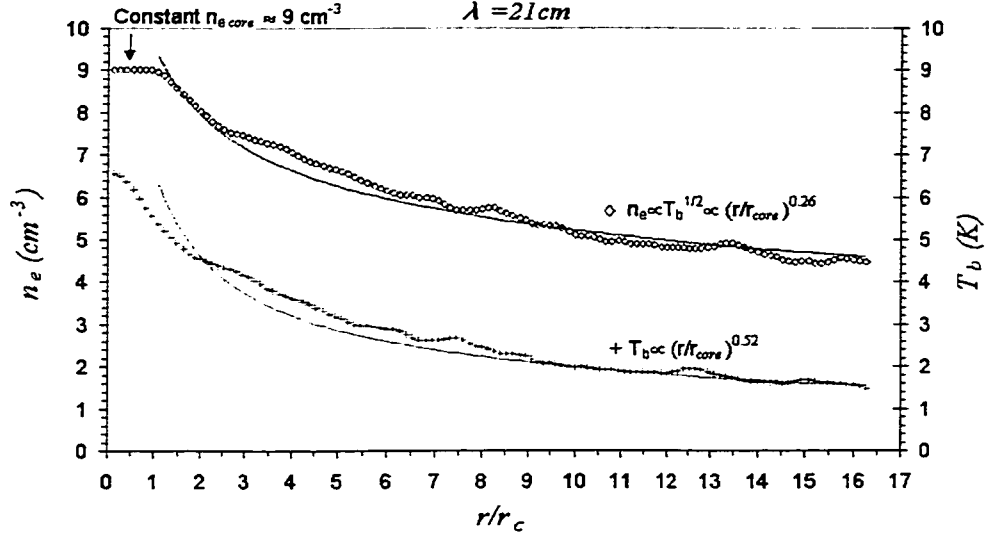


Figure 5.5: Radial brightness temperature (T_b) and electron density (n_e) profiles through the tail of NRAO 655. T_b values are from the 21 cm DRAO ST image. Solid line is a least squares power law fit to density profile (eq. 5.2). Radius is measured eastward from the centre of the semi-circular kernel.

kernel is also visible at $\lambda = 74\text{cm}$ as a somewhat more bowl-shaped hemisphere within $T_b = 150\text{K}$ contours. At $\lambda = 11\text{cm}$, the kernel is kidney bean shaped within $T_b = 0.65\text{K}$ contours. Both 74cm and 11cm wavelengths at a similar resolution of $4'$ show the kernel with a diameter of $17'.5$. Emission from the tail of the nebula drops off to the east closely following a power law $T_b \propto r^{-w}$. The variation in T_b through the tail is probably due mostly to changes in optical depth τ along the tail, and less to physical temperature variations. For a constant electron temperature:

$$\tau \propto \int n_e^2 dx \propto \langle n_e^2 \rangle D \quad \text{eq. 5.1}$$

where D is the path length through the tail along the line of sight. This is assumed constant along the tail, and since $T_b = \tau T_{\text{physical}}$, the optically thin, ionized gas in NRAO 655's tail thus has an electron density profile:

$$n_e(r) = n_c \left(\frac{r}{r_c} \right)^{-\frac{1}{2}w} \quad \text{eq. 5.2}$$

where $n_c \equiv$ ion density in the kernel (semi-circular radius $r_c = 6'.4$). It is shown later that $n_c \approx 9\text{cm}^{-3}$ for the head. Figure 5.5 shows brightness temperature and density fall-off for NRAO 655's eastward extending tail.

The kernel portion of NRAO 655's head is visible at all four IRAS infrared bands ($\lambda = 12 \mu\text{m}$, $25 \mu\text{m}$, $60 \mu\text{m}$ and $100 \mu\text{m}$). The appearance is mottled, with areas of high emission (and hence dust density) at the rim surrounding

central patches of low emission. A “finger” of dust extends from the SE portion of the head almost directly east a full 7 arcminutes. No such structure exists in any radio map of the nebula. Figure 5.6 shows the good correlation between the nebula’s morphology in radio and $\lambda = 60 \mu m$ wavelengths. The appearance of the kernel at $\lambda = 21$ cm is more uniform, however the overall shape of this dust is similar to the radio continuum shape of NRAO 655. It is thus reasonable that the dust seen along this line of sight is not uniformly distributed, but associated with NRAO 655. Similarly good correlation exists in all bands.

Optical emission from NRAO 655 has never been detected prior to this study. No nebulosity in the area is visible in the POSS-1 (Palomar Observatory Sky Survey) plates, nor seen in any of the narrowband images produced by Parker et al, 1979 for their Milky Way emission line survey. However, a deep $H\alpha + [NII]$ line CCD image reveals significant nebulosity (see Figures 4.4 and 4.6, Chapter 4) at NRAO 655’s position on the sky. With stars removed, the composite image was block averaged to $\approx 1'$ resolution, and contoured to 4σ , 5σ , and 6σ levels above the background to produce the contours seen in Figure 5.7. The semi-circular shape of the emission nebulosity is unquestionably similar to NRAO 655 in both radio and IR regimes. The “kernel” is outlined well by the 5σ contour lines, as is another smaller piece $< 1'$ NE of the kernel. A 5σ “finger” nearly identical in shape and length to that found in the IR image is visible extending 7 arcminutes NE from the SE edge of the head. The SW edge of the head itself is outlined by the 4σ contour line.

When one overlays the $\lambda = 656.3nm$ contours onto a similar scale $\lambda = 21cm$ radio map, the similarity in shape between these two wavelengths is striking (Figure 5.8). The $H\alpha + [NII]$ emission appears to come from the kernel only, the brightest portion of NRAO 655 at radio wavelengths. Thus, the brightest optical emission correlates with the brightest radio emission. The optical “finger” appears to arise from an area of intense radio emission, and extend E into the weaker radio head.

Even more dramatic is a comparison of NRAO 655’s appearance at IR and optical wavelengths. Figure 5.9 shows the $\lambda = 656.3nm$ contours atop the infrared map at $\lambda = 60\mu m$. IR emission outlines the edges of optical nebulosity. The bright areas of $H\alpha + [NII]$ emission correspond to dim areas of infrared (dust) emission. It is probable that the high amount of dust in these areas is obscuring optical light, which itself shows through areas of weaker dust emission. The optical and IR “fingers” are identical in length, but are seen side by side rather than superimposed, more evidence for anti-correlation between optical and IR emission.

The correlation of this nebula’s optical appearance with radio structure and anti-correlation with IR morphology is convincing evidence that the $H\alpha + [NII]$ emission detected originates with NRAO 655, and not elsewhere.

The integrated flux density of $H\alpha + [NII]$ emission within the 4σ contour (111.44 square arcminutes) was found to be $4.79 \pm 0.92 Jy$ (110.15 ± 21.07 Rayleighs, see below). We can find the emission measure and rms electron density of the kernel using the following equations (Reynolds, 1988):

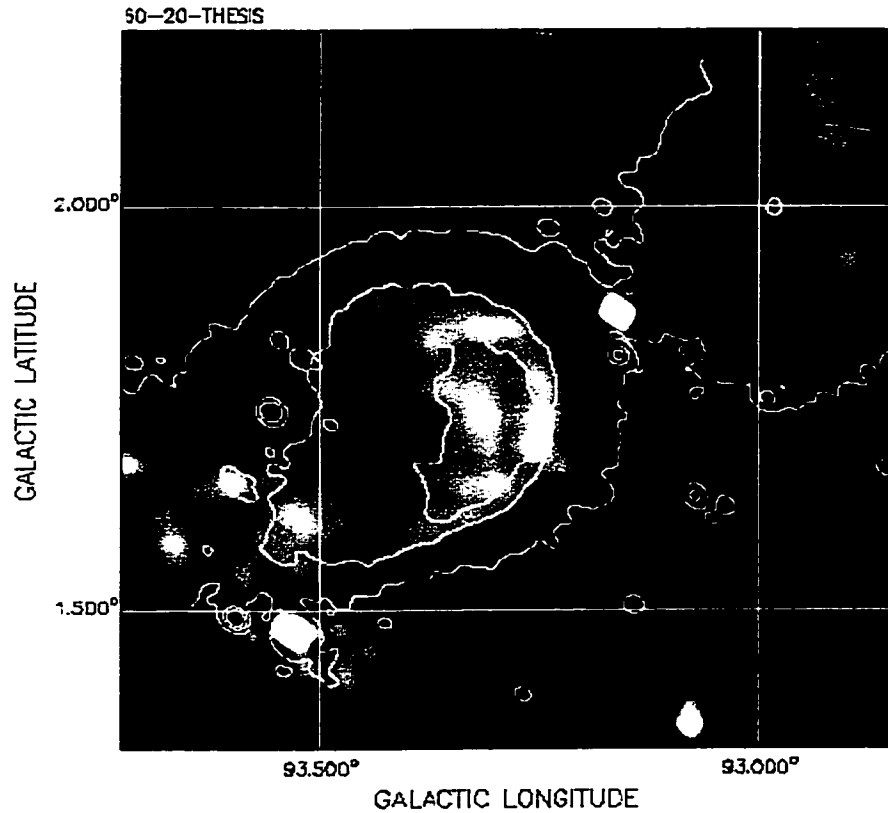


Figure 5.6: $60 \mu m$ IRAS image of NRAO 655, iterated 20 times in a deconvolution technique (Maximum Correlation Method). Artifacts (“ringing”) around point sources are produced by MCM. Contours are brightness temperatures ($1.6K$, $3K$, $5K$) from a 21cm DRAO ST image of NRAO 655. North is up. The $7'$ finger runs ESE from $l = 93.3^\circ, b = 1.65^\circ$ to $l = 93.4^\circ, b = 1.55^\circ$.

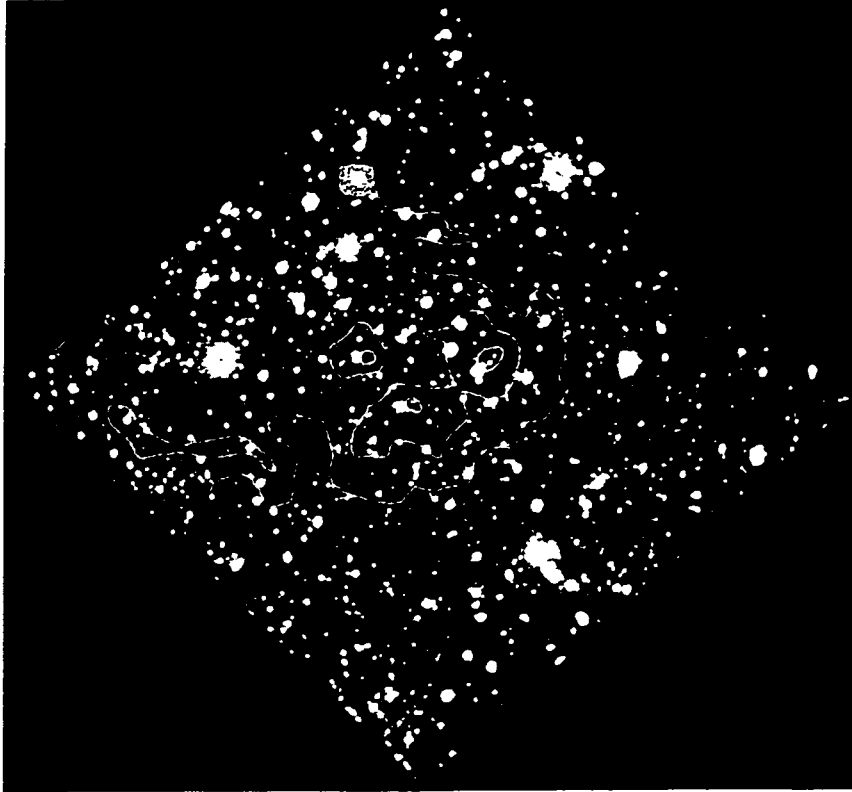


Figure 5.7: Sigma stepped contours (4σ , 5σ , 6σ above the background), overlaid on the original composite $H\alpha + [NII]$ line image. Contours around edge and halo artifacts have been removed. The shape of NRAO 655 is very apparent. North is up, east is left, and the field is $24' \times 24'$.



Figure 5.8: Devon AO $H\alpha + [NII]$ image (656.3nm) on a $53' \times 53'$ DRAO 21cm image of NRAO 655. Dramatically similar morphology in the radio and optical regimes is evident, as both wavelengths show a semi-circular, regular shell of emission. North is up.



Figure 5.9: NRAO 655 at optical and IR wavelengths. The semi-circular shell is again evident in both images, but bright areas of $H\alpha + [NII]$ optical emission correspond to dim areas of dust emission.

$$EM = 2.75 \times \left(\frac{T_e}{10000}\right)^{0.9} I_\alpha e^{(2.2E_{B-V})} cm^{-6} pc \quad \text{eq. 5.3}$$

$$n_e f^{\frac{1}{2}} = \sqrt{\frac{EM}{2R_{HII}}} cm^{-3} \quad \text{eq. 5.4}$$

where I_α is the surface brightness in Rayleighs ($1R = \frac{10^6}{4\pi} photons cm^{-2} s^{-1} sr^{-1}$), R_{HII} is the mean radius of the ionized region ($R_{HII} = 15.3 pc$ at a distance of 8800 pc), T_e is the electron temperature, E_{B-V} the extinction to the ionizing star, and f the fraction of the volume within the HII region occupied by ionized gas. By integrating HI out to $-72 km s^{-1}$ (see sec. 5.5) the optical extinction to NRAO 655 is found to be $A_v = 7.8 mag$, or a reddening of $E_{B-V} = 2.461$ (Sudzhus et al., 1996). Assuming $T_e = 7000 K$ (reasonable, according to Churchwell et al., 1975), we find $EM_{kernel} = 49347 \pm 9439 cm^{-6} pc$. The EM found from the HII-region modelling (see sec. 5.6), which was carried out to fit the 408 MHz and 1420 MHz radio continuum data in the "head" region (Higgs, DRAO export package), is $EM_{head} = 3285 cm^{-6} pc$. Planetary nebula, which are much denser objects, have emission measures on the order of $10^7 cm^{-6} pc$. The intermediate value obtained here is not unreasonable. The rms electron density found for the kernel is $n_e = 40 \pm 4 cm^{-3}$. This is to be compared with the value $n_e = 9 cm^{-3}$, found by integrating the 21cm brightness temperatures within the 4σ contour from the optical image. The same radius, $R_{HII} = 15.3 pc$, was used.

It is probable that the portions of NRAO 655 detected in the $H\alpha + [NII]$ line are those with intrinsically higher EM and n_e values. The apparent discrepancy between the radio continuum and optical values of EM and n_e is thus resolvable.

The mass of emitting $H\alpha + [NII]$ nebulosity is found from the rms electron density and volume of the integrated region to be $1.5 \times 10^4 M_\odot$. For comparison, the mass of the head found from HII-modelling is $1.3 \times 10^4 M_\odot$.

5.4 INTEGRATED FLUXES AND RADIO SPECTRA OF OBJECTS NEAR $l=94^\circ$

Classification of the emission mechanism behind a radio source can be done with surface brightness measurements of it over a range of frequencies. A spectrum is produced, and one can inspect the dependence of flux density S_ν (and hence brightness temperature T_b) on the frequency of observation. At radio wavelengths an optically thick thermal source's flux is proportional to ν^2 , in the Rayleigh-Jeans limit ($h\nu \ll kT$) of blackbody emission:

$$S(\nu) = I(\nu)\tau(\nu) = \frac{2kT}{c^2} \nu^2 \Omega, \quad \text{where } \Omega \equiv \text{solid angle of source} \quad \text{eq. 5.5}$$

In the low frequency regime the optical depth is great, and the dependence of $S(\nu)$ on τ is small, since the body is already opaque. An optically thick thermal source should exhibit a *spectrum* with dependence $S(\nu) \propto \nu^2$. At higher frequencies, $\tau(\nu)$ is decreasing, and the source is becoming optically thin. Since $T \simeq \tau(\nu)T_b$ and $\tau(\nu) \propto \nu^{-2.1}$, a thermal body's flux exhibits little dependence on ν ($S(\nu) \propto \nu^{-0.1}$). Non-thermal radio emission from the synchrotron mechanism tends to have flux density $S(\nu)$ more strongly inversely dependent on frequency, since the intensity depends on the energy spectrum of radiating relativistic electrons. Harwitt (1988) shows this distribution in the

ν (MHz)	Ref.	Resolution (')	$S_{3C434.1}$	$\pm(Jy)$	$S_{NRAO655}$	$\pm(Jy)$
30.9	1	13.0×11.1	99.3	19.9	Invisible	
151	2	1.2×1.5	26.5	1.1	Invisible	
326	3	0.9×1.1	17.7	1.2	6.7	0.5
408	DRAO	3.5×3.8	22.2	1.5	11.6	0.2
1420	DRAO	1.0×1.1	12.8	0.8	11.8	0.1
2695	4,5	4.3	7.8	0.6	8.4	0.1

Table 5.2: Radio data used for spectral index study of J8 field objects 3C434.1 and NRAO 655. References: (1) Kassim, 1988, (2) Vessey et al., 1998, (3) Rengelink et al., 1996, (4) 1990, Reich et al. and (5) 1984, Reich et al.

low frequency radio regime to obey the proportionality $S(\nu) \propto \nu^{-a}$ where we customarily define the *spectral index* of the source as $\alpha = -a$.

High quality 11cm data at a resolution of 4'.3 was obtained from a galactic plane survey at Bonn, Germany. Pre-release data from the seventh Cambridge survey (7C) galactic plane survey of 1998 at 151 MHz was kindly given to us by Dave Green (Mullard Radio AO). 326 MHz data from the Westerbork Northern Sky Survey provided intermediate frequency coverage, and images from the Clark Lake survey at 30.9 MHz provided low frequency data. Other data at 610 MHz and 232 MHz were obtained, but the background noise in these data was high, and the J8 field objects were not seen at all. See Table 5.2 for the frequency range and references.

Point sources superimposed on the field objects were fit and removed in all radio continuum data. Aperture photometry measurements on the sources 3C434.1 and NRAO 655 in at least three different frequencies show different spectra. Table 5.2 presents flux densities obtained from these measurements, and Figure 5.10 shows the objects' radio spectra. 3C434.1 emits in a distinctly non-thermal way, while the spectrum of NRAO 655 shows the expected index of $\alpha = -0.1$ within error. The author finds NRAO 655 invisible at lower frequencies, such as the high-resolution (1') 7C survey at 151 MHz. The Westerbork synthesis telescope data did not have complete (u,v) plane coverage (missing low spatial frequencies), thus, flux densities were lower than expected at 326 MHz.

The spectrum of NRAO 655 identifies it as an HII region; a hot cloud of ionized hydrogen emitting thermally. The flatness of this spectrum suggests NRAO 655 is optically thin at radio wavelengths, suggesting a lower than usual electron density for this nebula. The region's 1420 MHz flux density ($S_{1420} = 11.8 \pm 0.1$) is inconsistent with that of Pauliny-Toth et al. (1966) who obtained a substantially lower value at 1400 MHz ($S_{1400} = 6.4 \pm 0.6$).

Previous classifications of 3C434.1 as a shell type SNR appear correct, and our value for 1420 MHz flux density of $S_{1420} = 12.8 \pm 0.08 Jy$ is consistent with Landecker's (1985; $S_{1420} = 16 \pm 3 Jy$), and Pauliny-Toth's (1966; $S_{1400} = 12.0 \pm 1.5 Jy$). A spectral index of $\alpha = 0.54 \pm 0.08$ is consistent with Mantovani's value $\alpha = 0.46 \pm 0.03$ (1985), and is typical of a shell type supernova remnant.

Integrated Radio Spectra of J8 Field Sources

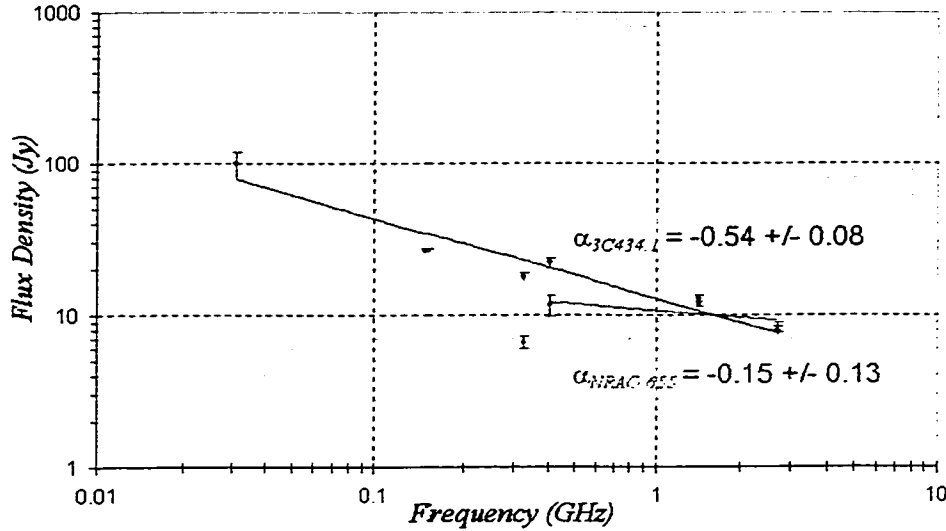


Figure 5.10: Radio spectra of 3C434.1 and NRAO 655.

Maps of the spectral-index (SI) variation across the source were constructed by the author using a method detailed by Zhang et al., 1997. The maps clearly show different average indices for the SNR and HII region, and the emission between them appears to show an index similar to that of the SNR, as noted by Landecker et al, 1985. Some variation in the spectral indices exists across the face of each object. In all SI maps derived with pairs of continuum wavelengths, 3C434.1 appears to have a kidney bean shaped region of low index ($\alpha = -0.2$) near its centre, oriented NS (Figure 5.11). It is interesting to note that this feature's position and orientation is similar to the NS band of absorption noted in the optical image. The low SI in the remnant's centre may be the result of thermal contamination from a foreground source which absorbs optical emission. From the centre, the SI steadily increases towards the east, peaking at the probable location of the shock with $\alpha \sim -0.6$. This behavior is found in other supernova remnants (e.g. G78.2+2.1, Zhang et al., 1997). Theoretical reasons for spectral-index variations across remnants have been suggested but no clear interpretation of this apparent spectral steepening near the shock front has been found. There is no clear correlation of spectral index with intensity across the SNR. NRAO 655's spectral index displays a constant thermal signature within the head.

While no significant dust emission is present at the location of 3C434.1 ($l=94.0$, $b=1.0$), emission is visible in all four IRAS images at $l=93.4$, $b=1.8$,

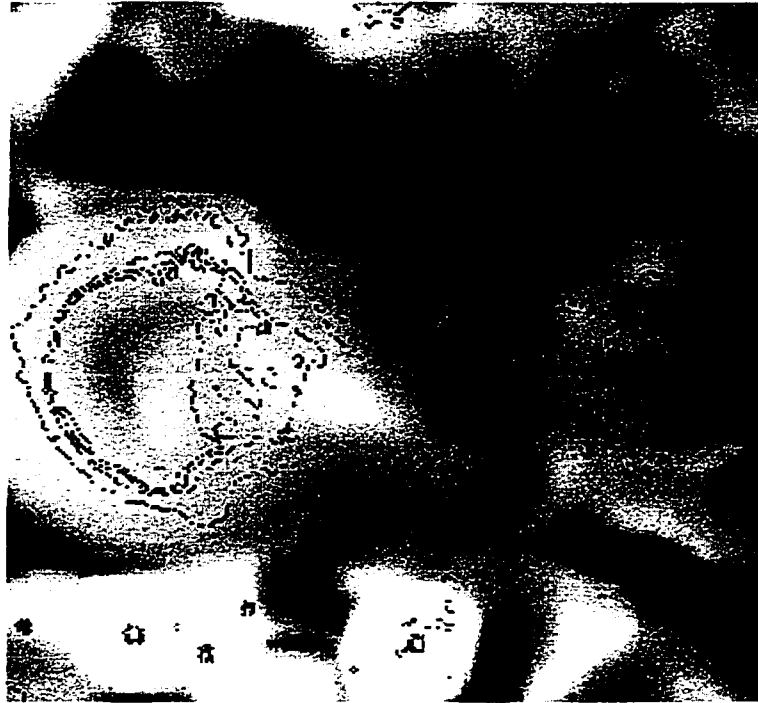


Figure 5.11: Spectral index map of 3C434.1 and NRAO 655, calculated with radio continuum 11cm and 74 cm maps. The 21cm continuum contours are overlaid. Note the distinctly lower average index of NRAO 655, indicative of thermal emission. The westerly extension from 3C434.1 appears to have a high index, similar to the shell itself. The greyscale runs from index $\alpha = 0.7$ (dark) to $\alpha = -1.1$ (light).

Wavelength (μm)	Bandwidth (μm)	Integrated flux density (Jy)	Integrated flux ($\times 10^{-11} W m^{-2}$)
0.656	0.0075	4.79 ± 0.92	0.025 ± 0.005
12	6.5	97 ± 5	0.019 ± 0.001
25	11	107 ± 6	0.035 ± 0.002
60	40	1013 ± 55	1.22 ± 0.07
100	37	3263 ± 284	3.62 ± 0.32

Table 5.3: Infrared and optical flux densities and fluxes for NRAO 655, as derived from IRAS (www.ipac.caltech.edu/ipac/iras/iras.html) and Devon AO observations. A strong IR point source at ($l=93.37$, $b=1.82$) is visible at 12 and 25 microns within the “head” of NRAO 655. This was individually measured and its flux density removed.

the location of NRAO 655 (see Figure 5.6). Table 5.3 shows the HII region’s integrated flux density in all four IRAS wavelengths, as well as the integrated $H\alpha + [NII]$ ($0.656\mu m$) flux density, derived from optical observations (Chapter 4). In $H\alpha + [NII]$ emission line, NRAO 655 has a very similar overall semi-circular shape, of similar extent (diameter $14'$) as the IR object (diameter $18'$).

5.5 LINE EMISSION FROM HII, HI AND H₂ SURROUNDING NRAO 655 AND 3C434.1

Objects within the CGPS J8 field have previously been catalogued, but no distances have been ascribed to them firmly. Mantovani et al. (1982) found Σ -d-z distances for 3C434.1 and the incorrectly classified NRAO 655. However, the intrinsic unreliability of Σ -d-z distance estimates was concluded by Green et al. 1984, making the only distance estimates for objects in this region unreliable. In this study, new distances are derived through direct observations of atomic, molecular, and recombining hydrogen.

Suggestion of a molecular hydrogen shell surrounding the western edge of NRAO 655 comes from observations at 115.271 GHz ($\lambda = 2.6mm$) of the ^{12}CO $J = 1 \rightarrow 0$ transition. CO is considered a tracer of molecular hydrogen in interstellar clouds (Rohlfs, 1986, p. 289). The CO data used in this study come from the 1.2m CfA survey (Dame et al., 1987) and have a low angular resolution ($FWHM = 8.7'$). They are the only such observations available near $l = 94^\circ$, and are available only below $b = 2^\circ$.

The brightest ^{12}CO emission ($T_b = 0.809K$ peak near $-72 km s^{-1}$) coincides with the steep western edge of the continuum emission from the kernel. CO emission from $v = -68 km s^{-1}$ to $v = -77 km s^{-1}$ appears to consist of discrete concentrations of brightness, and the position of the peak CO emission changes from channel to channel (spaced by $1.3 km s^{-1}$). As velocity becomes less negative, the position of peak CO brightness moves generally clockwise around the periphery of the head of NRAO 655. CO integrated over a velocity interval of

13 km s^{-1} forms a rough crescent around the west side of the head of NRAO 655, as shown in Figure 5.12. A molecular cloud thus surrounds the western edge of the ionized material of NRAO 655, presumably the edge of where molecular dissociation of H_2 can occur. The central velocity of this cloud is -71.5 km s^{-1} .

Also seen in Figure 5.12 is the integration of six HI 21cm-line emission images. The individual HI images have been interpolated onto a velocity grid of 2.6 km s^{-1} so that the six images span 13 km s^{-1} . A local minimum in HI emission is seen to coincide with the continuum-emission kernel of NRAO 655. This cavity's western edge is seen wrapped with a shell of HI emission. The angular size of this minimum does not vary in a regular manner from channel to channel, as might have been expected if it were caused by an expanding shell of atomic gas. Instead, the contours of continuum emission complement the 21cm-line HI brightness quite well in the middle of the velocity range portrayed, and less well at the ends. The middle of this velocity range is -71.5 km s^{-1} . On this basis, it is concluded that there is a cavity in the HI which matches the position and angular size of the kernel of NRAO 655, and that the velocity of this HI cavity is approximately -71.5 km s^{-1} .

Worthy of note is the layered appearance of hydrogen on the western rim of NRAO 655 (Figure 5.13). Emission from HII within the kernel peaks about 6 arcminutes West of the head's centre, and drops sharply thereafter. This peak of HII (the kernel) corresponds to a minimum of emission from HI and marks the location of the cavity, and presumably the ionizing star or stars powering the nebula. About 5 arcminutes from the kernel, HI emission peaks, showing the location of the atomic hydrogen shell surrounding the cavity on the western edge. Here the flux of ionizing photons ($\lambda < 91.2\text{ nm}$) from the central star diminishes, but lower energy photons are still present and dissociating H_2 molecules. The point where the low energy photon flux is no longer sufficient for dissociation is reached 7 arcminutes from the kernel, where CO emission, and hence the density of H_2 , peaks.

Both the atomic and molecular hydrogen seen associated with NRAO 655 are visible near -72 km s^{-1} . Using a flat galactic rotation model with the solar galactocentric distance $R_0 = 8.5\text{ kpc}$ and orbital velocity $v_0 = 220\text{ km s}^{-1}$, the kinematic distance that can be assigned to NRAO 655 is 8.8 kpc. This places it on the far edge of the Perseus spiral arm, whose mean kinematic distance (at $l = 94^\circ$) is 8.3 kpc (see Figure 5.14). The linear size of NRAO 655 is thus $107\text{ pc} \times 67\text{ pc}$.

To convert the contour map of brightness temperature of ^{12}CO emission from the molecular cloud in Figure 5.12 to the mass of H_2 in the cloud, we use the relation:

$$N_{\text{H}_2} = 2.3 \times 10^{20} \int T_b dv \text{ (cm}^{-2}\text{)} \quad \text{eq. 5.5}$$

where v is velocity in km s^{-1} , and T_b is ^{12}CO brightness temperature in K (Strong et al., 1988). Figure 5.12 shows T_b integrated over a velocity interval of 13 km s^{-1} and we find:

$$\int \int T_b dv d\Omega = 2.04 \times 10^{-3} \text{ K km s}^{-1} \text{ sr} \quad \text{eq. 5.6}$$

Using a distance of 8.8 kpc, we find a total mass of H_2 in the cloud of $58000 M_\odot$. This is a lower limit, since the molecular cloud may extend higher in b

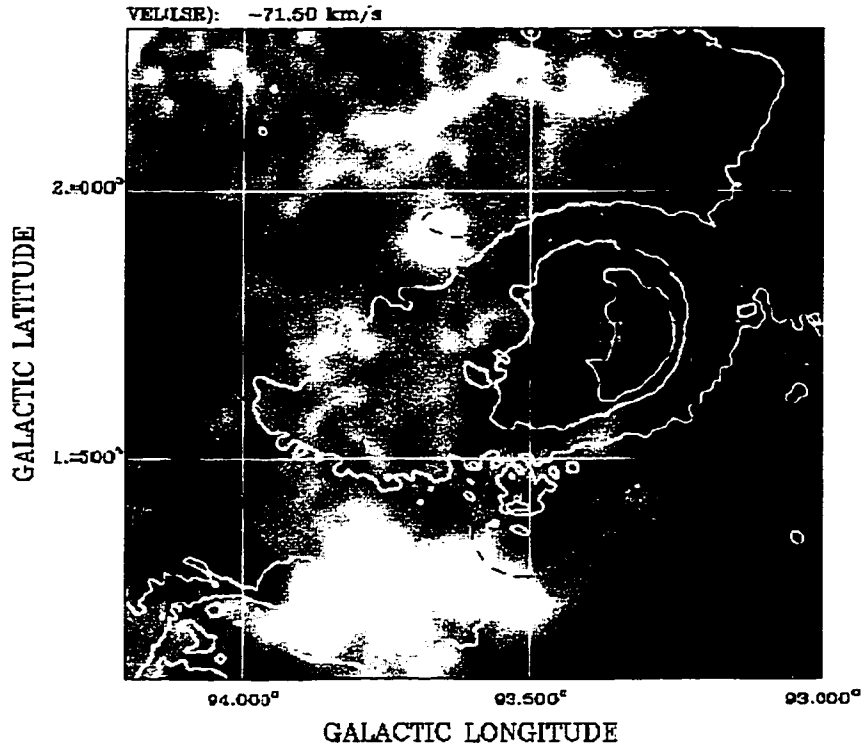


Figure 5.12: Atomic and molecular hydrogen shells surrounding the kernel of NRAO 65.5. Both the HI emission (grayscale map) and the CO emission (dotted contour lines) have been integrated over a 13 km s^{-1} velocity interval centred on -71.5 km s^{-1} . White lines are 1.4 GHz continuum emission contours (1.5K, 3K and 5K of brightness temperature) from NRAO 655. The velocity-integrated CO contours ($13, 26, \text{ and } 39 \text{ K km s}^{-1}$ of $\int T_b dv$) appear to wrap around the head of NRAO 655 in the form of a crescent, and the cavity in the velocity-integrated HI emission coincides well in position and shape with the kernel of NRAO 655. The mean has been subtracted from this image, and the greyscale runs linearly from $T_b = -130 \text{ K km s}^{-1}$ (dark) to $T_b = +195 \text{ K km s}^{-1}$ (light).

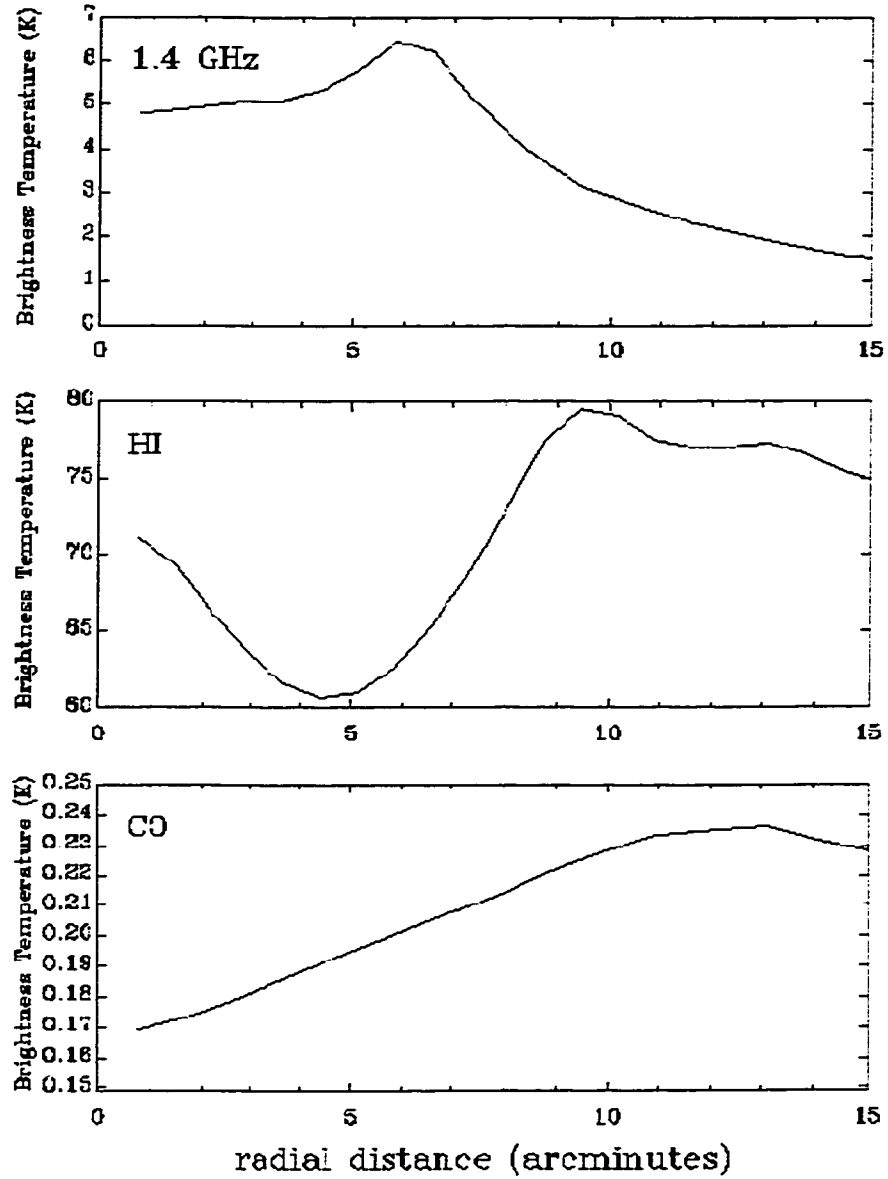


Figure 5.13: Radial profiles from NRAO 655's centre towards the western rim, showing the layered appearance of hydrogen.

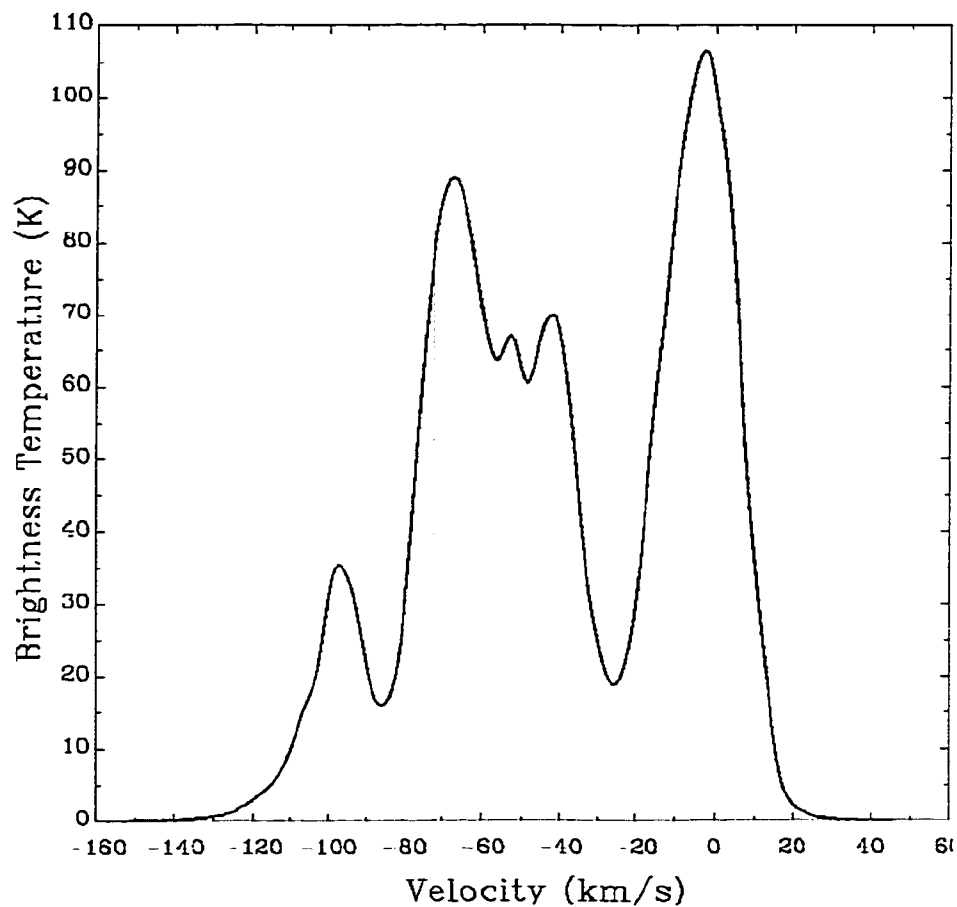


Figure 5.14: The average HI T_b spectrum for $l = 94^\circ$ over a region of diameter $40'$. The vertical line at -72 km s^{-1} shows the central velocity of HI and CO emission associated with NRAO 655. Visible is nearby gas in the local spiral arm, which peaks near 2 km s^{-1} . The Perseus spiral arm is visible at -68 km s^{-1} (8.3 kpc), and the outer spiral arm near -100 km s^{-1} (12.6 kpc).

than shown in Figure 5.12.

To find the mass of the partial HI shell flanking the western edge of NRAO 655, a similar integration is performed (Rohlfs, 1986, eq. 11.18):

$$N_H \cong 1.82 \times 10^{18} \int_v^{v+dv} T_b dv \text{ (cm}^{-2}\text{)} \quad \text{eq. 5.7}$$

With $dv = \Delta v = 13 \text{ km s}^{-1}$, and a distance of 8.8 kpc, a mass of $5100 M_\odot$ is found.

Supportive evidence for NRAO 655's distance and identity as an HII region was gathered with observations of hydrogen recombination line radiation. If NRAO 655 was a supernova remnant as suggested by previous authors, one would not expect to see recombination line emission from it. A search for $H158\alpha$ emission (rest frequency $\nu = 1651.541$ MHz) resulted in a successful detection: a broad line emerged 10.6σ above the noise (see Figure 4.4, Chapter 4). The non-flat baseline, atop which was this recombination signal, was removed from the data by subtracting a 3rd order polynomial fit, which was fit after giving velocities -119 km s^{-1} to -29 km s^{-1} zero weight. After this baseline removal, a Gaussian fit resulted with the observed central velocity $v = -71.8 \pm 4 \text{ km s}^{-1}$, and observed line width $FWHM = 41 \text{ km s}^{-1}$. This is the first detection of recombination line emission from this nebula. Using the same flat rotation model as above with constants $R_0 = 8.5 \text{ kpc}$ and $v_0 = 220 \text{ km s}^{-1}$ confirms the distance to NRAO 655 as $8.8 \pm 1.2 \text{ kpc}$.

The brightness temperature scale is uncalibrated for observations at this frequency with the 26m radio telescope. Thus, an electron temperature could not be derived from the recombination line results. From purely thermal electron motions, the $H158\alpha$ recombination line should be of Gaussian shape with full width $\Delta v \approx 19 \text{ km s}^{-1}$ (Rohlfs, p. 253), assuming an electron temperature of 8000K (see next paragraph). The observed line width ($\Delta v_{obs} = 41 \text{ km s}^{-1}$) can be used to estimate the non-thermal motion within the gas, or "micro-turbulence" (Rohlfs, p. 253):

$$\Delta v = \frac{2\nu_{ik}}{c} \left(\left(\frac{2kT_e}{M_{proton}} + v_t^2 \right) \ln 2 \right)^{\frac{1}{2}} \quad \text{eq. 5.9}$$

where $\nu_{ik} = 1651.541 \text{ MHz}$ for the transition $k = 159 \rightarrow i = 158$, and v_t is the velocity width due to non-thermal motions. For NRAO 655, $v_t = 22 \text{ km s}^{-1}$, or similar to the thermal contributions. The gas in NRAO 655 is probably quite turbulent.

A galactic temperature gradient for HII regions was derived by Shaver et al., 1983:

$$T_e(K) = (3150 \pm 110K) + 433 \pm 40(K \text{ kpc}^{-1}) \times R_G(\text{kpc}) \quad \text{eq. 5.8}$$

The heliocentric distance of 8.85 kpc translates into a galactocentric distance of roughly 12.7 kpc, which in turn implies an electron temperature of $T_e \approx 8500 \pm 1100K$ for the HII region. This is of similar order to the adopted value in the HII region modelling (7000K, next section).

Component	Head	Body	Tail	Halo	Totals
Type	Thick walled hemisphere	Thick walled cylinder	Filled ellipsoid	Thick walled ellipsoid	
$n_e (cm^{-3})$	8.5	8.5	5	2.6	
S (Jy) 1.42 GHz	4.7	3.1	1.7	2.2	11.6
{408 MHz}	{5.2}	{3.5}	{2.0}	{2.5}	13.2
EM ($cm^{-6}pc$)	3285	2316	845	362	
Mass (M_\odot)	13000	10900	7700	19000	50600
U ($cm^{-2}pc$)	90.0				
Stellar Type Required (ZAMS)	O5.8				
Number of B0 Stars	134				134

Table 5.4: The four-component model of NRAO 655.

5.6 A MODEL FOR NRAO 655

1.42 GHz and 408 MHz radio continuum images are used to produce a geometric model of NRAO 655 using the program “HIIMODEL” (DRAO export package, Higgs, 2000). The model begins with assumptions of electron densities and temperatures and the variation of each. Helium abundance, ionization, and distance are also input. The program computes one or more brightness-temperature distributions (which may be output as maps), the total flux density and mass, the maximum brightness temperature and emission measure ($cm^{-6}pc$), and the required excitation parameter ($cm^{-2}pc$). From this information, one can derive the single stellar type required to ionize that component, or the equivalent number of early type stars required.

Assumed model input parameters are shown in Table 5.4, along with results. NRAO 655 is broken down into a four- component model, each of which is modelled separately at 1.42 GHz and 408 MHz. All components have dimensions matching those observed, and are modelled with electron temperatures of $T_e = 7000K$, helium abundances of 9%, at a distance of 8500 pc. There are two constraints on the output model: 1) the sum of the component’s individual flux densities must match the observed total flux density of NRAO 655 at each frequency, and 2) the brightness temperature variation across each component and the maximum T_b should closely match the observed T_b distribution and maximum at each frequency.

It is assumed that the exciting star(s) are located within the head of NRAO 655. If a single star is responsible for the ionization of the head, it must be of spectral type O5-O6 zero-age main sequence (ZAMS). Such a star, at a distance of 8900 pc, would shine at magnitude $m_V = 16.7$ (including 7.8 magnitudes of optical extinction). This star is likely to be visible in the optical ($H\alpha + [NII]$) image (Chapter 4, Figure 4.5), as this image, by comparison with the Palomar Observatory Sky Survey plates (limiting magnitude 18-19), shows stars down to near 20th magnitude. A cluster of B0 stars will be nearer the limit of detection,

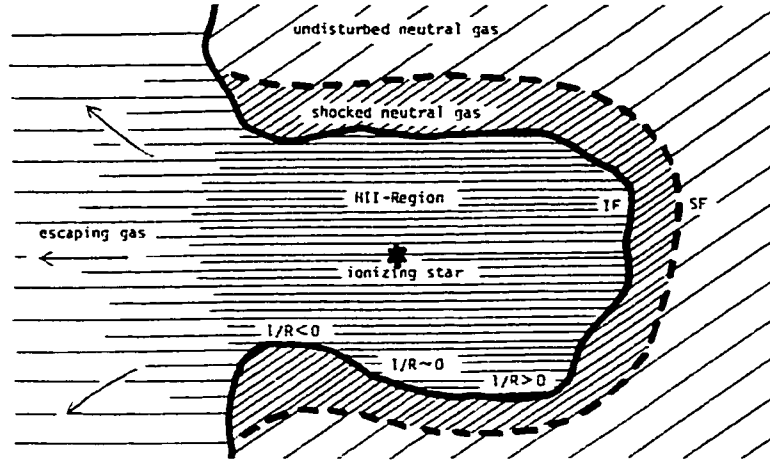


Figure 5.15: A scenario similar to the observed structure of NRAO 655 today. An O-star forms inside a molecular cloud, and erodes and ionizes a cavity near the edge. Ionized gas breaks out of the side into the less dense surroundings, while the ionization front (IF) inside advances towards the center of the cloud. R is defined as the radius of curvature for the IF with respect to the ionized gas, and three configurations ($R^{-1} > 0$, $R^{-1} \sim 0$, and $R^{-1} < 0$) are defined by Whitworth, 1979.

at $m_V = 18.5$ for each individual.

A single O-star, forming within the interior and near the edge of an extended massive molecular cloud will evolve an ionized region similar to what is observed for NRAO 655. An O-star will erode a cavity in the interior side of its parent molecular cloud, creating an ionization front on the inside, and a hole through which ionized gas can escape to the outside of the molecular cloud (Figure 5.15, from Whitworth, 1979). Comparing this to Figure 5.12, the neutral hydrogen shell observed on the western edge of the kernel would thus be the radiation-bounded region, and this dense HI would lie between the shock front and the ionization front. Ionized gas escapes through the eroded edge of the birth cloud towards the east when the IF reaches the inside edge.

Another, similar model that explains well the observed form of NRAO 655 is the Champagne Model (Tenorio-Tagle, 1979, and Franco et al., 1990). The model begins with a ZAMS O-star and its initial Stromgren sphere placed inside, and near the edge of a dense cloud of HI or H_2 . This cloud has a core of constant density n_c , radius r_c , and an envelope (inter-cloud medium, or ICM) with a power law density structure (eq. 5.9):

$$\begin{aligned}
 n(r) &= n_c, \text{ for } r \leq r_c \\
 n(r) &= n_c \left(\frac{r}{r_c} \right)^{-w}, \text{ for } r > r_c
 \end{aligned}
 \tag{eq. 5.9}$$

See Figure 5.16 for a graphical explanation of evolutionary phases of this model. The ionization front advances towards the inside edge of the cloud,

and will rush into the decreasing density envelope. The pressure gradient at the boundary sets up a strong shock that propagates into the ICM, while a rarefaction wave moves towards the star. Ionized material flowing into the ICM behind the shock spreads and forms an observable nebula. For the champagne phase to occur, the exponent in the power law governing the density of the ICM must be $w > 1.5$.

This model is likely to be very applicable to NRAO 655. The tail (where we believe ionized gas has spilled out into the ICM) already shows a mild power law density profile (Figure 5.5). It is reasonable to assume that a stronger power law existed prior to the champagne flow. The large size of NRAO 655 argues against large initial density gradients (large values of w) so the nebula is probably in what Franco et al. call the “slow regime” ($\frac{3}{2} \leq w \leq 3$). In this regime, the radius of the ionized core evolves as:

$$r(t) \simeq r_c + \left[1 + \left(\frac{3}{3-w} \right)^{\frac{1}{2}} \right] c_i t$$

where c_i is the speed of sound in the ionized gas. Estimates with reasonable assumptions of w , measurements of NRAO 655’s current ionized radius ($r(t) = 34pc$), and estimates of its initial ionized core radius ($r_c \sim 15pc$) lead to an age estimate of $t \sim (3 - 5.2) \times 10^5 yr$. This is consistent with the typical core hydrogen burning lifetime of B0 stars ($3 - 4 \times 10^6 yr$).

5.7 EVIDENCE OF INTERACTION AND A COMMON ISM FOR OBJECTS NEAR $l=94^\circ$

The possibility of an environment dynamically shared by NRAO 655 and 3C434.1 is first raised upon inspecting radio continuum images of the region near $l = 94^\circ$. The DRAO radio continuum 21cm and 74 cm observations have produced high resolution images with features suggestive of interstellar links between such objects in this region. Such features include haloes enveloping SNR/HII region pairs, and bridges of emitting material between individual objects and between groups. Evidence for interaction between SNRs and HII regions is in the form of extensions, or blowouts, into common areas between the objects. Such interaction of SNRs and HII regions is expected. The SNRs’ progenitor stars, being massive, are necessarily very young. Thus they explode as supernovae while other stars in the neighbourhood are still in their early evolutionary phases and are likely to be surrounded by HII regions. This study has produced evidence to support this possibility.

Emission between the two objects is distinctly seen in radio continuum maps at $\lambda = 21cm$ and $\lambda = 11cm$, and is weakly apparent at $\lambda = 74cm$. Emission extending from 3C434.1 towards NRAO 655 appears to be non-thermal in origin, and is apparent in spectral index maps of the region. This emission probably originates with the SNR. Thermal emission extends some 40’ from NRAO 655 towards the north-east, in an anti-parallel direction to the SNR’s extension. As discussed in the previous section, this is possibly an occurrence of a “champagne flow”, suggesting that NRAO 655 formed near the inside edge of its parent

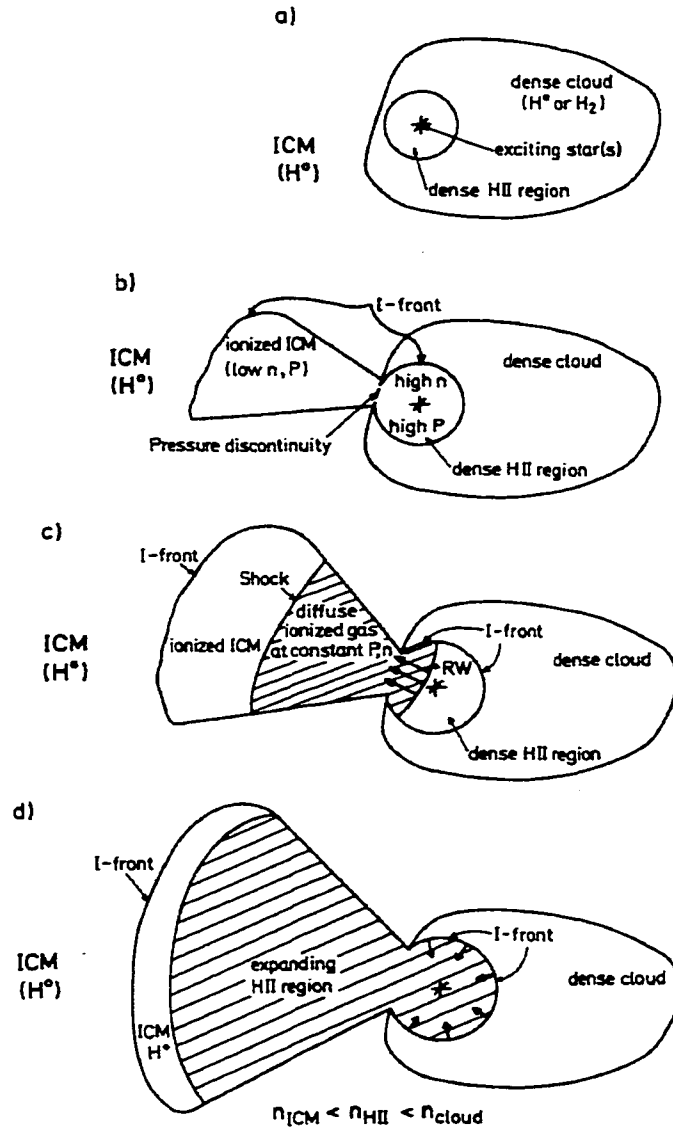


Figure 5.16: Evolution of a dense HII region as it breaks through the edge of its parent cloud, and “champagne flows” into the surrounding ICM. From Tenorio-Tagle, 1979.

molecular cloud. It is possible that both the SNR and HII region are responding to or interacting with the same lower density medium between them.

The strongest evidence backing the shared environment hypothesis is the common distance to both objects, as evidenced by atomic hydrogen emission line data. A very distinct shell of HI is found at $v = -72 \text{ km s}^{-1}$, wrapping fully 180° around the eastern rim of 3C434.1, from the northern edge to the southern edge of the remnant. The semi-circular HI neatly contains the entire eastern rim of the remnant, and the shell's 29' inside diameter matches the 29' circle that best describes the continuum appearance of 3C434.1. At a kinematic distance of 8.8 kpc, the shell and remnant are 75 pc in diameter. The shell on the eastern side is most likely HI swept-up by the expanding shock. No swept-up material is visible across the western half of the remnant.

The SNR/HII region pair and their neighboring objects are seen to exist within a very large halo of weak emission (Figure 5.17). This observational evidence, along with similar distances and areas into which flows are occurring point to a likely shared environment between 3C434.1 and NRAO 655.

5.8 REFERENCES

- Arendt, R. G., 1989, Ap JS 70, 181.
- Caswell, J.L., 1970, A&A 7, 59.
- Churchwell E. and Walmsley C.M., 1975, A&A 38, 451.
- Dame T. M., Ungerechts H., Cohen R. S., de Geus E. J., Grenier I. A., May J., Murphy D. C., Nyman L., and Thaddeus P., 1987, ApJ 322, 706.
- Fich, M., 1983, Ph.D. Thesis, University of California, Berkeley.
- Fich, M., 1986, AJ 92, 787.
- Franco J., Tenorio-Tagle G., and Bodenheimer P., 1990, ApJ 349, 126.
- Galt J.A., and Kennedy J.E.D., 1968, AJ 73, 135.
- Goss W., Mantovani F., Salter C.J., Tomasi P., and Velusamy T., 1984, A&A 138, 469.
- Green, D. A., 1984, MNRAS 209, 449.
- Harwit, Martin. Astrophysical Concepts (Second Edition), Springer-Verlag, New York, 1988.

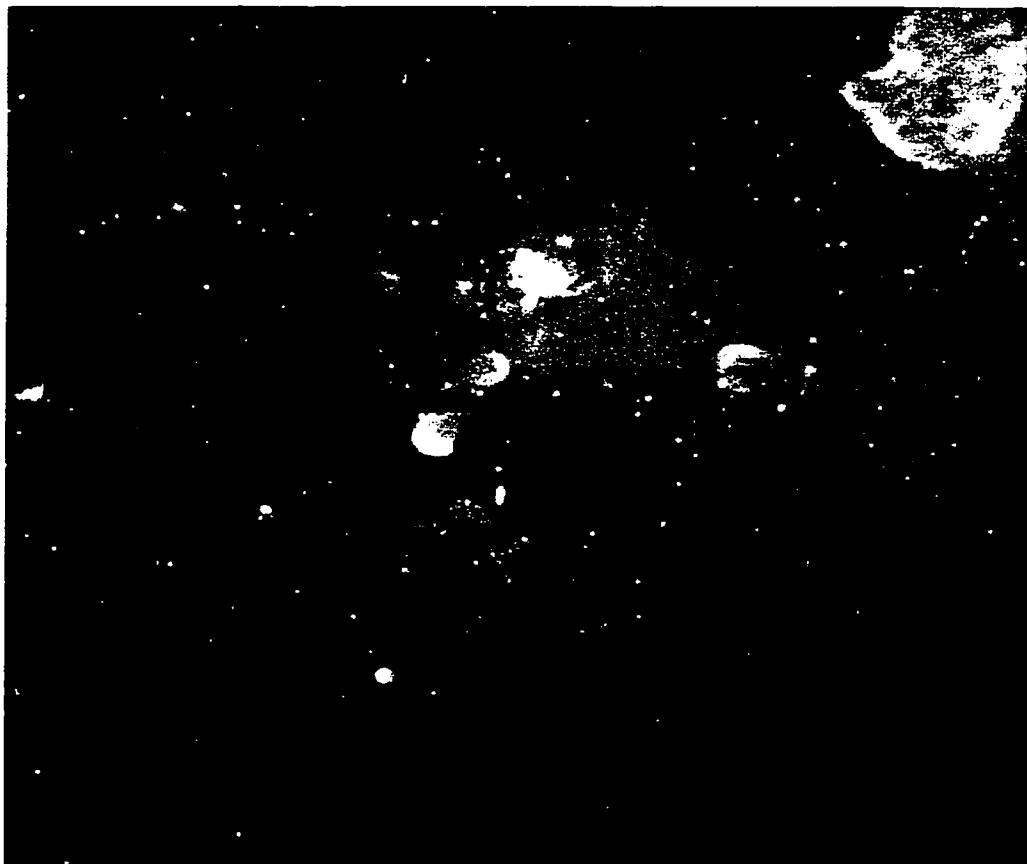


Figure 5.17: The galactic environment from $l = 88^\circ, b = -3.5^\circ$ (lower right) to $l = 98^\circ, b = +5.5^\circ$ (upper left), centred on $l = 93.12^\circ, b = 1.005^\circ$ (near NRAO 655). Many more objects are visible than are listed in Table 5.1. The large region surrounding 3C434.1 and NRAO 655 is enveloped in a halo of weak continuum emission, suggestive of an interstellar medium shared by these objects. Map derived from a CGPS continuum super-mosaic at $\lambda = 21cm$.

- Higgs, L. A., 2000 DRAO export package.
- Kallas E., and Reich W., 1980, A&AS 42, 227.
- Kassim, N. E., 1988, ApJS 68, 715.
- Landecker T. L., Higgs L. A., and Roger R. S., 1985, AJ 90, no. 6, 1082.
- Landecker T.L., Zheng Y., Zhang X., and Higgs L.A., 1997, A&AS 123, 199.
- Mantovani F., Nanni M., Salter C. and Tomasi P., 1982, A&A 105, 176.
- Miralles M.P., Rodriguez L.F., and Scalise E., 1994, ApJS 92, 173.
- Molinari S., Brand J., Cesaroni R., and Palla F., 1996, A&A 308, 573.
- Parker R., Gull T., and Kirschner R., An Emission Line Survey of the Milky Way, NASA, 1979.
- Pauliny-Toth I.I.K., Wade C.M., and Heeschen D.S., 1966, ApJS 13, 65.
- Reich W., Furster E., Haslam C. G. T., Steffen P., and Reif K., 1984, A&AS 58, 197.
- Reich W., Furster E., Reich P., and Reif K., 1990, A&AS 85, 633.
- Rengelink R.B., Tang Y., de Bruyn A.G., Miley G.K., Bremer M.N., Rottgering H.J.A., and Bremer M.A.R., 1997, A&AS 124, 259.
- Reynolds, R.J., 1988, ApJ 333, 341.
- Rohlfs, Kristen. Tools of Radio Astronomy, Springer-Verlag, New York, 1986.
- Shaver P.A., McGee R.X., Newton L.M., Danks A.C., Pottasch S.R., 1983, MNRAS 204, 53.
- Strong A. W., Bloemen J. B. G. M., Dame T. M., Grenier I. A., Hermsen W., Lebrun F., Nyman L.-A., Pollock A. M. T., and Thaddeus P., 1988, A&A 207, 1.
- Sudzius J., Bobinas V., and Raudeliunas S., 1996, Baltic Astronomy 5, 485.
- Tenorio-Tagle, G., 1979, A&A 71, 59.
- Vessey S.J., and Green D.A., 1998, MNRAS 294, 607.

- Velusamy T., and Kundu M.R., 1974, A&A 32, 375.
- van der Werf P., and Higgs L.A., 1990, A&A 235, 407.
- van der Werf P., and Higgs L.A., 1991, A&AS 89, 599.
- Willis, A.G., 1973, A&A 26, 237.
- Whitworth, A., 1979, MNRAS 186, 59.
- Wouterloot J.G.A., and Brand J., 1989, A&AS 80, 149.
- Zhang X., Zheng Y., Landecker T.L., and Higgs L.A., 1997, A&A 324, 641.

Chapter 6

THE FUTURE FOR THE DEVON ASTRONOMICAL OBSERVATORY

6.1 THE POSSIBILITIES

The discovery of optical emission from NRAO 655 foretells a future of possible similar achievements at the Devon Astronomical Observatory. Enormous potential astrophysics is waiting to be done on HII regions and supernova remnants, especially in conjunction with the high resolution radio images being produced by DRAO. For example, Winkler et al. (1993) find that optical luminosities have been measured for very few galactic SNRs, of which there are at least two within an area of 6 square degrees centred on $l = 94^\circ, b = 0.0^\circ$.

As seen in this study, optical emission line identification of HII regions can provide quantities for the emission measure, electron density, and mass of ionized material, quantities that can be compared to those derived from radio maps. The excellent selection of interference filters at Devon allow abundances of S^+ , N^+ , and O^{++} to be derived for HII regions and supernova remnants from $[SII]/H\alpha$, $[NII]/H\alpha$, and $[OIII]/H\alpha$ line ratios, respectively (Hunter, 1992). Identification of strong $[SII]$ and $[NII]$ lines in a remnant is characteristic of shock-heated material (Dopita et al., 1984). The ratio of $[OIII]/H\beta$ characterizes the excitation parameter of an HII region, which correlates to the effective temperature of the exciting star (Hunter, 1992). Finally, construction of HR diagrams with faint stars and clusters can potentially serve to identify the ionizing star(s) associated with HII regions, and the necessary multi-colour photometric capabilities exist at the Devon AO.

Table 6.1 lists the catalogued sources in the $l = 94^\circ$ area and the optical identifications achieved to date, as well as whether emission can be seen in the red Palomar Observatory Sky Survey (limiting stellar magnitude 18-19). This area is extremely interesting, as the number of astronomical sources within it is large and as yet, little more than catalogued. Most have not been optically identified, and no significant field nebulosity is visible in the POSS scans either. Surprisingly, emission near CTB 102 is seen, but has not been studied or

Object	Type	Emission and Absorption Features in POSS-I Scans	Identification
CTB 102, KR1	HII	Large scattered patches of faint emission, brightest at: $\alpha = 21^h 12^m, \delta = 52^{\circ} 27'$	
WB 43, Mol 133	HII	None	
KR6		None	
KR4		None	
NRAO 652	HII	None	
G92.3+1.5		None	
WB 93, Mol 135	HII	None	
CTB 104A	SNR	None	
NRAO 655	HII	None	1999, this study
3C434.1	SNR	None	1999, this study
BG 2107+49	HII Complex	Dark absorption features at low level; no emission.	Higgs et al., 1987

Table 6.1: Previous optical identifications of sources surrounding $l = 94^{\circ}$, and the appearance of emission and absorption features near them. Only BG2107+49 has been optically identified in a 1983 red (700nm) CCD image from an extended study by Higgs et al., 1987. Faint optical emission features are seen near CTB 102 in the Digitized Sky Survey POSS plate scans, but studies of these have not been published by any author. Coordinates given are J2000.

confirmed in any publication to date.

The Devon AO can produce useful maps for optical studies of objects found in the CGPS data. High resolution mosaics, assembled from CGPS fields of the $l = 94^{\circ}$ area and objects, are available as 21cm and 74cm radio continuum maps, and would be complemented with similar optical emission line mosaics. The necessary software for construction of mosaics from Devon AO fields exists, and the techniques have been tried (Cartledge, 1996). Emission line $H\alpha + [NII]$ observations of the “galactic mushroom” (English et al., 2000), at the request of J. English (STScI) and A. R. Taylor (University of Calgary) will begin this fall to augment its discovery image in the CGPS HI data.

The author feels strongly that the possibilities of the Devon AO system are just now beginning to be explored, and that optical data from this observatory can augment radio data from DRAO, and facilitate the CGPS in fulfillment of its primary goal; understanding our origins, ultimately from diffuse gas and dust in the interstellar medium of our Galaxy.

6.2 PROJECT SUMMARY STATEMENT

This work has combined optical, radio and infrared astronomical data together for a comprehensive look at two galactic objects. This was the original intention behind the design and construction of the DevonAO CCD system, a project that brought optical and radio astronomers on the University of Alberta and The King's University College campuses together. The project is arguably a successful one. The system's noise and performance specifications have been characterized, and struggles with optical artifacts (e.g. ghosting), high dark count, and RFI contamination have been overcome. The new software developed for the project efficiently allows the observer to collect excellent CCD data, while maintaining attention to its quality. Observing and reduction techniques for imaging faint objects, and collecting precision photometric data have been developed, and are now routine to use. Emission line observations of faint extended objects at the Devon AO is also proven to produce convincing detections, and that useful astrophysical information can come from these observations. The design phase of the project is over, and the exciting and diverse astrophysical science in waiting can begin.

6.3 REFERENCES

Cartledge, S., 1996, M.Sc. Thesis, University of Alberta.

Dopita M.A., Binette L., D'Odorico S., and Benvenuti P., 1984, ApJ 276, 653.

English J., Taylor A.R., Mashchenko S.Y., Irwin J.A., Basu S., and Johnstone D., 2000, ApJ Letters 533, 25.

Higgs L.A., Vallee J.P., Albinson J.S., Batrla W., and Goss W.M., 1987, A&A 181, 351.

Hunter, D., 1992, ApJS 79, 469.

Winkler P.F., Olinger T.M., Westerbeke S.A., 1993, ApJ 405, 608.

Appendix A

PROCESSING OF 21CM AND 74 CM DRAO ST CONTINUUM IMAGES

Herein one will find a comprehensive recipe for processing raw aperture synthesis data as it comes from the DRAO ST. The software used is L. Higgs' LINUX export of the DRAO software. Some packages (e.g. CLEAN, PH2) need at least 300 megabytes of virtual memory (swap + physical RAM). As well, a very fast processor is needed for the inevitable experimentation with the packages. I used a PC equipped with a PII-400 MHz CPU, 128M RAM, 300M virtual memory, and the new Linux kernel (2.2.1) with libc5.4.44. Image visualization was accomplished with KARMA, version 1.6.26 for Linux.

More guides for ST data reduction are available online at the DRAO web site: <http://www.drao.nrc.ca/facilities/telescopes/sst/cookbook>. I will try to be as detailed here as possible, to aid in any activities with DRAO ST images undertaken by future students of this field. DRAO package names are capitalized and bold (e.g. **CLEAN**) for clarity, but must be entered in the computer as lower case (e.g. clean). The DRAO ST simultaneously observes two wavelengths, and produces maps at both $\lambda = 21\text{cm}$ and $\lambda = 74\text{cm}$. Processing of both 21cm and 74 cm data is discussed here, with references to 74cm data made in brackets (e.g. 21cm (74cm)).

STEP ONE: POLAR CORRECTING THE IMAGES

Raw DRAO ST images have an uneven gain across them, due to the gaussian shape of the primary beam. To correct for this non-flat field, we run **POLARCORR**. Don't scale before correction. Name the output file MI21-POL (MI74-POL for 74cm), or something else descriptive. Use a cosine power of 6, and use the default FWHM of 107.2' (334.2 '). You may wish to set the output map to 0 (undefined data value) beyond a given radius (this eliminates noise which may affect **CLEAN** later on). I used 120' (240 '). Inspect the new image.

STEP TWO: CENTERING THE DATA YOU REALLY NEED

Beyond the central portion of unprocessed DRAO ST images is noise (e.g.

grating responses). Work with only the portion of data you really need. I chose the central 512^2 of my 1024^2 image. Use **MADR** to define a new image of 512^2 pixels (define file), and subset the original 1024^2 image (subs <file #> (cen 512)). Use "man" in **MADR** to copy the data into the new image (f<new file #>=f<old file #>). Don't forget to also define a smaller version of the dirty beam file (with the .P21 (.P74) extension), the same size as the data file.

STEP THREE: INITIAL CLEANING OF THE POLAR CORRECTED IMAGE

Sidelobe responses are prevalent around point sources within the image; they have an elliptical shape due to the elliptical synthesized beam shape of the DRAO ST. **CLEAN** can do away with these artifacts. Start **CLEAN** now. An action prompt is offered, but it can be ignored. The dirty map is the polar-corrected image, and the dirty beam is the file with the .P21 (.P74) extension (inspection shows a beam centred in the image, with sidelobe responses around it). Use this as the **CLEAN** beam. Call the output whatever you want; e.g. MI21-CL (MI74-CL). Output the clean components as 21(74)-COMPS. It may be a good idea to save the residual map to disk, in case you wish to restart **CLEAN**. Start with about 200 iterations (though as few as 60 may be sufficient). Inspect the cleaned image - note the sidelobe responses have been reduced, revealing asymmetrical rings around the point sources. These are due to phase errors in the telescope, and will be reduced by self-calibration of the image, the next step.

STEP FOUR: THE SELF-CALIBRATION PROCESS

Now that we have a **CLEAN** component model 21-COMPS (74-COMPS) we can proceed with the first iteration of a self-calibration routine. We will start with the phase information contained in the longer baselines only, and subsequent iterations will contain information from the shorter baselines. Start by running **PTSRCs** (make sure you have enough virtual memory, or you will get a segmentation fault). Use 21 (74) cm as the wavelength for analysis. Option 1 for **PTSRCs** will suffice. Now we will need to choose the minimum spacing for Antenna-based Calibration. As suggested by the recipe ("self_cal.ps", available online) choose for option 3 a minimum spacing of 36. As well, option 11 needs to be set. Here, we need the flux density of the strongest unresolved point source within the image (this will be S, in Jy). Use **FLUXFIT** to find this. For example, in the 74cm images, there is a strong point source located at ($21^h 18^m 53.43^s$, $49^\circ 36' 39.23''$). **FLUXFIT** removed this from my image and fitted a gaussian to it with an amplitude of $9724\text{mJy} \pm 40\text{mJy}$ with a goodness of fit $>>95\%$. Thus, $S=9.72\text{Jy} \pm 0.04\text{Jy}$, and (from the recipe) $n(\# \text{ of integration periods to be averaged}) = 36/S^2$ (for 408 MHz data). Since this is 0 in this case, I used a "reasonable" value of 10. The survey code is entered (J8 - I had to copy the file j8.tbl to J8.TBL) and the UV code is AA (the last 2 letters of the file J8RRN.V74**). Use the 74-COMPS file in **PTSRCs**. Do not use negative clean components in this. This will give you the file J8RRN.V74AB.

STEP FIVE: RUN PH2 ON THE RESULTS OF PTSRCs

Run **PH2** now. Use the file just created (**J8RRN.V74AB**) as the input file, and 74 cm as the wavelength. For 74 cm maps, only the RR polarization band is observed. UV code is now AB (or AC, etc). This gives a dirty map and dirty beam pair of images (each 1024^2), which then need to be cleaned.

STEP SIX: RUN **CLEAN** ON THE RESULTS OF **PH2**

To aid in a successful **CLEAN**, you may wish to make 512^2 copies (in **MADR**) of the dirty map/beam pair (which are 1024^2) output by **PH2**. **CLEAN** should then be straightforward.

STEP SEVEN: INSPECT RESULTS

This is critical in determining the quality of the final image. Compare the **CLEAN** result **MI74-CLII** to the original **MI74-CL**. Did the procedure reduce the asymmetrical rings around point sources? Did it add other unwanted artifacts? If it did, then you probably want to live with the original **CLEAN** job, and either retry a self-cal with different parameters, or skip it altogether. If all looks good, try another iteration (go back to **STEP 5** -> **PTSRCS** and use your recent **COMPS** file) using a minimum spacing of 24 (as suggested). For example, my 74 cm results show reduced rings, but an overall noisier background, and dark lines (parallel to the image's major grating response) appeared over an extended SNR within my image. Many self-cal's were tried with different parameters, but, for the 74 cm images each **CLEAN** image showed results similar to those described above. **SELF-CAL ROUTINES SHOULD NOT BE APPLIED IF THE RESULT SHOWS NEW ARTIFACTS**. In this spirit, the 74 cm images were simply cleaned, and used in the next process. The 21cm images, on the other hand, responded well to self-calibration. Three self-cal iterations produced a beautiful final image, with faint asymmetric rings around strong point sources. Artifacts appeared when more than three iterations were made, so the third iteration was deemed the best one. All four bands (A,B,C,D) for four polarizations (RR,LL,RL,LR) were used (i.e. 16 files **J8**A.V21AA,J8**B.V21AA,J8**C.V21AA,J8**D.V21AA**, where ****** is **RR,LL,RL, or LR**).

STEP EIGHT: ADDITION OF SHORT SPACINGS

Large scale structure is not included in the **DRAO ST** images. Since the antennas can only be spaced at a distance such that their dishes don't make physical contact, structure that a larger beam would be sensitive to is missed. It is therefore prudent to add in such structure, as seen by another telescope of lesser resolving power. Before we can proceed, one must obtain an appropriate telescope's data. Through one's **DRAO** account (drao.nrc.ca), one can access many past surveys at different wavelengths in a database. Look for your field (at the appropriate frequency) there. The reader is referred to L. Higgs' recipe for **HI-Line Map Reduction**, 1995, online at the **DRAO** web site.

SUB-STEP 8.1: Begin by calculating the factor by which you must multiply your image to convert its pixel values from mJy/beam to T_b (K). Given the

equation;

$$F = \frac{0.385E}{(1.13f^2R^2)}$$

where E=ratio of minor/major axis of synthesized beam, R is the minor axis of the beam (arcminutes) and f is the observation frequency in GHz. For 74cm images, we obtain;

$$F=0.144(\text{K/mJy/beam})$$

while for 21 cm images;

$$F=0.143 (\text{K/mJy/beam})$$

Next, we calculate the distance in the uv plane at which you want the low resolution and high resolution signal added with equal weight. Use the values for the survey you just obtained (i.e. the "other" telescope's beam width and working frequency)

For the 21cm image:

$$D = \frac{15.4\lambda(\text{cm})}{R(\prime)} = \frac{15.4 \times 21.1\text{cm}}{8.4\prime} = 38.68$$

Using $D_{low}/D_{high}=0.46667$ (same ratio as for the 26 m antenna at DRAO) we find

$$D_{high}=52.75$$

$$D_{low}=24.61$$

and, for 74cm:

$$D = \frac{15.4 \times 74\text{cm}}{0.85^\circ \times 60\prime}$$

$$D=22.345$$

$$\text{i.e. } D_{high}=30.47$$

$$D_{low}=14.22$$

SUB-STEP 8.2: Use **MAPCONVRT** to convert the low-resolution maps to a large area with a smaller, finer grid value. For the original 512^2 pixel (at $20''/\text{pixel}$) low resolution maps, I converted to 1024^2 at $10''/\text{pixel}$. One may try even greater increases.

SUB-STEP 8.3: Use **MAPTAPER** to smooth the edge of your maps, so that FT's don't produce Gibb's phenomenon at the edge. Not much is needed; only 10 pixels width to 50% taper value at edges of maps. Taper to the average value, parallel to edges.

SUB-STEP 8.4: Use **MAP2UVP** to build visibility map of the tapered map produced above.

SUB-STEP 8.5: **UVANALYZE** is used with option 4 to zero spatial frequencies at uv distances $> D$. Ellipticity (E) used was 1, position angle $A=0$, $D_{high}/D_{low}=2.41$. The inner and outer limits used are from 0.0 to D_{low} . Feathering is used with a ratio of D_{high}/D_{low} . All numbers used here are for the low resolution telescope, as calculated in SUB-STEP 8.1.

SUB-STEP 8.6: Do another polar correction to undo the low resolution telescope's natural shape. In **UVANALYZE**, use option 8 and, when asked for the distance to half-power beam width, specify D (from SUB-STEP 8.1). Use an E of whatever the minor/major axis of the "other" telescope's beam is, and use an angle = $A_{original} - 90^\circ$.

SUB-STEP 8.7: Use **MAP2UVP** to go back to normal space. Look at the resulting image to ensure no edge effects have contaminated the central portion.

SUB-STEP 8.8: Use **MAPCONVRT** once again to convert the resultant map back to its original pixel configuration (eg. from 1024^2 at $10''/\text{pixel}$ back to 512^2 at $20''/\text{pixel}$). It is important to get the grid increment correct here, or the result will be useless. This is the final low-resolution image for adding into your data. Inspect it.

SUB-STEP 8.9: Use **MAPTAPER** with the same pixel width as before to taper your high resolution maps (presumably, from the DRAO ST).

SUB-STEP 8.10: Transform your tapered high resolution map to the UV plane (**MAP2UVP**).

SUB-STEP 8.11: Use the resultant visibility set in **UVANALYZE**. Here we want to zero the short spacing UV visibilities for distances less than D. Use option 3, and inner, outer limits of 0.0 to D_{high} . Use feathering, but with the ratio of D_{low}/D_{high} (the inverse of the ratio used in SUB-STEP 8.5). The resulting visibilities are ready for the next step.

SUB-STEP 8.12: Use **MAP2UVP** to go back to real space. Look at the resulting map to make sure no suspicious artifacts have crept in. Depending on your choices in SUB-STEP 8.11, objects may now be surrounded by dark areas. This is normal, as these areas are to be filled in by large scale structure missing from the data before.

SUB-STEP 8.13: Go into **MADR**, and define a new file. Make sure it has exactly the same attributes as your original high resolution map, except, its units should be in T_b (not mJy/beam). In **MAN**, apply the following:

$$F\# = f1 \times F\# + f2 \times F\#$$

$F(\text{new number}) = (\text{factor to convert low resolution map to } K) \times f(\text{number of map from SUB-STEP 8.8}) + (\text{factor to convert high resolution map to } K) \times f(\text{number from SUB-STEP 8.12})$. The final map should be in units of brightness temperature.

STEP NINE: DERIVATION AND APPLICATION OF AGC CORRECTION FACTOR TO 74CM IMAGES

To have accurate T_b values in the 74cm map, one must multiply it by a correction factor known as the AGC factor (see text of thesis for explanation).

One must obtain maps of calibration objects 3C147 ($5^h42^m36.2^s$, $49^\circ51'7.2''$, J2000) and 3C295 ($14^h11^m20.65^s$, $52^\circ12'9.0''$, J2000) from another survey at 408 MHz. I used the Haslam ALLSKY survey. Go to your DRAO account and run **SURVEY**, choosing ALLSKY as the survey. Make small (64^2 pixels) maps centered on the above coordinates, at a grid increment of $1' 10''$. Use **CONV_MADR** and **CONVREALS** on them once you FTP them back to your machine. Now, make a 64^2 gaussian beam of 318' FWHM centered on pixel 33,33 using **GAUSSMAP**. Multiply the calibration object maps by this gaussian map in **MADR** using "man". Now, in **MADR**, find the average of each result by typing "in <f#> ext". For example, calibration object 1 (3C147) has <intcal1>=46.64 K, and 3C295 has <intcal2>=38.22K. Carry out these steps with a similar 64^2 map from the ALLSKY survey centered on the central coordinates of your observation field. Obtain <intobs> (e.g. for my J8 field, <intobs>=87.72K). Now, find the AGC correction factor from the following:

$$T'_A(obs) = \frac{\langle intobs \rangle}{\langle beam \rangle} = \frac{87.72}{0.97496} = 89.973K$$

$$T'_A(cal1) = \frac{\langle intcal1 \rangle}{\langle beam \rangle} = 47.84K, T'_A(cal2) = 39.2K$$

$$\text{Average } T'_A(cal) = 43.52K$$

Now apply:

$$T_A(obs) = 0.66 \times T'_A(obs) + 12$$

and

$$T_A(cal) = 0.66 \times T'_A(cal) + 12:$$

e.g. $T_A(obs) = 71.38K$, $T_A(cal) = 40.72K$. Finally, our AGC Correction factor is:

$$F_{AGC} = \frac{T_A(obs)+90K}{T_A(cal)+90K} = 1.235$$

Multiply your 74 cm DRAO maps by this factor in **MADR** ("man") and name the output "MI74-AGC" or something descriptive.

DRAO Synthesis Telescope maps are now properly reduced, calibrated, and ready for analysis.